NTNU – Trondheim
Norwegian University of
Science and Technology

Pressure Perpendicular to the Grain in Wooden Sills

Numerical Studies of Softening and Failure in Abaqus

Espen Ruud

Civil and Environmental Engineering
Submission date: June 2012
Supervisor: Kjell A Malo, KT

Norwegian University of Science and Technology
Department of Structural Engineering

NORGES TEKNISK-NATURVITENSKAPELIGE UNIVERSITET
INSTITUTT FOR KONSTRUKSJONSTEKNIKK

MASTEROPPGAVE 2012

Espen Ruud

TRYKKBELASTNING NORMALT FIBERRETNING PÅ TREVIRKE (COMPRESSION NORMAL GRAIN ON WOOD)

Bakgrunn:

På grunn av trematerialenes anisotrope karakter er det ikke like lett å bestemme kriterier for brudd i tre som det er for eksempel for isotrope metaller som stål. Strekk og trykkfasthet er forskjellig i de forskjellige retninger og interaksjonen mellom de forskjellige spenningskomponentene er mer komplisert. Trykk normalt fiberretning representer en duktil, men forholdsvis myk belastningsretning på trevirke. Nesten alle bygg har detaljer med denne type belastning og dette har tradisjonelt ikke vært noe stort problem.
Ved innføring av ny europeisk standard har imidlertid denne belastningsvarianten fått betydelig redusert beregningsmessig kapasitet og har medført at våre tradisjonelle detaljer ikke lenger oppfyller de beregningsmessige krav.

Hensikten med oppgaven er derfor vha eksperimentele og numeriske studier å klargjøre hvordan belastningene sprer seg i materialet og om mulig å forbedre numeriske modeller for å prediktere kapasiteten for trykk normaltt fiberretning.

Ved bruk av det kommersielt tilgjengelige programmet Abaqus skal det lages en modell av en tresvill med last vinkelrett på fiberretningen. Ved bruk av verktøy i programmet skal modellen bygges for å gi mest mulig realistisk respons for materialet gjennom både det lineære og ikkelineære responsområdet. Modellen skal også evaluere brudd og ideelt sett vise bruddets utvikling.
Modellen skal testes og sammenlignes med et tilsvarende fysisk eksperiment. Det skal videre kjøres en studie der parametere i modellen endres og tilsvarende fysiske eksperimenter gjennomføres, for å teste hvor robust modellen er.På bakgrunn av gjennomført studie skal viktigheten av testede parametere evalueres.

Etter samråd med veiledere kan kandidaten konsentrere sitt arbeide til spesielle deler av oppgaven, eller trekke inn andre aspekter.

Generelt:

Besvarelsen skal ha form som en forskningsrapport hvor det legges vekt på en klar og oversiktlig presentasjonsform. Besvarelsen skal leveres ved Institutt for konstruksjonsteknikk innen 11. juni 2012.
Faglærer: Kjell Arne Malo
Veiledere: Pål Ellingsbø og Nathalie Labonnote

NTNU, februar 2009

Kjell Arne Malo

Abstract

Joints with pressure perpendicular to the grain are a common occurrence in wooden structures. While the making of such a joint is very simple, dimensioning it is difficult: The load configuration causes a mix of ductile compressive failure and brittle tensile failure. In addition, the global response shows hardening after the first failure.

Recent changes to the design code has made the design bearing strength for this type of load so low that Norwegian houses no longer fulfill the requirements. As the houses remain standing even after the new rules were introduced, it is clear that a revision of the rules may be in order. The revision is made even more important by the growing interest for building large wooden structures.

This thesis focuses on using numerical models to estimate the bearing strength of wooden sills with pressure perpendicular to the grain and compares the numerical model with results from laboratory tests. The goal is to see how accurate response a numerical model can give for the problem in question, to and beyond first failure.

Many new and interesting tools for modeling of complex material behavior have been implemented in commercial FEA analysis software in later years. These tools are implemented in an attempt to mimic the complexity of the material behavior, but limitations in the software and hardware proved hard to overcome. While the model is able to give good estimates for bearing strength for certain cases, it proves unable to model the development after first failure.

Using results from laboratory tests in conjunction with the numerical model, the impact of tested parameters such as pith location, cross-section geometry and load placement is still evaluated. Results imply that all of these parameters severely impact the global response of the problem, particularly after first fracture.

The numerical model has potential, particularly as new modeling tools become available, and should be worked on.

Sammendrag

Skjøter der det er trykk vinkelrett på fiberretningen er svært vanlige i trebygg. Å lage et slikt ledd er meget enkelt, men dimensjoneringen byr på utfordringer: Denne lastkonfigurasjonen fører til både duktile trykkbrudd og sprø strekkbrudd rundt det belastede området. Videre vil den globale responsen få en fastning selv etter brudd.

Eurocoden ble nylig oppdatert med nye designregler for dette problemet, som setter bruddlasten så lavt at norske hus ikke lenger oppfyller kravene. Ettersom norske hus enda ikke har falt sammen, selv etter innføring av nytt regelverk, er det åpenbart at det trengs en revisjon av reglene. En slik oppdatering blir enda viktigere ved øket interesse for å bygge store konstruksjoner i tre.

Denne diplomoppgaven fokuserer på bruk av numeriske modeller for å estimere bærestyrken til tresviller med trykk vinkelrett på fiberretningen. Videre blir disse modellene sammenlignet med resultater funnet ved forsøk i laboratorium. Målet er å se hvor nøyaktig respons en numerisk modell kan gi for det aktuelle problemet, både til og forbi brudd.

Utviklingen av programvare for numeriske analyser har i de senere årene tilgjengeliggjort stadig flere verktøy for å modellere kompleks materialoppførsel. Slike verktøy blir implementert i et forsøk på å gjenskape den komplekse materialoppførselen i det aktuelle problemet, men begrensninger i både programvare og maskinvare viser seg å skape mange problemer. Den endelige modellen er i stand til å gi gode estimater for bærestyrke i enkelte oppsett, men er ikke i stand til å modellere utviklingen etter brudd.

Ved bruk av resultater fra laboratorietestene sammen med den numeriske modellen, er det likevel mulig å evaluere innvirkningen fra de testede parameterne: Plassering av marg, tverrsnittsgeometri og lastplassering. Det viser seg at alle disse parameterne har en betydelig innvirkning på den globale responsen til systemet, særlig etter brudd.

Den numeriske modellen har potensiale, særlig etter hvert som nye modelleringsverktøy blir tilgjengelige, og bør arbeides videre med.

Preface

This master thesis was written as the final assignment at the five year masters program Civil and Environmental engineering at the Norwegian University of Science and Technology (NTNU). Through the five year program, I have focused on structural engineering. During the first semester of my fifth year, I completed a project based course focusing on the material properties of wood. This work was extended into this master thesis, which accounts for all the credits in the final semester of the masters program.

The thesis was suggested by the student and was refined in cooperation with Kjell Arne Malo. With basis in simple numerical simulations run as a part of the project work the semester before, the goal was modeling the response of wood with pressure perpendicular to the grain all the way to failure and beyond.

Writing this thesis has been incredibly challenging and exciting. Working with theory at the forefront of current knowledge has been gratifying when things were working and frustrating when they do not. The process has given me a lot of insight into subjects of which I had no prior knowledge, like fracture mechanics, adaptive meshing techniques and the extended finite element method. It has also improved my understanding of wood as a material and given me immense respect for its complexity: Despite being such an old construction material, there are still a multitude of unsolved engineering challenges related to it.

I would like to thank my supervisor Kjell Arne Malo for his guidance through the writing of this thesis, providing valuable input, perspective and keeping me in line when I try to make things too complicated for my own good. Thanks are due Pål Ellingsbø for helping out with the many software problems that arose during the numerical modeling and for providing access to a decent computer for running analysis so my laptop survived the semester. I would also like to thank the Terje Petersen at the laboratory at the department of structural engineering for being efficient and helpful in the making of the test samples.

Finally, I would like to thank my fellow students for useful input and discussion, as well as being good company through the many long days. I don't think I would have been able to keep motivation up without your diversions.

Trondheim, June 2012

Espen Ruud

-Never did I imagine myself sitting in a acclimatized room with a piece of wood in each hand, pondering their differences.

Contents

Abstract **iii**

Sammendrag **v**

Preface **vii**

Terminology **xiii**
Normative references xiii
Common abverations xiii

Nomenclature **xiv**

1 Introduction **1**
1.1 Background 1
1.2 Problem Definition 1
1.3 Method 3
1.3.1 Numerical Modeling 3
1.3.2 Calibration and Control 3
1.3.3 Using the Model 3

2 Theory **5**
2.1 The Structure of Wood 5
2.1.1 Cell Arrangement 5
2.1.2 Growth Rings 5
2.2 Mechanical Properties of Wood 7
2.2.1 Linear Elastic Response 7
2.2.2 Nonlinear Response 8
2.3 Abaqus Spesific Theory 15
2.3.1 Elastic Behaviour in Abaqus 15
2.3.2 XFEM in Abaqus 16
2.3.3 Hill Anisotropic Yielding 20
2.3.4 Adaptive Meshing 20
2.4 Other Options for Material Behavior 21

3 Modeling **23**
3.1 Geometry 23
3.2 Material Model 24
3.2.1 Parts 1 and 2 26
3.2.2 Parts 3, 4 and 5 28

3.2.3 Parts A and B . . . 28
3.3 Interactions . . . 28
3.3.1 Bottom Interaction . . . 29
3.3.2 Top Interaction . . . 30
3.4 Meshing . . . 31
3.5 XFEM . . . 34
3.5.1 Customizing Steps and Solution Controls . . . 34

4 Laboratory tests **37**
4.1 Material . . . 37
4.1.1 Moisture . . . 37
4.1.2 Density . . . 38
4.1.3 Pith Location . . . 38
4.1.4 Sources of Error . . . 38
4.2 Execution of Tests . . . 39
4.2.1 Setup . . . 39
4.2.2 Boundry Conditions and Gathering of Data . . . 39
4.2.3 Sources of Error . . . 41
4.3 Test Results . . . 41
4.3.1 Load-Displacement Diagrams . . . 42
4.3.2 Moisture Content . . . 52
4.3.3 Densities . . . 52

5 Calibration **55**
5.1 Testing Material Model in Parts 1 and 2 . . . 55
5.1.1 XFEM . . . 55
5.1.2 Hill Anisotropic Yield . . . 57
5.1.3 XFEM and Hill Anisotropic Yield . . . 57
5.1.4 XFEM Deactivated (Semi XFEM) . . . 58
5.2 Calibrating the Reference Case . . . 58
5.2.1 Initial Changes . . . 58
5.2.2 Increasing Displacement . . . 59
5.2.3 Comparing Initial Model with Laboratory Tests . . . 59
5.2.4 Calibration . . . 60

6 Discussion **65**
6.1 Evaluation of Load-displacement Response Data From the Model . . . 65
6.1.1 N-Pc-Lc . . . 65
6.1.2 N-Pe-Lc . . . 66
6.1.3 N-Pb-Lc . . . 66
6.1.4 N-Pa-Lc . . . 66
6.1.5 N-Pb-Lh . . . 66
6.1.6 N-Pb-Le . . . 66
6.1.7 D-Pb-Lc . . . 67
6.1.8 H-Pb-Lc . . . 67
6.2 Model Robustness Evaluation . . . 67
6.2.1 Pre-Fracture Behavior and Strength . . . 67
6.2.2 Post Fracture Behavior . . . 71
6.2.3 Utility . . . 72

6.3 Significance of Parameters . . . 73
6.3.1 Pith Location . . . 73
6.3.2 Load Placement . . . 74
6.3.3 Sill Geometry . . . 75

7 Conclusion **77**

8 Further Work **79**

A Laboratorium Test Plan **83**
A.1 General Setup for Testing . . . 83
A.1.1 Tools . . . 83
A.1.2 Execution . . . 83
A.2 Pith Location Test 1 (N-Pc-Lc) . . . 83
A.3 Pith Location Test 2 (N-Pe-Lc) . . . 86
A.4 Pith Location Test 3 (N-Pb-Lc) . . . 88
A.5 Pith Location Test 4 (N-Pa-Lc) . . . 90
A.6 Load Location Test 1 (N-Pc-Lh) . . . 92
A.7 Load Location Test 2 (N-Pc-Le) . . . 94
A.8 Load Location Test 1 with Alternate Pith Location (N-Pb-Lh) . . . 96
A.9 Load Location Test 2 with Alternate Pith Location (N-Pb-Le) . . . 98
A.10 Geometry Test 1 (D-Pb-Lc) . . . 100
A.11 Geometry Test 2 (H-Pb-Lc) . . . 102

B Eurocode Calculations **105**
B.1 General Calculations . . . 105
B.2 Cases 1, 2, 3, 4, 5, 7, 9 and 10 . . . 105
B.3 Cases 6 and 8 . . . 106

C Plots of Numerical Results **107**
C.1 Numerical Load-Displacement Comparison to Laboratory Results . . . 107

D Specimen Measurements (Digital) **113**

E Test Data (Digital) **115**

F Abaqus Input Files (Digital) **117**

Terminology

Normative References

Abaqus FEA Finite element analysis software, originaly written by Dassault Systemès. Formerly known as ABAQUS.

Eurocode 5 NS-EN 1995-1-1 Eurocode 5: Design of timber structures. Part 1-1: General Common rules and rules for buildings. Abverated EC5.

NS-EN 338 NS-EN 338: Structural timber Strenght classes

Abbreviations

ALE Arbitrary Lagrangian-Eulerian analysis, an adaptive meshing technique

DOF Degree of freedom

EC5 See "Eurocode 5" under normative references

ELR End of linear range

FEA Finite element analysis, method for numerical solution of field problems

FEM Finite element method, see FEA

LEFM Linear elastic fracture mechanics

MAXE Maximum nominal strain criterion for damage initiation

MAXS Maximum nominal stress criterion for damage initiation

RF Reaction force

SLS Serviceability limit state

ULS Ultimate limit state

XFEM Extended finite element method, an extension of FEM for solving problems with discontinuities

Symbols used

General Symbols

ϵ_{ij}	Component in the strain tensor
γ	Shear strain
ν_{ij}	Poisson's ratio between direction i and j
σ_{ij}	Component in the stress tensor
σ_{ij}^{y}	is the yield stress when σ_{ij} is applied as the only nonzero stress component
τ	Shear stress
C_{ij}	Component in the stiffness matrix
E_i	Elasticity modulus in direction i
G_{ij}	Shear modulus for the ij plane
P_i	Load in direction i
S_{ij}	Component in the compliance matrix
u_i	Displacement in direction i

LEFM Symbols

Γ	Energy used to open new crack surface
γ	Free surface energy per unit area
σ_c	Critical stress level
a	Crack length
a_c	Critical crack length
E	Youngs modulus
G	Griffith energy or crack-extension force
K	Stress intensity factor
U_E	Stored elastic energy
U_P	Energy used in plastic deformation

W work done by applied loads

Y Geometry factor

Abaqus Symbols

δ_n is the separation corresponding to t_n

δ_s is the separation corresponding to t_s

δ_t is the separation corresponding to t_t

ϵ_n Strain component normal to the likely cracked surface

ϵ_n^0 Maximum allowed strain component normal to the likely cracked surface

ϵ_s First shear strain component on the likely cracked surface

ϵ_s^0 Maximum allowed first shear strain component on the likely cracked surface

ϵ_t Second shear strain component on the likely cracked surface

ϵ_t^0 Maximum allowed second shear strain component on the likely cracked surface

η Viscosity coefficient representing the relaxation time of the viscous system

d Damage variable evaluated in the original inviscid model

G_n Work done by the traction and its conjugate separation in the normal direction

G_n^C Critical fracture engery requred to cause failure in the normal direction

G_s Work done by the traction and its conjugate separation in the first shear direction

G_s Work done by the traction and its conjugate separation in the second shear direction

G_s^C Critical fracture engery requred to cause failure in the first second direction

G_t^C Critical fracture engery requred to cause failure in the first shear direction

t_n Stress component normal to the likely cracked surface

t_n^0 Maximum allowed stress component normal to the likely cracked surface

t_s First shear stress component on the likely cracked surface

t_s^0 Maximum allowed first shear stress component on the likely cracked surface

t_t Second shear stress component on the likely cracked surface

t_t^0 Maximum allowed second shear stress component on the likely cracked surface

$H(x)$ Heaviside function

$N(x)$ Shape function

Eurocode Symbols

ρ_{mean} Mean density

$\sigma_{c,90,d}$ Design compressive stress on the effective contact surface perpendicular to the grain

A_{ef} Effective contact surface for compression perpendiular to the grain

$E_{0,mean}$ Mean elasticity modulus parallel to the grain

$E_{90,mean}$ Mean elasticity modulus normal to the grain

$F_{c,90,d}$ Design compressive load perpendicular to the grain

$f_{c,90,d}$ Design compressive strength

G_{mean} Mean shear modulus

$k_{c,90}$ Factor accounting for load configuration, spliting of the wood and the magnitude of the compressive deformation

Wood Specific Symbols

ρ_w Density of the undried specimen

K Coefficient for volume shinkage

v_w Volume of an undried specimen

Chapter 1

Introduction

1.1 Background

Wood is one of the oldest construction materials known to man. Norway has always had a rich supply of timber, and as such wood is important in Norwegian building tradition. Even though innovation has brought competition from new engineered materials, wood is still in wide use. Engineered wooden constructions, like bridges, have sparked new interest for the material. Recently there have been several propositions for high-rise buildings with wooden support systems. This has resulted in an increased focus on the challenges of compression perpendicular to the grain of wooden sills and beams.

The latest version of Eurocode 5 contains rules for design of contact joints with compression perpendicular to the grain dependent on several geometrical parameters and loading situations. However, these rules have been shown to overestimate the compressive strength perpendicular to the grain [3].

Using numerical models to calculate stiffness as well as ultimate load can be of great help when creating and evaluating criteria for design rules, like those found in the Eurocodes. Through the use of a numerical model, it is possible to make quick and inexpensive parameter studies to evaluate the impact of several variables.

Software developments in later years have made several new tools widely available through commercially available analysis programs. Some among these, like the extended finite element method (XFEM), are of particular interest for modeling problems where post-fracture behavior is important. Introduced by Belytschko og Black [26] in 1999, it is now integrated in FEM software like Abaqus. Other tools, like adaptive meshing, enables the analyst to get results even when the original mesh is severely distorted. This paper will investigate the possibilities and limitations of modeling failure in wood with pressure perpendicular to the grain using such new tools.

1.2 Problem Definition

Pressure perpendicular to the grain of wood is a geometrically simple problem made complicated by the properties of wood. The orthotropic nature of the material, where stiffness and strength in the grain direction is often 10-15 times that of other directions [16], give rise to the hammock effect shown in figure 1.2. This "hammock" distributes the downward force to material surrounding the material directly under the load, making the system stronger.

Figure 1.1: A proposition for world's tallest wooden residential building in Bergen. Foto: [4]

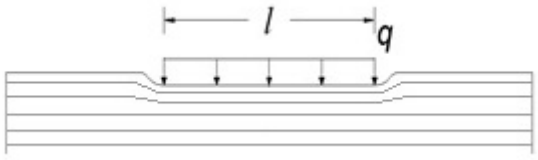

Figure 1.2: Hammock effect in a specimen of wood

Two of the four failure mechanisms described by Mackenzie-Helnvein, Eberhardsteiner and Mang [18] are active when there is pressure perpendicular to the grain. First, local ductile compression failure occurs under the load, causing the fibers to take a greater part of the load due to the hammock effect before the second failure, brittle tensile failure in fiber direction, occurs. Thus, since fibers lose little strength when being crushed perpendicular to their grain [18], the hammock effect can give strength to the system well beyond what is indicated by 1-axis strength tests. Works by Ribberholt [19] show that the system may be strengthened by end lengths up to one and a half time the specimen height in the case of a sill.

Figure 1.3 shows four load cases where pressure perpendicular to the grain is significant to the design. Case 1 does not allow for any hammock effect as end lengths are zero. Case 2 to 4 can all have a load increase after local ductile compression failure because of the hammock effect. If there is perfect symmetry about the horizontal center plane of the beam in case 2, it is equivalent to a version of case 3 with half height and zero friction between the sill and the surface on which it is placed. Case 4 is a modification of case 2 where bending and shear will complicate the stress and strain fields. In this thesis, the focus is to model compressive failure, post failure hardening due to the hammock effect and eventually brittle fiber fracture. For this purpose case 3 is suitable for representing both case 2 and 3. While interesting, case 4 introduces complications by having a displacement that is a superposition of beam bending, beam shear and compressive crushing. This makes calibration and verification of the numerical model using laboratory tests difficult and the case is therefore omitted.

The Eurocode rules for this problem are very rudimentary, accounting only for the strenght perpendicular to the grain, to some degree the geometry of the sill cross section

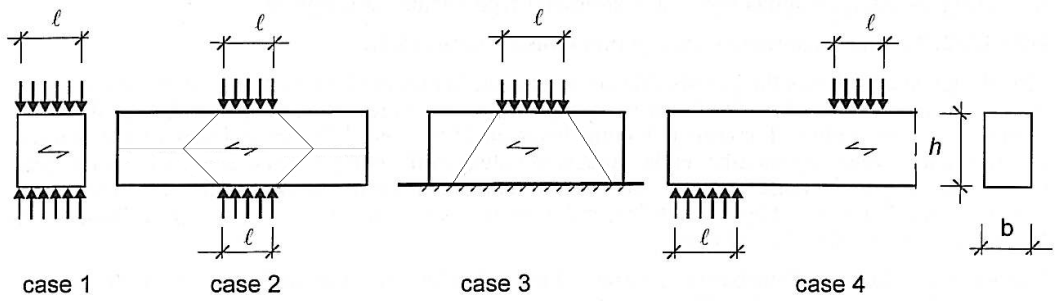

Figure 1.3: Loading situations with compression perpendicular to the grain [11]

and to some degree the load situation. Oversimplification may be the cause of the ruleset giving to high strengths according to Leijten and Shoenmakers [3], while Norwegian engineers say that no Norwegian wooden residential home would be standing if the Eurocode was right.

1.3 Method

1.3.1 Numerical Modeling

A numerical model of a reference case will be created using a commercially available finite element analysis program called Abaqus FEA. The model will be of case 3 in figure 1.3 and should produce realistic load-displacement diagrams with clear points of failure. To achieve this, it must feature elastic orthotropic properties as well as weakening, failure or both, beginning at a set stress or strain situation. A secondary but important goal is to get the model to be able to realistically model behavior after the first fiber failure.

1.3.2 Calibration and Control

To make sure the right parameters and properties are used in the model, laboratory tests will be run of the reference case. The model will then be calibrated to match an avarage of the results from the laboratory tests.

After the model has been calibrated to match the reference case, its robustness must be controlled. This will be done by varying pith location, load placement and geometry from that of the reference case. Only one parameter is varied at a time and each parameter is varied at least twice to collect a total of three data sets for each parameter, the reference case being one of the data sets in all cases. The same tests will be run both in the laboratory and with the numerical model, before being compared. If the results do not correspond, further calibration may be attempted given that such a calibration can be done without affecting cases where the results do correspond. Should there be parameters that the model cannot account for through calibration, other options for accounting for these should be considered.

1.3.3 Using the Model

If the model is either calibrated to produce realistic results for variations of all parameters on its own or in combination with other rules, it may be used in a further parameter study. After gathering sufficient data it could be used to generate a criterion for failure in the

case modeled, accounting for all parameters that were shown to impact the result. Bearing strengths calculated using this criterion may then be compared to bearing strengths calculated using the same parameters with Eurocode 5.

Chapter 2

Theory

This paper assumes basic understanding of physics, structural engineering, wood anatomy and finite element analysis. The reader is referred to literature covering these subjects should the need arise. Some supplementary literature is: "Mechanics of Wood and Wood Composites" by Jozsef Bodig and Benjamin A. Jayne [16] for understanding the mechanics of wooden materials, "Trekonstruksjoner" by Petter Aune [5] for understanding design of wooden structures and "Concepts and Applications of Finite Element Analasys" by Robert D. Cook with others [20] for understanding the finite element method.

2.1 The Structure of Wood

Wood is a complex material with several layers of composite structure: The cell walls, the cell arrangement and the growth rings function as composites. All of these must be considered to understand the relation between structure and properties [16]. For the purpose of modeling wood as a construction material, the focus is on the macrostructure: Cell arrangement and the growth rings.

2.1.1 Cell Arrangement

The arrangement of the cells in wood gives it some of its characteristic properties. Figure 2.1 shows the cellular structure of a typical softwood. Note that a majority of the volume is occupied by fiber cells, called tracheids, with their longitudinal axis parallel to the central axis of the tree. The fibers are held together by an adhesive called lignin, effectively functioning as a composite with unidirectional fibers. [16].

2.1.2 Growth Rings

Wood grown in a temperate climate nearly always produces one growth ring each year, forming the characteristic concentric annual rings shown in figure 2.1(4). The rings are the composed of a layer of earlywood that develops rapidly early in the season and a layer of latewood that develops slowly at the end of the season [10]. Figure 2.1 shows that there is a significant difference in the cross sectional dimensions of the tracheids in earlywood as contrasted to the latewood, making the latewood layers stronger than the earlywood layers.

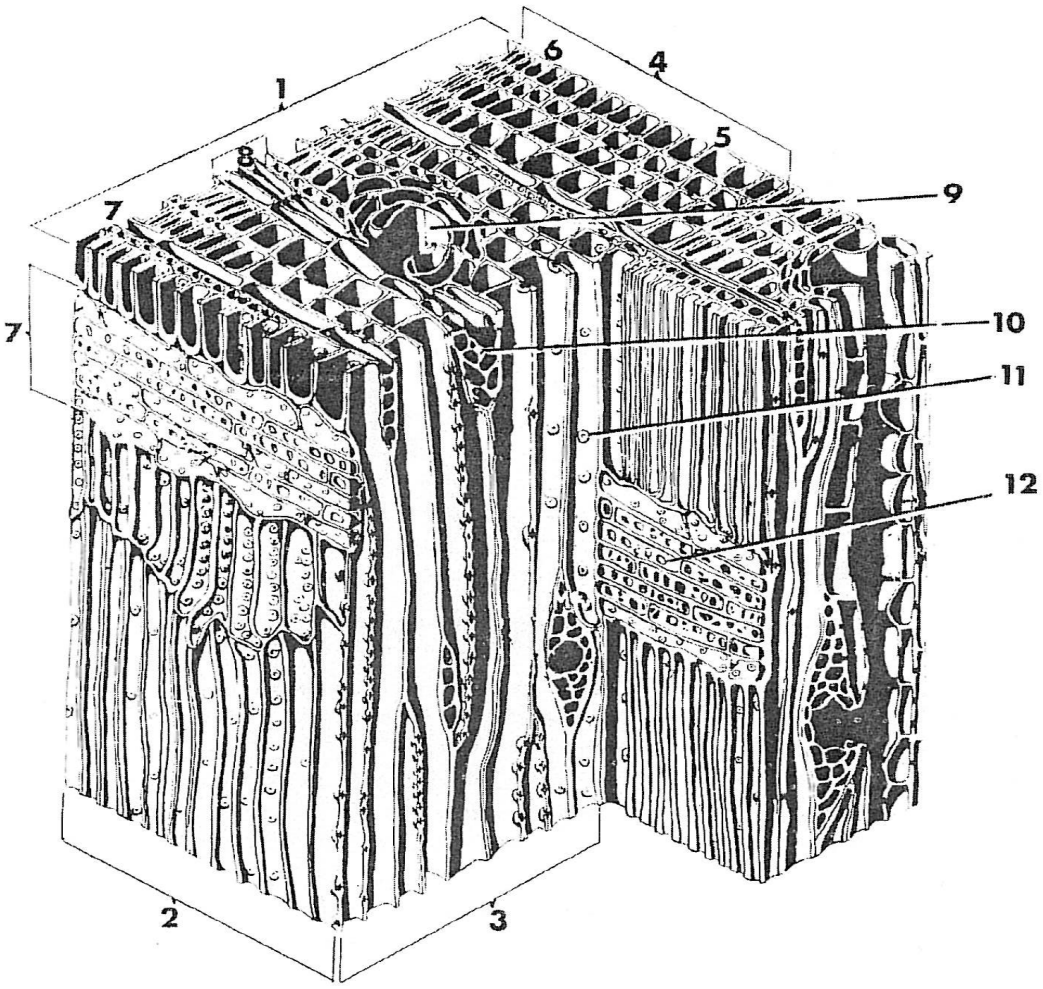

Figure 2.1: Celluar structure of a softwood: (1) cross section, (2) radial section, (3) tangential section, (4) growth ring, (5) earlywood, (6) latewood, (7) wood ray, (8) fusiform ray, (9) vertical resin duct, (10) horisontal resin duct, (11) bordered pit, (12) simple pit. From: Foulger [8]

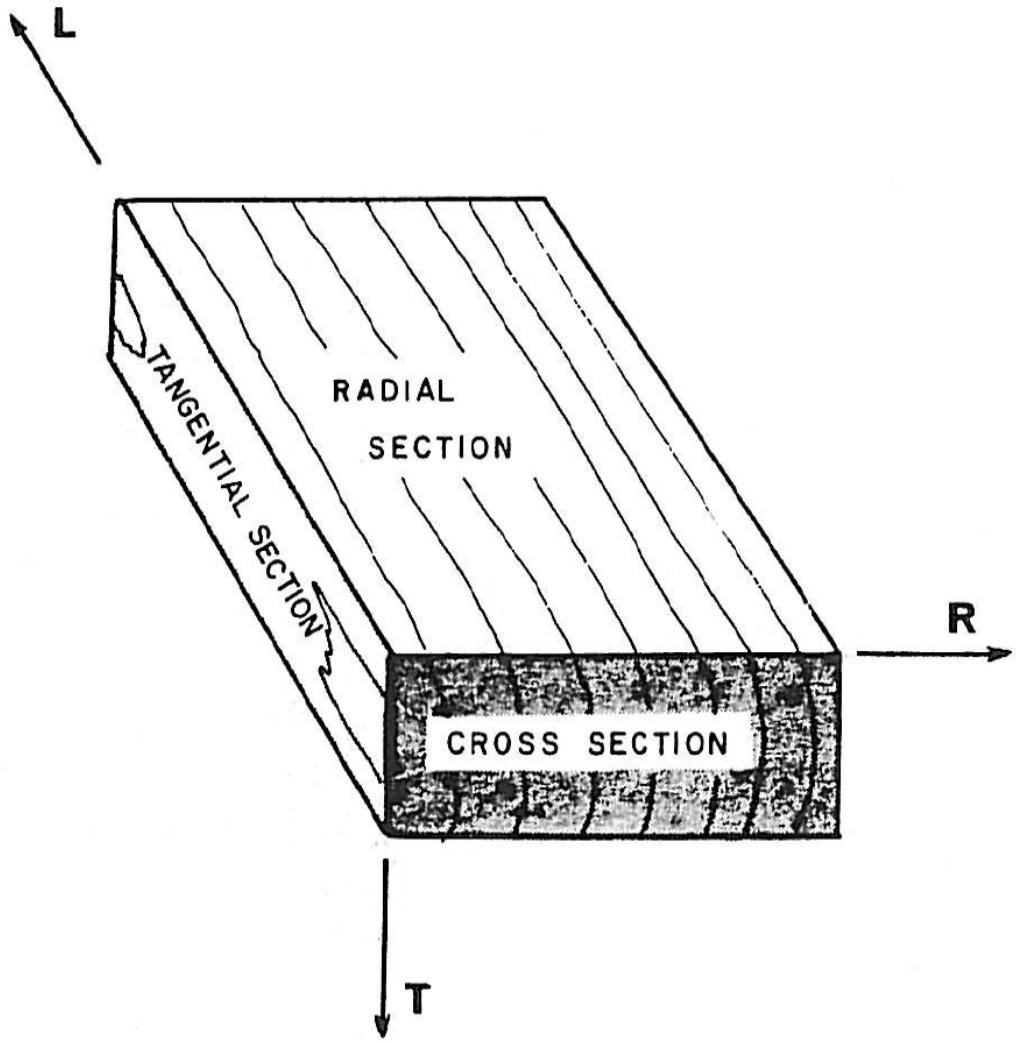

Figure 2.2: Defenition of sections and directions for a rectangular block of wood [16]

2.2 Mechanical Properties of Wood

2.2.1 Linear Elastic Response

Due to the arrangement of the wooden cells and the growth rings, wood has different elastic properties in different directions. It is an anisotropic material, which is defined a material where properties at a point may vary with direction or orientation of reference axes. Should the properties of the material in any direction be the same as the properties along a symmetric direction with respect to a plane, then that plane is defined at a plane of material symmetry. A material may have any number of these planes, where the two extremes are identified as general anisotropic for zero planes of material symmetry and isotropic for an infinite number of planes of material symmetry [15].

Wood has an organization that causes symmetry of properties about three planes. Materials that have symmetry about at least three planes are commonly referred to as orthotropic materials. These planes can be defined as the normal planes to three directions identified in a cylindrical coordinate system as the radial-, tangential- and longitudinal direction as shown in figure 2.2. The figure shows that for wood, the radial direction

corresponds to behavior perpendicular to the grain and growth rings, the tangential direction corresponds to behavior perpendicular to the grain and tangential to the growth rings while the longitudinal direction corresponds to behavior parallel to the grain.

Linking stresses and strains is done with Hookes law. In its general form it requires the use of 81 individual material constants. This is both impractical and obtaining all the constants is near impossible. The amount of constants may be reduced to 36 by observing symmety in the stress and strain tensors [15]:

$$\begin{aligned} \sigma_{ij} &= \sigma_{ji} \\ \epsilon_{ij} &= \epsilon_{ji} \end{aligned} \tag{2.1}$$

Using energy balance it may then be proven that [15]:

$$\begin{aligned} C_{ij} &= C_{ji} \\ S_{ij} &= S_{ji} \end{aligned} \tag{2.2}$$

where C_{ij} is a component in the stiffness matrix while S_{ij} is a component in the compliance matrix [15].

In the case of orthotropic materials, it is possible to simplify Hookes law so that only nine individual material constants are required [16]. The resulting simplified version of Hookes law, with stiffness components, is shown in matrix form in equation 2.3 [15]:

$$\begin{bmatrix} \sigma_1 \\ \sigma_2 \\ \sigma_3 \\ \tau_4 \\ \tau_5 \\ \tau_6 \end{bmatrix} = \begin{bmatrix} C_{11} & C_{12} & C_{13} & 0 & 0 & 0 \\ C_{21} & C_{22} & C_{23} & 0 & 0 & 0 \\ C_{31} & C_{32} & C_{33} & 0 & 0 & 0 \\ 0 & 0 & 0 & C_{44} & 0 & 0 \\ 0 & 0 & 0 & 0 & C_{55} & 0 \\ 0 & 0 & 0 & 0 & 0 & C_{66} \end{bmatrix} \begin{bmatrix} \epsilon_1 \\ \epsilon_2 \\ \epsilon_3 \\ \gamma_4 \\ \gamma_5 \\ \gamma_6 \end{bmatrix} \tag{2.3}$$

2.2.2 Nonlinear Response

Experiments done by Dahl [6] showed that wood can be a brittle material with little plastic deformation before failure, especially parallel to the grain. For compressive forces perpendicular to the grain however, wood has a ductile response similar to metal placticity. This means that the nonlinear behavior of wood depends heavily on loading. Mackenzie-Helnwein [18] identifies four types of failure, of which two are active in this problem:

The brittle tensile failure in the grain direction is dominated by damage and failure mechanisms. An accurate material model for this mechanism should include a failure criterion, a softening rule and ideally allow crack growth. This might be achieved through the use of a damage initiation criterion, a damage evolution rule and XFEM.

For the volumes where the ductile compressive behavior is dominating, the response can be modeled either by using a yielding criterion or damage evolution.

The following subsections will briefly show the theory needed to model in this manner. Other options for the nonlinear response are discussed briefly in section 2.4.

Linear-Elastic Fracture Mechanics

Linear elastic fracture mechanics (LEFM) is a method of describing crack growth in a material. A crack is assumed to exist in a linearly elastic material, with a crack tip of infinite stiffness. This assumption; an infinitely stiff crack tip in an elastic material, causes

a stress singularity around the crack tip with stress approaching infinite while the strains approach zero. The singularity makes stress and strain conditions unsuitable for deciding if the crack will grow. To deal with this issue, the method of LEFM originally developed by Griffith is based around thermodynamics [9].

Griffith Energy Balance Using an expression for change in free energy with respect to crack length, Griffith energy balance evaluates the area directly in front of the crack tip. This area is the new crack surface that will appear during the next incremental growth of the crack. During crack growth, stresses around the crack are relaxed and some elastic energy is released. Conversely, total surface energy is increased due to the increased surface area of the crack. Griffith defines the energy balance in a material with a crack as follows:

$$-\frac{\partial \Pi}{\partial A} = \frac{\partial U_P}{\partial A} + \frac{\partial \Gamma}{\partial A} \tag{2.4}$$

where

$$\Pi = U_E - W \tag{2.5}$$

and

U_E is the stored elastic energy

W is the work done by applied loads

U_P is the energy used in plastic deformation

Γ is the energy used to open new crack surface

The equation simply states that sufficient potential energy must be available in the system to overcome the surface energy required of a new crack surface in the material for a crack to grow. Since the material is assumed to be ideally brittle, the energy dissipated due to plastic deformation is considered negligible. It is also assumed that the crack grows slowly, so that the kinematic contribution to the energy balance is neglected [28].

In a body of elastic material containing a crack, the crack-extension force is defined as

$$G = -\frac{\partial \Pi}{\partial A} \tag{2.6}$$

per unit width of crack front. It is important to note the distinction between crack area and surface area. A crack has two matching surfaces, so the crack surface area is twice the projected crack area [28].

Using the total energy of the system and Clapeyron's theorem of linear elastostatics, this can be rewritten as

$$G = \frac{\partial U_E}{\partial A} \tag{2.7}$$

Using the stress solutions found by Inglis, Griffith defined the increase in strain energy due to the elliptic cavity with zero radius in an infinite plane. This may be used to express the total energy of the system in the case of a thin plate as [28]

$$U_{total} = -\frac{\pi a^2 \sigma^2 B}{E} + 4aB\gamma \tag{2.8}$$

where

B is the plate thickness
σ are stresses in unaffected parts of the plate
a is the crack length
E is the Youngs modulus
γ is the free surface energy per unit area

Using derivation with respect to A, which is equivalent to 2aB, an expression for change in total energy over time is attained as only the crack area is time dependent. It is obvious that the total energy has a local maximum when the change in total energy over time is zero. This maximum occurs at the following crack length [28]

$$a_c = \frac{2\gamma E}{\pi\sigma^2} \tag{2.9}$$

This can be rearranged to yield the critical stress level that a cracked body can sustain for constant load under plane stress conditions:

$$\sigma_c = \sqrt{\frac{2E\gamma}{\pi a}} \tag{2.10}$$

Energy Release Rate The energy release rate is commonly denoted G and it is the strain energy that is used to create new surface, causing an increased total surface energy in the solid, when the crack grows an increment. Each increment has a length denoted a and the length of the increment is dependent on the properties of the material through which the crack is propagating.

In the load-displacement diagram shown in figure 2.3, the potential energy of the specimen is the area above the load-displacement curve, the area below the curve is the recoverable strain energy stored in the specimen and the area of the rectangle is the work done by external force. The potential energy change is the difference between work done by external forces and the recoverable strain energy stored in the specimen. More energy is stored in a specimen with a crack of length $a + \delta a$ than in a specimen with a crack of length a. For a system with constant load conditions, the increase is given by

$$\delta U_E = \frac{1}{2}(u_1 - u_2)P_1 = \frac{1}{2}P_1\delta u \tag{2.11}$$

This increase is due to work done by the load, which has moved a distance of $u_2 - u_1$. The work done by external applied load is

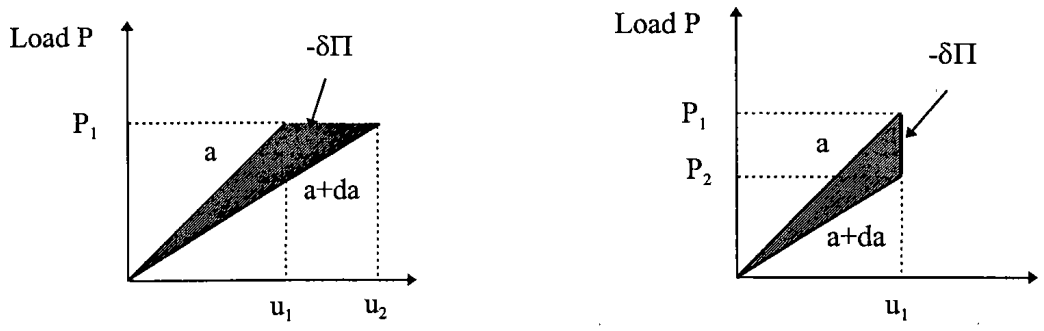

Figure 2.3: Load displacement characteristics for cracked bodies: (a) constant load crack extension, (b) crack extension under constant displacement [28].

$$\delta W = P_1(u_2 - u_1) \tag{2.12}$$

It is clear that the recoverable elastic energy stored in the system is less than the work done by applied loads. The missing energy is the hatched coloured area in figure 2.3(a) and is equal to the energy spent in increasing crack surfaces. For a system with constant displacement conditons, the increase in crack length causes a decrease in stored elastic strain energy given by

$$\delta U_E = \frac{1}{2}(P_1 - P_2)u_2 = \frac{1}{2}u_1\delta P \tag{2.13}$$

which is the hatched area in figure 2.3(b). In a constant displacement system, no external work is done, so all the above energy is used in increasing crack surfaces.

In summary, the constant load condition requires the potential energy release shown in equation 2.11 while the constant displacement condition requires the potential energy release shown in equation 2.13 [28].

Stress Intensity Factor The stress intensity factor defines the amplitude of the singularity around the crack tip and thus the intensity of the local stress field, effectively describing the rise in local stresses around the crack tip. Local stresses near the crack tip are proportional to K, which has one value for each of the three failure modes shown in figure 2.4.

Resulting stress fields are described using a polar coordinate system with r being the distance to the crack top and θ being the angle to the plane in which the crack is propagating as shown in figure 2.5. The stress fields around a crack tip in an isotropic plate of linearly elastic material are shown in table 2.1.

In general the stress intensity factor is dependent on the applied stress, crack size and the geometry of the specimen. It is given as

$$K = Y\sigma\sqrt{\pi a} \tag{2.14}$$

where Y is a geometry factor that accounts for the geometry of a crack system in relation to the applied load. For the case in figure 2.5, a centre crack in an infinite plate, $Y = 1.0$. While accurate analytical values for the geometry factor exist for simplified problems, finding the geometry factor for any realistic geometry requires the use of numerical methods such as FEM [28].

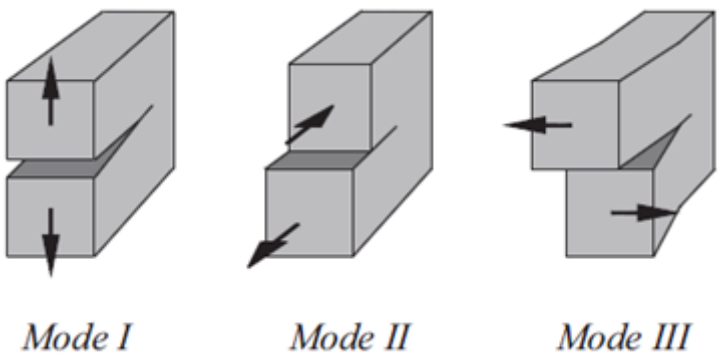

Figure 2.4: Modes of crack extension: (I) opening mode, (II) sliding mode, (III) tearing mode [7]

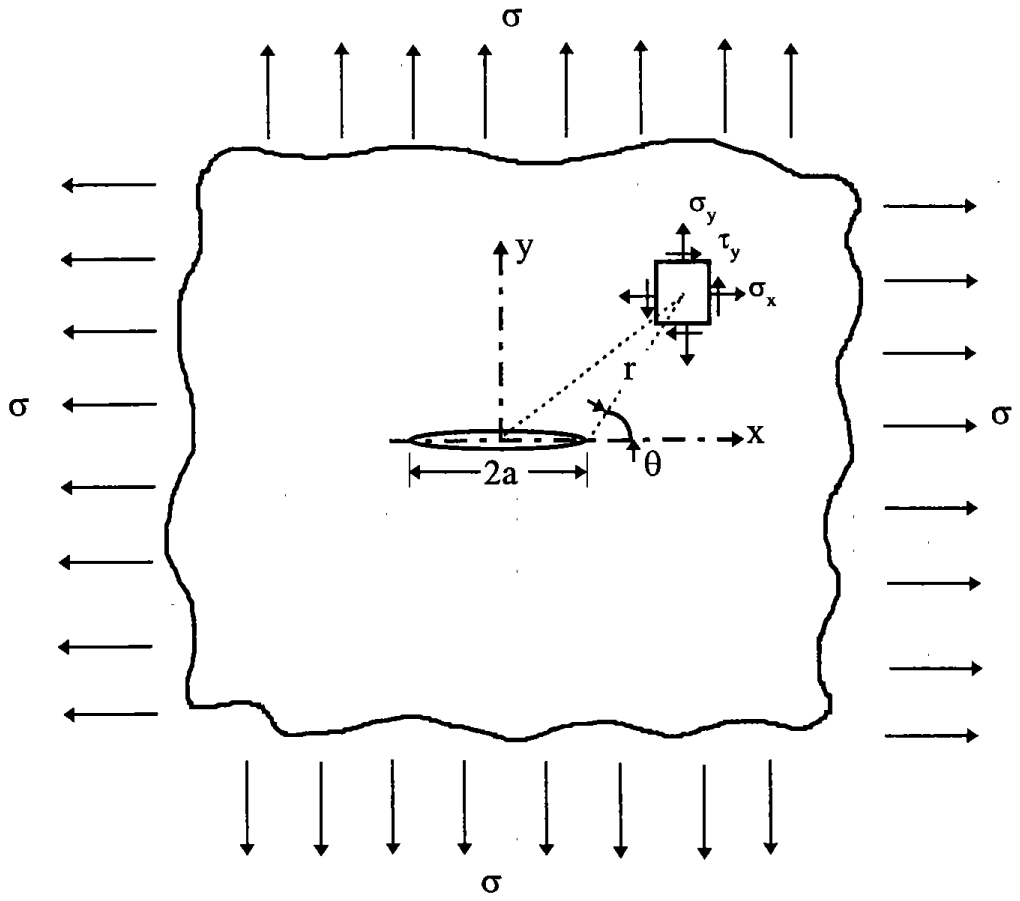

Figure 2.5: A crack of lenght $2a$ in an infinite plate [28]

	Mode I	Mode II	Mode III
σ_{xx}	$\frac{K_I}{\sqrt{2\pi r}} cos\frac{\theta}{2}\left[1 - sin\frac{\theta}{2} sin\frac{3\theta}{2}\right]$	$-\frac{K_{II}}{\sqrt{2\pi r}} sin\frac{\theta}{2}\left[2 + cos\frac{\theta}{2} cos\frac{3\theta}{2}\right]$	0
σ_{yy}	$\frac{K_I}{\sqrt{2\pi r}} cos\frac{\theta}{2}\left[1 + sin\frac{\theta}{2} sin\frac{3\theta}{2}\right]$	$\frac{K_{II}}{\sqrt{2\pi r}} sin\frac{\theta}{2} cos\frac{\theta}{2} cos\frac{3\theta}{2}$	0
τ_{xy}	$\frac{K_I}{\sqrt{2\pi r}} cos\frac{\theta}{2} sin\frac{\theta}{2} cos\frac{3\theta}{2}$	$\frac{K_{II}}{\sqrt{2\pi r}} sin\frac{\theta}{2}\left[1 - sin\frac{\theta}{2} sin\frac{3\theta}{2}\right]$	0
σ_{zz}	$\begin{cases} 0 & plane\ stress \\ \nu(\sigma_{xx} + \sigma_{yy} & plane\ strain \end{cases}$	$\begin{cases} 0 & plane\ stress \\ \nu(\sigma_{xx} + \sigma_{yy} & plane\ strain \end{cases}$	0
τ_{xz}	0	0	$-\frac{K_{III}}{\sqrt{2\pi r}} sin\frac{\theta}{2}$
τ_{yz}	0	0	$\frac{K_{III}}{\sqrt{2\pi r}} cos\frac{\theta}{2}$

Table 2.1: Stress fields ahead a crack tip for modes I, II, III [28]

Relationship Between G and K To recapitulate, G is the energy required for an incremental growth of a crack and K describes stresses and strains around the crack tip. The relation between these in a plane stress state with a isotropic material is

$$G = \frac{K_t^2}{E} \tag{2.15}$$

showing that the G and$K$ values are linked through the stiffness of the material. This is useful for determining the stress intensity factor for a cracked specimen from compliance measurements and conversely for assessing the compliance of a cracked specimen.

Extended Finite Element Method

The extended finite element method (XFEM) is a way of modeling failure and crack growth using finite element analysis. Compared to other methods it is less mesh dependent and it allows solution dependent crack initiation as well as growth. This is achieved with an extension to ordinary FEA by enriching elements with additional degrees of freedom and shape functions. The enrichment allows discontinuities, such as cracks, without predefining crack location, without remeshing the model and it does not require the mesh to match the geometry of the discontinuity. The fact that there is minimal need for remeshing and that the solution is rather mesh independent means good results even for a coarse mesh. This makes XFEM relatively computationally inexpensive [26].

For the analyst, this means that setting up the analysis requires less knowledge of the crack propagation in the specimen, as the crack initiation and growth is solution dependent. The method has been proven to exhibit nearly no mesh dependence if the mesh is sufficiently refined [24]. A failure criterion as well as a damage evolution law has to be established by the user, making the material model somewhat more complex. The regions in which cracks are expected to occur must be defined as enriched regions. These regions are evaluated for crack initiation or growth, using the failure criterion, throughout the analysis. Otherwise the model is created and meshed as any other FEM model; some program specific limitations may apply to the use of XFEM however.

Enrichments The aforementioned enrichments are simply two extensions to the equation for the displacement vector used in ordinary FEM. These extensions represent the added displacement due to discontinuous geometry and the asymptotic stress around the crack tip. For the total displacement, the function is given by the Abaqus Analysis User's Manual [24] as:

$$u = \sum_{I=1}^{N} N_I(x) \left[u_I + H(x)a_I + \sum_{\alpha=1}^{4} F_\alpha(x) b_I^\alpha \right] \tag{2.16}$$

where

$N_I(x)$ are the usual nodal shape functions

u_I is the usual nodal displacement vector associated with the continuous part of the finite element solution

$H(x)$ are the jump functions across crack surfaces, described in equation 2.17

a_I is a nodal enriched degree of freedom vector

F_α are the elastic asymptotic crack-tip functions, described in equation 2.18

b_I^α is a nodal enriched degree of freedom vector

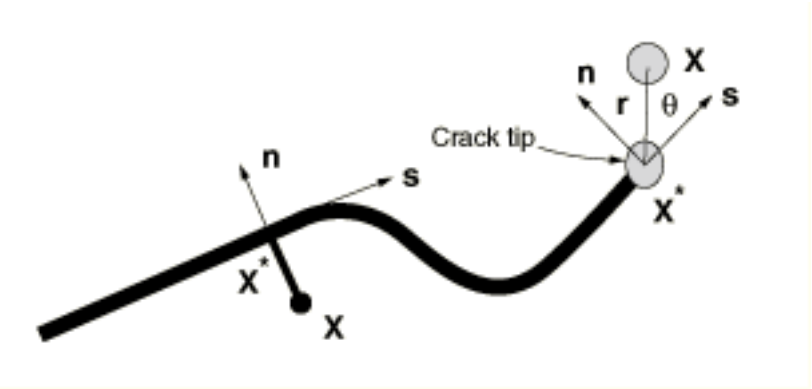

Figure 2.6: Illustration of normal and tangential coordinates for a smooth crack [24].

The first term on the right-hand side is applicable to all the nodes in the model; the second term is valid for nodes whose shape function support is cut by the crack interior; and the third term is used only for nodes whose shape function support is cut by the crack tip [24].

Figure 2.6 shows the discontinuous jump function accross the crack surfaces $H(x)$. This function is given by

$$H(x) = \begin{cases} 1 & if\,(x - x*)n \geq 0 \\ -1 & otherwise \end{cases} \tag{2.17}$$

where
x is a sample point
$x*$ is the point on the crack closest to x
n is the unit outward normal to the crack at $x*$

The figure also illustrates the functions for the asymptotic crack tip, that were described in paragraph 2.2.2, in an isotropic elastic material and are given by

$$F_\alpha(x) = \left[\sqrt{r}sin\frac{\theta}{2},\ \sqrt{r}cos\frac{\theta}{2},\ \sqrt{r}sin\theta sin\frac{\theta}{2},\ \sqrt{r}sin\theta cos\frac{\theta}{2}\right] \tag{2.18}$$

where $(r,\ \theta)$ is a polar coordinate system with its origin at the crack tip and $\theta = 0$ is the tangent to the crack at the tip [24].

Yielding for Anisotropic Metals

The commonly used yield criterion for anisotropic metals is called the Hill criterion. It is an extension of the Mises criterion for isotropic material. While both criteria describe yielding in metals, the Hill criterion has applications for wood under certain load situations as explained in the introduction of subsection 2.2.2.

Hill assumes that the material has three mutually orthogonal planes of symmetry at every point; the material is what was defined as orthotropic in subsection 2.2.1. The planes of symmetry meet in three orthogonal directions that may be called the principal axes of anisotropy. These axes directions may vary from point to point in the material. Looking at a single element with Cartesian axes of reference, the plastic potential is expressed. As with Mises, a homogenous quadratic is used. This means that the Bauchinger effect is not accounted for; the yield stress in a direction for tension is the same as for compression [13]. Because of the symmetry assumption, terms in which any one shear stress occurs linearly

must be discarded. Assuming that the superposition of hydrostatic pressure does not influence the yielding, the yield criterion in the quadratic form is

$$2f \equiv F(\sigma_{yy}-\sigma_{zz})^2+G(\sigma_{zz}-\sigma_{xx})^2+H(\sigma_{xx}-\sigma_{yy})^2+2L\sigma_{yz}^2+2M\sigma_{zx}^2+2N\sigma_{xy}^2=1 \quad (2.19)$$

where F, G, H, L, M and N are constants characteristic of the current state of anisotropy. The expression for f takes this form only when the principal axes of anisotropy are used as the axes of reference [13].

If σ_{11}^y, σ_{22}^y and $\sigma_{33}^y$are the tensile yield stresses in the principal axes of anisotropy, it can be shown that

$$\begin{aligned} F &= \frac{1}{2}\left[\frac{1}{(\sigma_{22}^y)^2}+\frac{1}{(\sigma_{33}^y)^2}-\frac{1}{(\sigma_{11}^y)^2}\right] \\ G &= \frac{1}{2}\left[\frac{1}{(\sigma_{33}^y)^2}+\frac{1}{(\sigma_{11}^y)^2}-\frac{1}{(\sigma_{22}^y)^2}\right] \\ H &= \frac{1}{2}\left[\frac{1}{(\sigma_{11}^y)^2}+\frac{1}{(\sigma_{22}^y)^2}-\frac{1}{(\sigma_{33}^y)^2}\right] \end{aligned} \quad (2.20)$$

Similarly, if σ_{12}^y, σ_{13}^y and σ_{23}^y are the yield stresses in shear with respect to the principal axes of anisotropy, then [13]

$$L=\frac{1}{2(\sigma_{12}^y)^2},\ M=\frac{1}{2(\sigma_{13}^y)^2},\ N=\frac{1}{2(\sigma_{23}^y)^2} \quad (2.21)$$

where

σ_{ij}^y is the yield stress when σ_{ij} is applied as the only nonzero stress component

2.3 Abaqus Spesific Theory

There are several limitations in the tools supplied in software like Abaqus FEA. This chapter will discuss these limitations and provide theory for adaptations and workarounds that may be employed.

2.3.1 Elastic Behaviour in Abaqus

Abaqus supports input of material properties for elastic response in an orthotropic material both as compliances and engineering constants. As material properties are commonly given as engineering constants, this approach requires less pre-processing of data. Care must be taken if the local material coordinate system does not correspond to the global coordinate system. The analyst must take special care to ensure that the engineering constants are given for the correct directions. This can be achieved by rotating the coordinate system or by carefully rearranging the engineering constants and using the following equation

$$\frac{\nu_{ij}}{E_i}=\frac{\nu_{ji}}{E_j} \quad (2.22)$$

from Daniel & Ishai [15] to find the correct Poisson's ratios.

It should be noted that the issue of altered directions is especially prevalent when using a cylindrical coordinate system in Abaqus, as the L, R and T-directions are the 3, 1 and 2-directions respectively. Through the use of coordinate system rotation, this can be rearranged so that the L, R and T-directions are the 1, 3 and 2-directions respectively.

The rearrangement is important for the implementation of XFEM, as the crack direction is oriented with respect to the local 1-direction. The following subsection contains more on this.

2.3.2 XFEM in Abaqus

Abaqus has a method based on traction-separation cohesive behaviour and phantom nodes for modeling geometric discontinuities. This allows elements to be split into two separate volumes without remeshing, meaning that cracks do not have to align with element boundaries. Phantom nodes are in essence a second set of virtual nodes that initially are bound to their real parent node with a bond of infinite stiffness.

Once a crack initiation criterion is met, the element splits into two separate volumes. Each volume formed by a combination of some real and some phantom nodes. The bond between the phantom node and its real parent node then gradually weaken according to a cohesive law until the cohesive strength of the cracked element is zero, at which point the nodes move independently of each other. The cohesive law is described in the next subsection.

Figure 2.7 shows how the initial volume to the left is split into the two separate volumes on the right, comprised of both real and phantom nodes. Each volume is considered whole for the purpose of interpolating displacement. The real domain of each volume Ω_o is extended with the phantom domain Ω_P so that the degrees of freedom in the phantom nodes can be used to interpolate with the same shape functions as before the discontinuity was introduced. To realize the jump in the displacement field at the discontinuity, the field is simply integrated only for the area from the side of the real nodes up to the crack surface.

It should be noted that this means that the near-tip asymptotic singularity occurring in the case of LEFM is not considered. Only the displacement jump across a cracked element is considered. Therefore, the crack has to propagate across an entire element at a time to avoid the need to model the stress singularity. This means that Abaqus does not use the last term in equation 2.16 for growing cracks, saving the computational cost of calculating the asymptotic stress field singularity [24].

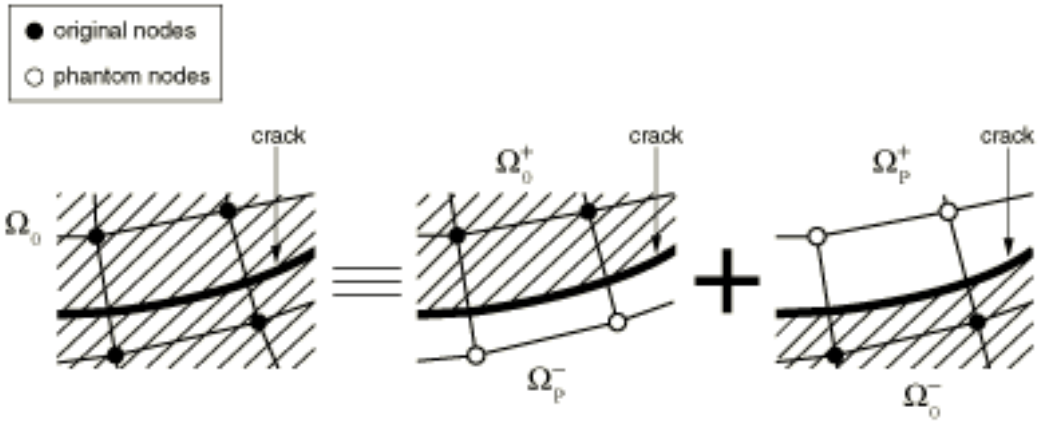

Figure 2.7: Illustration of a cracked element with real nodes and phantom nodes [24]

Crack Initiation

A damage initiation criterion must be defined. Damage initiation refers to the beginning of the degradation of the response in a material point; the process of degradation begins when the stresses or strains met the conditions specified by the criterion.

For use with traction separation, the best available criteria for wood are the maximum nominal stress (MAXS) or strain (MAXE) criteria. Both are defined by the Abaqus Analysis User's Manual [24]. The maximum nominal stress criterion can be expressed as

$$f = max \left\{ \frac{\langle t_n \rangle}{t_n^0}, \frac{t_s}{t_s^0}, \frac{t_t}{t_t^0} \right\} \tag{2.23}$$

where

t_n is the stress component normal to the likely cracked surface
t_s is the first shear stress component on the likely cracked surface
t_t is the second shear stress component on the likely cracked surface
t_n^0 is the maximum allowed stress component normal to the likely cracked surface
t_s^0 is the maximum allowed first shear stress component on the likely cracked surface
t_t^0 is the maximum allowed second shear stress component on the likely cracked surface

The maximum nominal strain criterion can be expressed as

$$f = max \left\{ \frac{\langle \epsilon_n \rangle}{\epsilon_n^0}, \frac{\epsilon_s}{\epsilon_s^0}, \frac{\epsilon_t}{\epsilon_t^0} \right\} \tag{2.24}$$

where

ϵ_n is the strain component normal to the likely cracked surface
ϵ_s is the first shear strain component on the likely cracked surface
ϵ_t is the second shear strain component on the likely cracked surface
ϵ_n^0 is the maximum allowed strain component normal to the likely cracked surface
ϵ_s^0 is the maximum allowed first shear strain component on the likely cracked surface
ϵ_t^0 is the maximum allowed second shear strain component on the likely cracked surface

In both criteria, damage is assumed to begin when f reaches a value of one. Note that the $\langle\,\rangle$signifies that the damage will not be initiated by a pure compressive state.

A tolerance f_{tol} should be specified so that the criterion gets the from

$$1.0 \leq f \leq 1.0 + f_{tol} \tag{2.25}$$

for damage initiation. If f has a value greater than the right side of the equation, the increment is cut back and attempted again.

Data for both ultimate strain and stress is available. As strain fields often are more stable than stress fields in numerical analysis, the MAXE damage criterion has the most attractive properties.

Traction-Separation Law

As mentioned before, a cohesive law governs the weakening of an element after the crack initiation criterion is met. In Abaqus, this is a traction-separation law. The traction-separation behavior assumes linear elastic behavior until the damage initiation criterion is met. As mentioned, the behavior beyond this point the will develop according to a traction-separation law until the element reaches a completely damaged state and a crack is made or propagated.

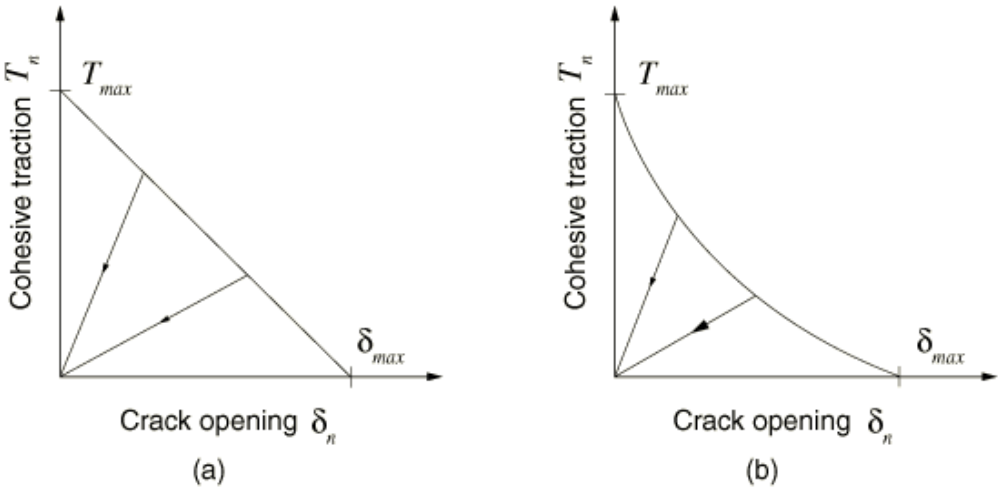

Figure 2.8: Typical linear (a) and nonlinear (b) traction-separation response [24]

Abaqus has both a linear and nonlinear traction separation law built in. User defined laws may also be implemented through the use of tabular data. The traction vector is defined as

$$t = \begin{Bmatrix} t_n \\ t_s \\ t_t \end{Bmatrix} = \begin{bmatrix} K_{nn} & 0 & 0 \\ 0 & K_{ss} & 0 \\ 0 & 0 & K_{tt} \end{bmatrix} \begin{Bmatrix} \delta_n \\ \delta_s \\ \delta_t \end{Bmatrix} = K\delta \tag{2.26}$$

where

t_n is the traction stress in the normal direction
t_s is the first shear traction stress
t_t is the second shear traction stress
δ_n is the separation corresponding to t_n
δ_s is the separation corresponding to t_s
δ_t is the separation corresponding to t_t

Note that the stiffness components are not coupled. Pure normal separation does not give rise to cohesive forces in the shear directions and vice versa. The stiffness terms are calculated from the elastic properties of the enriched element and need not be specified. An example of both linear and nonlinear traction-separation response is shown graphically in figure 2.8 [24].

Damage Evolution

Theory described in section 2.2.2 is applied in Abaqus using energy based damage evolution, which uses energy dissipated as a result of the damage process to calculate damage evolution. This is equivalent to what was referred to as crack-extension force in the LEFM theory and is called fracture energy in Abaqus. The fracture energy is equal to the area under the traction-separation curve in figure 2.8. Fracture energy dependence on the mix of failure modes can be specified using tabular data or by using analytical forms where the mode-mix ratio is defined in terms of energies. For this model, power law mixed mode behavior was selected.

In the power law formulation, the dependence of the fracture energy on the mode mix is defined based on a power law fracture criterion. The power law criterion states that failure under mixed-mode conditions is governed by a power law interaction of the energies required to cause failure in the individual modes. It is given by

$$\left\{\frac{G_n}{G_n^C}\right\}^\alpha + \left\{\frac{G_s}{G_s^C}\right\}^\alpha + \left\{\frac{G_t}{G_t^C}\right\}^\alpha = 1 \tag{2.27}$$

where

G_n is the work done by the traction and its conjugate separation in the normal direction

G_s is the work done by the traction and its conjugate separation in the first shear direction

G_t is the work done by the traction and its conjugate separation in the second shear direction

G_n^C is the critical fracture engery requred to cause failure in the normal direction

G_t^C is the critical fracture engery requred to cause failure in the first shear direction

G_s^C is the critical fracture engery requred to cause failure in the second shear direction

The mixed mode fracture energy $G^C = G_n + G_s + G_t$ when the above condition is satisfied [24].

Damage Stabilization

Material models with softening behavior and stiffness degradation can cause severe convergence difficulties in implicit analysis programs, such as Abaqus/Standard. These difficulties can be overcome by using viscous regularization, which makes the tangent stiffness matrix of the material that is softening to be positive when time increments are sufficiently small. In the regularization scheme, a viscous damage variable is defined by the evolution equation:

$$\dot{d_v} = \frac{1}{\eta}(d - d_v) \tag{2.28}$$

where

η is the viscosity coefficient representing the relaxation time of the viscous system

d is the damage variable evaluated in the original inviscid model

The damaged response of the viscous material is given as

$$\sigma = C_d \epsilon \tag{2.29}$$

where the damaged elasticity matrix C_d is computed using viscous values of damage variables for each failure mode [24].

Restrictions when using XFEM in Abaqus

Certain restrictions apply when using XFEM in Abaqus FEA 6.10-2 [24]:

- Is currently only available for first order stress/displacement solid continuum elements.
- May not be used in a step with adaptive mesh regions; however steps with adaptive mesh regions can be used in the same analysis as steps with XFEM regions.

- Uses only one degree of freedom per node to calculate the displacement field discontinuity and stress field singularity near the tip. This means that cracks may not branch or join with other cracks, unless the model is remeshed to make the crack a part of the model geometry.
- May only be used with tetrahedral elements in three dimensions.
- A crack may not turn 90° within an element; an approximate solution can be achieved with a sufficiently fine mesh.

2.3.3 Hill Anisotropic Yielding

Abaqus uses a slightly modified form of the Hill anisotropic yield criterion: It is not in its quadratic form and the criterion and an arbitrary reference stress called σ^0 is introduced so that the potential function becomes

$$f(\sigma) = \sqrt{F(\sigma_{22}-\sigma_{33})^2 + G(\sigma_{33}-\sigma_{11})^2 + H(\sigma_{11}-\sigma_{22})^2 + 2L\sigma_{23}^2 + 2M\sigma_{31}^2 + 2N\sigma_{12}^2} \tag{2.30}$$

and the F, G, H, L, M and N factors are rewritten and defined as

$$\begin{aligned} F &= \frac{(\sigma^0)^2}{2}\left[\frac{1}{(\sigma_{22}^y)^2} + \frac{1}{(\sigma_{33}^y)^2} - \frac{1}{(\sigma_{11}^y)^2}\right] = \frac{1}{2}\left[\frac{1}{R_{22}^2} + \frac{1}{R_{33}^2} - \frac{1}{R_{11}^2}\right] \\ G &= \frac{(\sigma^0)^2}{2}\left[\frac{1}{(\sigma_{33}^y)^2} + \frac{1}{(\sigma_{11}^y)^2} - \frac{1}{(\sigma_{22}^y)^2}\right] = \frac{1}{2}\left[\frac{1}{R_{33}^2} + \frac{1}{R_{11}^2} - \frac{1}{R_{22}^2}\right] \\ H &= \frac{(\sigma^0)^2}{2}\left[\frac{1}{(\sigma_{11}^y)^2} + \frac{1}{(\sigma_{22}^y)^2} - \frac{1}{(\sigma_{33}^y)^2}\right] = \frac{1}{2}\left[\frac{1}{R_{11}^2} + \frac{1}{R_{22}^2} - \frac{1}{R_{33}^2}\right] \end{aligned} \tag{2.31}$$

$$L = \frac{3}{2}\left(\frac{\tau^0}{\sigma_{23}^y}\right)^2 = \frac{3}{2R_{23}^2},\ M = \frac{3}{2}\left(\frac{\tau^0}{\sigma_{13}^y}\right)^2 = \frac{3}{2R_{13}^2},\ N = \frac{3}{2}\left(\frac{\tau^0}{\sigma_{12}^y}\right)^2 = \frac{3}{2R_{12}^2} \tag{2.32}$$

σ^0 is set by the user and $\tau^0 = \sigma^0/\sqrt{3}$. R_{11}, R_{22}, R_{33}, R_{23}, R_{13} and R_{12} are called anisotropic yields stress ratios. The user inputs an arbitrary σ^0 and then has to caculate the anisotropic yields stress ratios for input according to the following equations [24]:

$$\begin{aligned} R_{11} &= \frac{\sigma_{11}^y}{\sigma^0},\quad R_{22} = \frac{\sigma_{22}^y}{\sigma^0},\quad R_{33} = \frac{\sigma_{33}^y}{\sigma^0} \\ R_{23} &= \frac{\sigma_{23}^y}{\tau^0},\quad R_{13} = \frac{\sigma_{13}^y}{\tau^0},\quad R_{12} = \frac{\sigma_{12}^y}{\tau^0} \end{aligned} \tag{2.33}$$

The evolution of the yielding, or hardening, is then defined by making additional data points consisting of a reference stress and a corresponding plastic strain. For Hill potential without cyclic loading, isotropic hardening is prefered. Isotropic hardening means that the yield surface changes size uniformly in all directions such that the yield stress increases or decreases in all stress directions as plastic straining occurs [24].

2.3.4 Adaptive Meshing

Several types of adaptive meshing techniques can be found in Abaqus.

Arbitrary Lagrangian-Eulerian Adaptive Meshing

This adaptive process is activated in the step module of abaqus. It uses a combination of the features of pure Lagrangian analysis and pure Eulerian analysis and is often called Arbitrary Lagrangian-Eulerian (ALE) analysis. This adaptive meshing algorithm is a tool that maintains a high-quality mesh even when the analysis has large deformations or loss of material, by allowing the mesh to move independently of the material. ALE adaptive meshing does not change topology of the mesh, meaning that this tool has some limitations in its ability to maintain a high-quality mesh when deformations are extreme. In effect, it does not create or remove elements.

For Abaqus/Standard, ALE adaptive meshing can be used to maintain a high quality mesh during large deformation geometrically nonlinear static problems [24].

Adaptive Remeshing

Activation of this tool is done in two steps, first creating a remeshing rule in the mesh module and then an adaptivity process in the job module. Unlike the ALE adaptive mesh, adaptive meshing allows changes in mesh topology. The goal of using this tool is to approach or reach targets on selected error indicators for selected models and load cases, using a minimum of elements. It is typically used for accuracy control, but can also be used for distortion control in some situations. Through iterations of the same job, the process generates several dissimilar meshes to determine a single, optimized mesh that is used throughout an analysis [24].

The use of adaptive remeshing enables the user to obtain a mesh that provides a good balance between solution cost and desired accuracy. According the the Abaqus Analysis User's Manual [24], adaptive remeshing can be helpful when:

- you are unsure how refined a mesh needs to be to reach a particular level of accuracy or how coarse the mesh can be without unacceptably impacting solution accuracy;
- it is difficult to design an adequately refined mesh near a region of interest, such as near a stress riser; or
- you do not know a location of interest, such as with formation of a plastic zone, a priori.

2.4 Other Options for Material Behavior

The reader may be familiar with the works of Tsai and Wu [22], describing an elliptic failure surface for anisotropic materials. Later works by Mackenzie-Helnwein [18] and others have further improved this mathematical model for use with wood. Both these have attractive properties such as accounting for coupling effects, differentiating between tension and compression and the latter even distinguishing between fracture modes. Unfortunately, Tsai-Wu is only available in plane stress states in Abaqus while more complex criteria have yet to be implemented at all. Other options, such as Hashin damage for fiber composites are also restricted to plane stress states [25]. As these criteria are not available for use, theory for them is omitted.

Chapter 3

Modeling

This chapter outlines the creation of the prototype model that would later be calibrated using laboratory tests. The chapter focuses on considerations and simplifications while detailed description of relatively simple modeling steps is omitted.

3.1 Geometry

The prototype was modeled as a reference case for later calibration using three dimensional deformable parts with solid homogenous sections. It was important for the model to be initially simple but with the option to change parameters to make the problem more complicated in later stages.

An overview of the setup of the reference case is shown in figure 3.1 while the geometry of each part is shown in figures 3.2 and 3.3, which also shows the pith locations. These were defined using local material orientations in Abaqus. The stud pith location was chosen due to availability of materials for the laboratory tests and was modeled with a rectangular coordinate system so that the growth rings were diagonal. Note that this simplification gives symmetry about the YZ-plane in the center of the model and allowed the model to be cut in half, saving computational time. The stud was added due to considerations that are discussed in section 3.3.

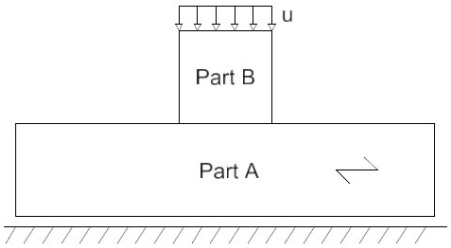

Figure 3.1: Overview of reference case

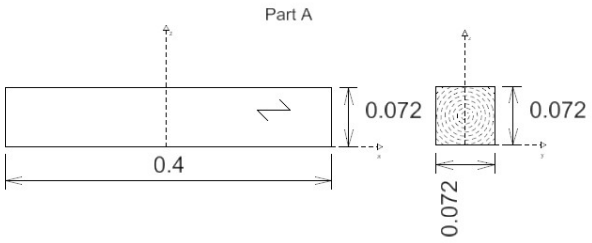

Figure 3.2: Reference case part A dimentions and pith locations

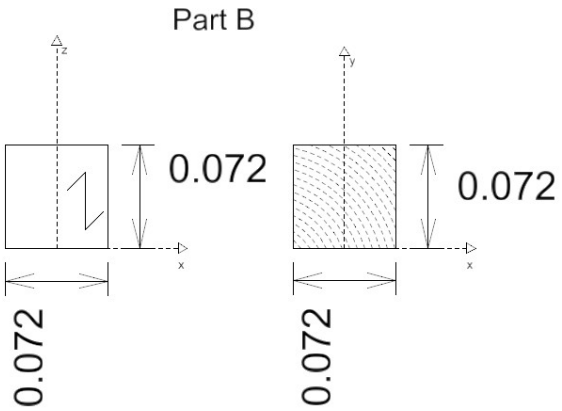

Figure 3.3: Reference case part B dimentions and pith locations

3.2 Material Model

Methods presented in the theory chapter were implemented using the material editor. Clear wood was chosen for two reasons: Because it is somewhat simpler to model than gluelam and because there is more possible variation in properties. Increased variation was expected to make a parameter study more interesting, with more visible differences when changing parameters. The most common quality of clear wood in Norway, C24, was selected.

Since traction-separation has to have a defined crack direction that is either normal or perpendicular to the local 1-direction, different materials had to be made for different parts of the sill and stud. The system was partitioned according to figure 3.4. Parts were numerated for easy reference as shown in the figure. Please refer to the figure for referencing the part names, as these will be used in the text. All the material data used is from sources in the literature.

Properties for a linear-elastic orthotropic behavior were set, using engineering constants, to the same values for all parts. Data from NS-EN 338 [1] are given in table 3.1.

Symbol	$E_{o,mean}$	$E_{90,mean}$	G_{mean}
Value	11000	0.37	0.69

Table 3.1: Elastic stiffness properties (in MPa) for C24 $\rho_{mean} = 420kg/m^3$ [1]

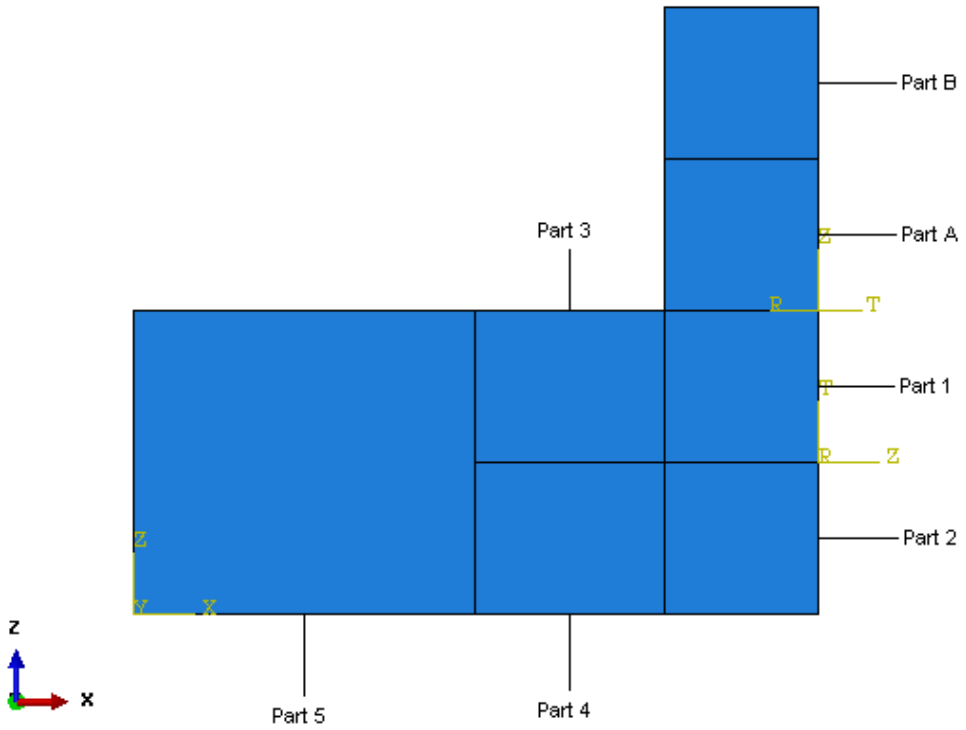

Figure 3.4: Partition geometry and annotations

Symbol	E_{LL}	E_{RR}	E_{TT}	ν_{LR}	ν_{LT}	ν_{RT}	G_{LR}	G_{LT}	G_{TR}
Value	10000	800	400	0.5	0.6	0.6	600	600	30

Table 3.2: Elastic stiffness properties (in MPa) and Poisson's ratios for Norway spruce with $\rho = 400kg/m^3$

Obviously, this is an incomplete data set for a numerical analysis. Table 3.2 contains a complete set of mean values based on the works of Dahl [6].

These are mean values. In an attempt to match the extended data from Dahl to strenght class C24 used in the Eurocode, the elasticity moduli from Dahl were adjusted using the ratio between the densities. Mean shear moduli are defined as

$$G_{mean} = E_{o,mean}/16 \tag{3.1}$$

in the Eurocode [1]. This relation was assumed to hold true for the updated elastic properties so that replacing the adjusted stiffness $E_{0,mean}\frac{420}{400}$ with $16G_{ij}\frac{420}{400}$ yielded

$$G^*_{ij} = G_{ij}\frac{420}{400} \tag{3.2}$$

Poissons ratios were assumed to remain unchanged.

Input values attained from these strategies are shown in table 3.3.

Further properties had to be given specifically to each part. As with the elastic properties the mean values for maximum linear stress, ultimate stress and ultimate strain were based on the works of Dahl [6]. The same strategy of adjusting the values using the ratio between the densities was employed on the stresses. Strains remain unchanged.

Symbol	E^*_{LL}	E^*_{RR}	E^*_{TT}	ν^*_{LR}	ν^*_{LT}	ν^*_{RT}	G^*_{LR}	G^*_{LT}	G^*_{TR}
Value	10500	840	420	0.5	0.6	0.6	630	630	31.5

Table 3.3: Adjusted elastic stiffness properties (in MPa) and Poisson's ratios for Norway spruce with $\rho = 420kg/m^3$

Symbol	$\sigma_{LL,t}$	$\sigma_{LL,c}$	$\sigma_{RR,t}$	$\sigma_{RR,c}$	$\sigma_{TT,t}$	$\sigma_{TT,c}$	σ_{LR}	σ_{LT}	σ_{TR}
Max lin. σ	41.4	-23.2	3.37	-2.66	1.84	-2.39	4.2	3.04	0.93
Ult. σ	63.4	-28.9	4.87	-3.6	2.75	-3.79	6.10	4.38	1.64
Symbol	$\epsilon_{LL,t}$	$\epsilon_{LL,c}$	$\epsilon_{RR,t}$	$\epsilon_{RR,c}$	$\epsilon_{TT,t}$	$\epsilon_{TT,c}$	ϵ_{LR}	ϵ_{LT}	ϵ_{TR}
Ultimate ϵ	.0077	$-.0047$	.0063	$-.0078$	.0114	$-.0201$	.0110	.0082	.0914

Table 3.4: Maximum linear stress, ulitmate stress and ultimate total strain for Norway spruce with $\rho = 400kg/m^3$. Stresses are in MPa ($t = tension$, $c = compression$).

Fracture energy for wood is harder to come by. Some data is available from Schmidt [21], but not for failure perpendicular to the grain. To circumvent this problem, the required fracture energies were extrapolated by assuming a linear relationship between fracture energy and fracture stress. The resulting data is presented in table 3.6.

For all MAXE damage criteria, failure tolerance, described in subsection 2.3.2, was set to 0.05 and cohesive damage stabilization, described in the same subsection, was set to 1×10^{-5}.

3.2.1 Parts 1 and 2

In these parts, it was assumed that there would be primarily ductile compressive failure. Two strategies were attempted for modeling this part.

XFEM

In addition to orthotropic linear-elastic properties, XFEM was activated for the parts and were given a failure criterion in the form of MAXE damage with failure parallel to the local 1-drection. The initial input properties are listed in table 3.5 and were set so that

$$\begin{aligned} \epsilon^0_n &= \epsilon^{ult}_{RR,t} \\ \epsilon^0_s &= \epsilon^{ult}_{LT} \\ \epsilon^0_t &= \epsilon^{ult}_{RT} \end{aligned} \tag{3.3}$$

Tensile strength in the radial direction was chosen because the MAXE damage criterion does not initiate for compressive loading, $\left|\epsilon^{ult}_{RR,t}\right| < \left|\epsilon^{ult}_{TT,t}\right|$ and there was no way

Symbol	$\sigma_{LL,t}$	$\sigma_{LL,c}$	$\sigma_{RR,t}$	$\sigma_{RR,c}$	$\sigma_{TT,t}$	$\sigma_{TT,c}$	σ_{LR}	σ_{LT}	σ_{TR}
Max lin. σ	43.47	-24.36	3.539	-2.793	1.932	-2.510	4.41	3.192	0.977
Ult. σ	66.57	-30.35	5.114	-3.78	2.888	-3.980	6.405	4.600	1.722
Symbol	$\epsilon_{LL,t}$	$\epsilon_{LL,c}$	$\epsilon_{RR,t}$	$\epsilon_{RR,c}$	$\epsilon_{TT,t}$	$\epsilon_{TT,c}$	ϵ_{LR}	ϵ_{LT}	ϵ_{TR}
Ultimate ϵ	.0077	$-.0047$	.0063	$-.0078$	.0114	$-.0201$	.0110	.0082	.0914

Table 3.5: Adjusted maximum linear stress, ulitmate stress and ultimate total strain for Norway spruce with $\rho = 420kg/m^3$. Stresses are in MPa ($t = tension$, $c = compression$).

Symbol	G_I	G_{II}	G_{III}
Parallel to grain	280	770	235
Normal to grain	3650	770	770

Table 3.6: Fracture energy from Schmidt and extrapolations (in Nm/m^2) [21]

to distingush between the two strengths due to the defention of the crack direction; the crack plane could be any plane that is parallel to the grain. The damage evolution was defined using linear energy formulation with maximum degredation and power law behavior. Fracture energies are listed in table 3.6 under "parallel to grain".

This lack of distinciton meant that the effect of growth ring placement would be absent in these parts. In addition, the MAXE criterion does not initiate damage in the normal direction under compressive loading, nor does it initate damage before the ultimate strain. Due to these issues, it was doubtful that this strategy would be able to accurately model the type of ductile compressive yielding that was expected, yet it was attempted anyway.

Hill Anisotropic Yielding

This option was only available with stresses that have to be transformed into R ratios according to equation 2.33 in subsection 2.3.3. The calculated R ratios are given in table 3.7.

Symbol	σ^0	σ^1	ϵ_p^1	σ^2	ϵ_p^2	R_{11}	R_{22}	R_{33}	R_{12}	R_{13}	R_{23}
Value	10	14	.00308	16	.01015	100	.2510	.2793	.5529	.7638	.1692

Table 3.7: R ratios for Hill potential. Note that 2-direction is the tangential direction while the 3-direction is the radial direction. Stresses are in MPa.

It was impossible to distinguish between tension and compression in this definition, so the "end of linear range" (ELR) stresses used to calculate R ratios were picked through study of stress fields from elastic test runs.

It was observed that the hammock effect generated tension in the fibers and that the local bending of the sill also caused compressive stress. However, there should not be much coupling effect between the ductile compressive failure and brittle failure in the fibers. In an attempt to accommodate this, the R ratio for the 1-direction was set to an arbitrary high value. It was discovered during calibration that the difference between R_{22} and R_{33} created issues with negative R ratios, crashing the analysis. To fix it, the ratios were changed so that $R_{22} = R_{33} = 0.251$.

For the radial and tangential directions, the fields again contained both compressive and tensile stresses. Observations of different cuts made it evident that the most significant parts of the stress fields, both in magnitude and size, were of a compressive nature. Compressive ELR strength was used for both directions.

Finally the stress factors σ^x and the ultimate plastic strains ϵ_p^x had to be set. Considering the importance of each strength in each direction, it was chosen to let the plasticity be defined by two points based mainly on the uniaxial compressive strengths in the radial and tangential direction. The data set given in table 3.8 are the input variables used, where σ is arbitrary while ϵ_p is based on ultimate stresses from table 3.5. Note that the two final stress and strain pairs in this data set are simply a linear extrapolation of the

former data pair and a made up pair, respectively. These final pairs were added so that the Hill potential would remain defined for higher stress

Combined Strategy

A final option, combining both XFEM and Hill anisotropic yielding in the parts, was tested using the same data as presented in the two previous subsections.

3.2.2 Parts 3, 4 and 5

In these parts, particularly part 3 and 4, it was assumed there would be primarily brittle tensile failure in the fiber direction. This behavior was modeled using XFEM where, in addition to orthotropic linear-elastic properties, the parts were given a failure criteria in the form of MAXE damage with failure perpendicular to the local 1-drection. The initial input properties are listed in table 3.5 and were set so that

$$\begin{aligned} \epsilon_n^0 &= \epsilon_{LL,t}^{ult} \\ \epsilon_s^0 &= \epsilon_{LT}^{ult} \\ \epsilon_t^0 &= \epsilon_{LR}^{ult} \end{aligned} \tag{3.4}$$

Tensile ultimate strain in the lenght direction was chosen because the hammock effect was expected to cause tensile stress in the fibers. The shear strains were simply input as is.

3.2.3 Parts A and B

The stud was given only orthotropic linear-elastic properties, as it was not the focus of this study; its role was merely application of the load.

3.3 Interactions

The interaction between the sill test specimen and the surface on which it is placed, as well as the interaction between the sill test specimen and the load or surface applying the load had to be considered. Both of these interactions could be described by a contact problem with a tangential friction coefficient or the interaction could be simplified. In this section, the friction approach as well as other simplified approaches where considered using a prototype of the model. The prototype had a course mesh and a material model that only accounted for elastic behavior. While this prototype may not have been an entirely accurate representation of the problem, it provided sufficient accuracy as a placeholder

σ	ϵ_p
10	0.00000
14	0.00308
16	0.01015
32	0.02030
64	0.50000

Table 3.8: Hill potential σ and ϵ_p data pairs. Stresses in MPa

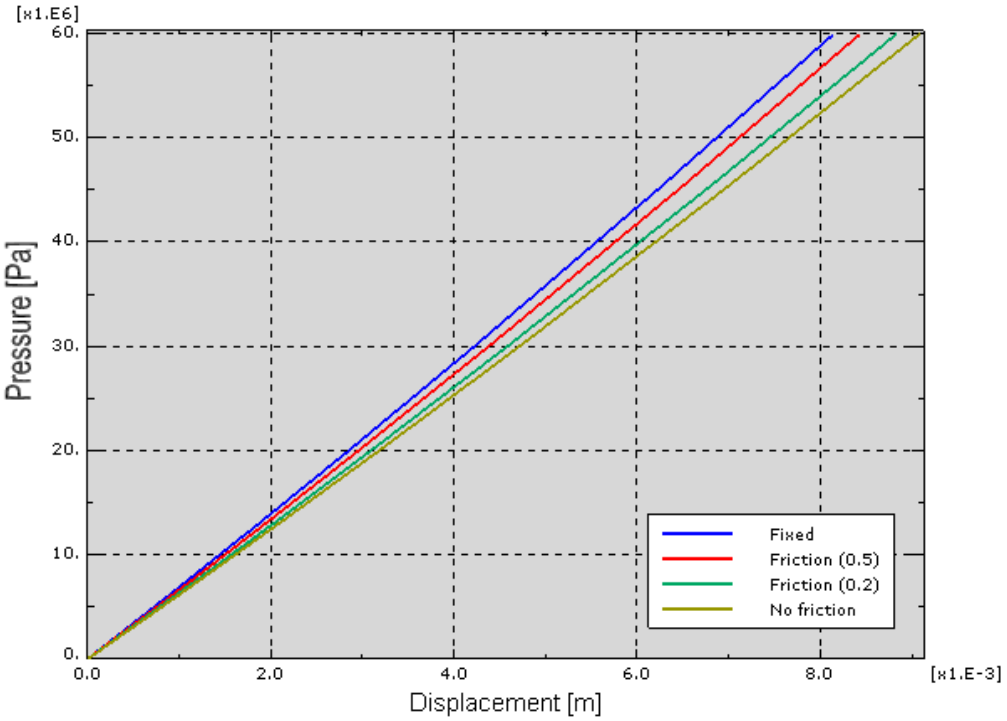

Figure 3.5: Load displacement diagram for different interactions at the bottom of the sill

and demonstrated the difference between the approaches to modeling the interaction. To make the deformations substantial despite only having elastic material laws governing the deformation, the load applied was magnified beyond any realistic loading situation.

3.3.1 Bottom Interaction

Four approaches where attempted in modeling the interaction between the bottom surface of the sill test specimen and the surface whereupon it would be placed. From least to most rigid these are:

- Only vertical DOF is held, this is equivalent to frictionless interaction
- Contact problem interaction with discrete rigid plate, friction coefficient set to 0.2
- Contact problem interaction with discrete rigid plate, friction coefficient set to 0.6
- All DOFs on bottom surface of sill fixed

The results are shown in figure 3.5 as a load-displacement diagram, with displacements extracted from the center point of the loaded zone on the top surface of the sill. It clearly shows that the fixed boundary conditions provided the stiffest response, while the frictionless provided lower stiffness with about 10% greater deformation for the same load. The two approaches using a contact problem with a tangential friction coefficient placed themselves as expected, in between the two extremes. The higher coefficient provided the stiffest response of the two.

Most real world situations would likely have interactions with a certain friction that could best be modeled using a contact problem and a friction coefficient. It is clear that the value of the coefficient is critical for such an interaction. This coefficient can vary

greatly, depending on the material the wooden surface is interacting with and the presence of liquids. As such, the frictionless approach was chosen as it would be a conservative approach.

3.3.2 Top Interaction

Applying the load to the top of the sill test specimen also required some considerations. Several limitations applied:

- The load application would have to be modeled in such a way that it would cause close to the same vertical displacement for all nodes in the loaded zone in the sill. Clearly, a continuous hammock without a sudden change in loading at the end of the loaded zone would not account for the complicated stress situation that should occur.
- As the surfaces in question would be moving during the analysis, using a contact problem formulation could cause severe convergence problems.
- The surface to which load was applied was a part of a region that was to use adaptive meshing, XFEM or both. Tests done using a tie constriction between any surface that was part of an adaptive mesh region and a rigid body in the model caused program errors.

These restrictions obviously made direct application of a pressure load, use of rigid bodies tied to the model and any approach using contact problems unviable solutions. The viable solutions that remained were:

- Tie a wooden stud to the loaded zone, with grain in the load direction (global Z-direction), and apply the load through it by applying pressure or displacement directly to the top of the stud.
- Use displacement control directly on the loaded zone of the sill.

The two approaches are compared in the load displacement diagram in figure 3.6. Note that the model featuring the wood stud was run both as a load controlled and a displacement controlled analysis. The model featuring the stud gave a slightly stiffer response than the model without the stud. However this difference varied with where on the loaded surface displacement history was extracted.

Unlike the bottom interaction, where the exact real world situation was unclear, it was easier to decide on a strategy for modeling the top interaction. The case of pressure perpendicular to the grain on a wood sill obviously occurs most frequently in wooden structures and in such structures the load would usually applied through a wood stud. Due to the microstructure of wood, the fiber-ends of the stud would lock into small grooves in the sill surface. The tie constraint between the stud and the sill is therefore a good simplification. Finally, displacement control was chosen as it is better for stable load-displacement response which would be important with the implementation of XFEM.

The total displacement applied to the top surface for the final model was set to 1mm.

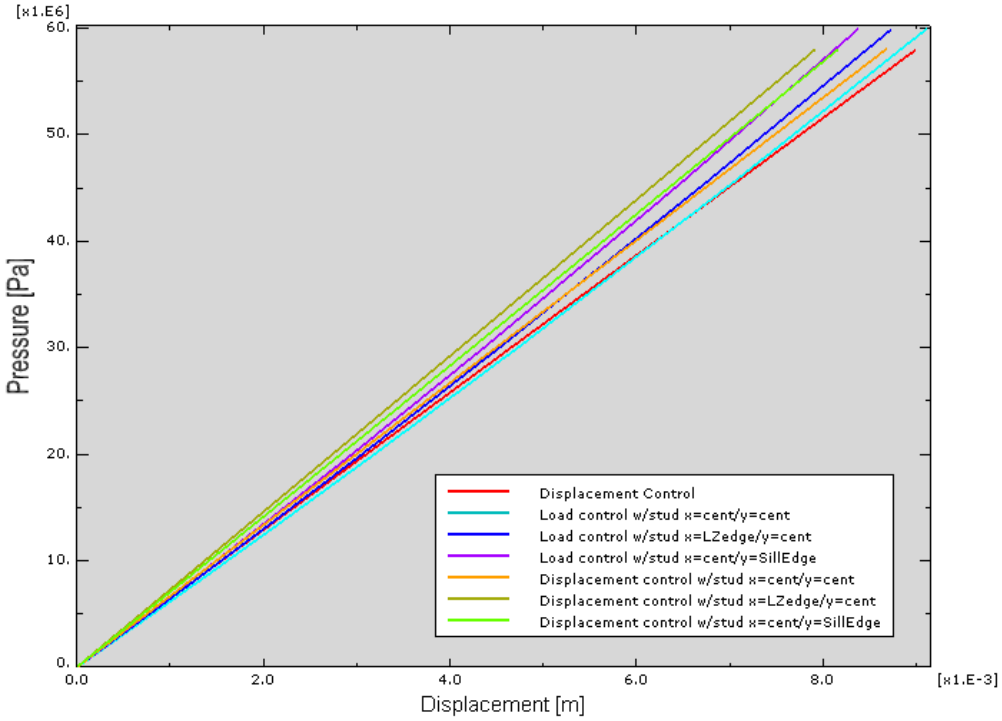

Figure 3.6: Load displacement diagram for different interactions at the top of the sill

3.4 Meshing

The mesh used in the interaction tests was clearly not ideal for the model. Firstly it used the wrong type of elements, as XFEM is only available for tetrahedral elements in 3D. Furthermore the mesh should be biased, so that the mesh would be finer close to interesting areas where stress situations was likely to become complex. A mesh convergence test was run testing a total of six meshes described in table 3.9. Figure 3.7 shows how edges where seeded for meshes 2, 3, 4 and 6. In the figure, the numbers are factors for the edge seeds. A factor of 1 means the edge was seeded with the minimum element size, while a factor of 2 means it was seeded with twice the minimum element size and so on. Edges with bias have two factors, representing the minimum and maximum element size on the biased edge. Please note that mesh tests were run with a model prototype that had a height and width of 90mm. When the model was scaled down to 72mm, all element sizes were scaled using the ratio between the two model sizes.

Additional comments:

Mesh	Seed	Bias	Min. ele. size	Element type
#1	Global	no	4.5mm	Quadratic hex
#2	Local	yes	2.25mm	Linear tet
#3	Local	yes	1.6875mm	Linear tet
#4	Local	yes	1.125mm	Linear tet
#5	Local	yes	1.125mm	Linear tet
#6	Local	yes	0.84375mm	Linear tet

Table 3.9: Tabular data for meshes

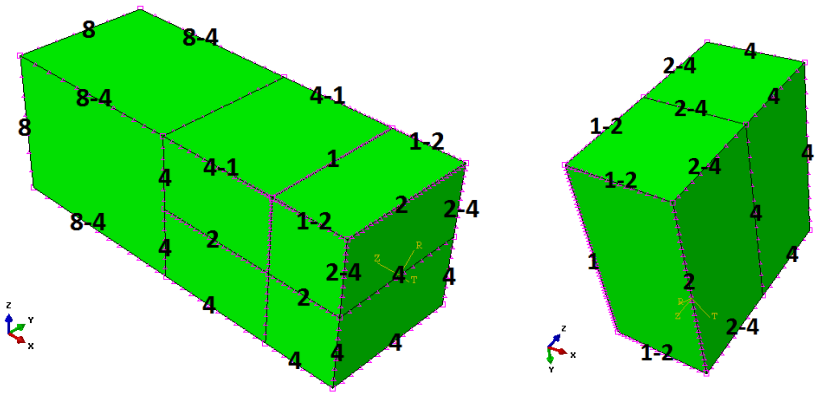

(a) Sill edge seeds (b) Stud edge seeds

Figure 3.7: Edge seeds for model. Numbers are factors that were multiplied with minimum element size. Edges with two numbers are biased, edges that are not seen have seeds to match adjacent edges.

Mesh #	Min element size	Total RF	Max logarthmic strain	Wallclock Time
2	2.25mm	213086N	0.0727435	254 sec
3	1.6875mm	211004N	0.0785629	710 sec
4	1.125mm	207036N	0.0815872	5075 sec
6	0.84375mm	203657N	0.0900482	9331 sec

Table 3.10: Data from mesh tests

- Mesh 1 was a test run with quadratic elements, XFEM is unavailable for quadratic elements.
- Mesh 5 used an alternate bias setup. It was discarded as it gave little accuracy but cost a lot of analysis time.

All meshes where given an 8mm downward vertical displacement if the sill top. Reaction forces where extracted from meshes 2, 3, 4 and 6. As the displacement obviously was the same for all meshes, the reaction force would be a measure of the stiffness of the model as a whole. In addition, the maximum principal logarithmic strains at the center of the edge marking the intersection between parts 1, 3 and A were extracted. These strains, along with the reaction forces and wallclock time of each analysis are shown in table 3.10. Wallclock time is the real time elapsed during an analysis.

Plots of the reaction forces to minimum element size and the logarithmic strain to minimum element size, from the location described, are shown in figure 3.8 and figure 3.9. Table 3.11 shows the relative difference in reaction forces and wallclock time between different meshes. From these data, it was hard to spot any convergence in the results with respect to the element size, especially with the logarithmic strain where the differences are significant. It was concluded that logarithmic strain is unsuitable for mesh convergence tests because the position of the node from which the data was extracted changed with mesh size, as the node has to be part of the mesh geometry. The stiffness, represented by reaction force at a set displacement, was therefore the variable used for mesh evaluation. Through an evaluation of the percentage change of reaction forces between the meshes, it was decided that mesh 3 gave sufficient accuracy at a reasonable computational time cost.

	Wallclock δt	δRF	$\%\delta$	$\frac{\delta t}{\lvert\%RF\rvert \cdot 100}$	δLE	$\%\delta$	$\frac{\delta t}{\lvert\%LE\rvert \cdot 100}$
$\#2 - \#3$	456 sec	-2082N	-0.98%	466.7 sec	0.0058	8.00%	58.34
$\#3 - \#4$	4365 sec	-3868N	-1.88%	2321.15 sec	0.0030	3.85%	602.97
$\#4 - \#6$	4256 sec	-3379N	-1.63%	2607.71 sec	0.0085	10.37%	251.45
$\#2 - \#6$	9077 sec	-9429N	-4.42%	2051.31 sec	0.0173	23.79%	86.23

Table 3.11: Differences due to different mesh topologies. # are the mesh numbers

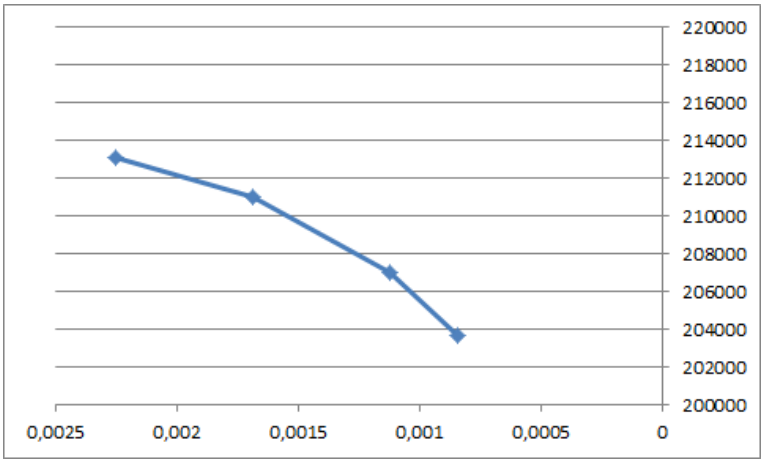

Figure 3.8: Plot of minimum element size to reaction force for meshes 2, 3, 4 and 6

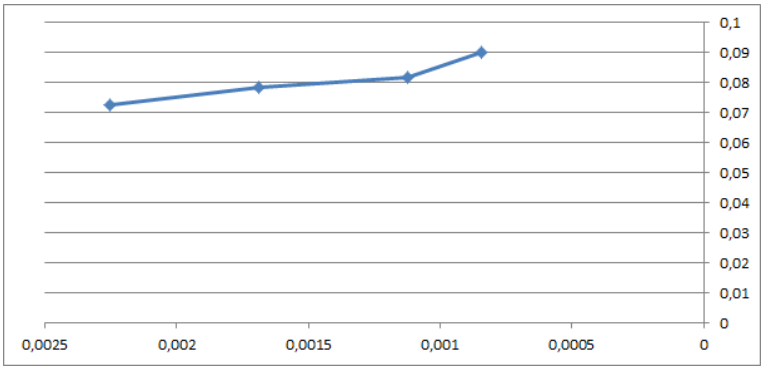

Figure 3.9: Plot of minimum element size to logarithmic strain for meshes 2, 3, 4 and 6

Mesh 2 was used for initial testing of XFEM implementation, but only mesh 3 was properly tested with XFEM as the non-linear material response and damage response increases the cost of a finer mesh significantly. Testing the finer meshes with XFEM was not considered necessary as XFEM shows very little mesh dependence as long as the mesh is refined enough [24].

The final mesh, mesh 3, was further refined slightly by seeding the inside edges created by partitioning the sill. This was done to ensure small enough elements size throughout the volume of the sill in interesting areas.

3.5 XFEM

A crack had to be created in the interaction module. Instabilities in the crack growth in parts 1 and 2, described further in section 5.1, caused the analysis to abort prematurely. This made the first strategy from subsection 3.2.1 less attractive, so an adjusted case deactivating XFEM for the part while not changing the material model was added to the cases to be run through calibration. The effect of this with respect to the damage initiation and development in region 1 and 2 was unknown at the time, but because of weaknesses explained in subsection 3.2.1, it was expected to play a lesser role as the damage initiation criterion does not activate with compressive forces. Thus, only shear cracks and weakening could happen in these regions when XFEM was to be active. Final decisions about the material modeling of parts 1 and 2 were as such postponed till the model calibration. This process is described in 6.

No crack location was specified and no interaction properties were given.

3.5.1 Customizing Steps and Solution Controls

Introducing XFEM called for some customization of solution controls and increment sizes. Experience attained through running analyses showed that the load increment needed to be very small upon damage initiation and crack propagation to be within the tolerance set in the material model. This proved to be very demanding in terms of time use, so the following customizations where done to achieve convergence and keep time consumption down:

Step and Incrementation

Load application was split into two steps. The first step was set to only apply a displacement which initial testing indicated was right before increment time cutbacks began due to damage initiation. As the step only had linear-elastic deformations, increments were set to a constant 0.1. Further displacement up to a total of 2mm was applied in the second step with time increments starting at 0.05, allowing for increments down to 1×10^{-30}. As total displacement was changed to 1mm at a later stage, the initial increment was set to 0.1. This made having two steps unnecessary, so the steps were remerged for convenience.

Solution Controls

Several adjustments were made to the solver controls. These can be accessed in the step module. Discontinuous analysis was activated in the controls. Other modifications are listed by suitable categories:

Quasi-Newton and Line Search A quasi-Newton solution technique was prescribed to all steps. Brittle materials have sharp discontinuities in stiffness as the material cracks, potentially requiring several expensive iterations to form the stiffness matrix. It was hoped that using quasi-Newton along with more line search iterations, employing a stricter convergence criteria for the line search iterations, would save computational time while maintaining convergence. Activating quasi-Newton is done by editing a step while changing line search controls is done by editing the general solution controls. These controls were set according to recommended settings from the Abaqus Analyst user manual. For analyses with severe discontinuities, it is recommended to set N_{ls} to 10 and η_{ls} to 0.01. Nls is the maximum number of line search iterations and nls is the ratio of new to old correction scale factors below which line searching terminates [24].

Maximum Cutbacks Damage initiation and crack propagation required the increment size to drop significantly from one increment to another. In some cases, this required a lot of cutbacks. The maximum number of cutbacks in Abaqus, denoted I_a, has a default value of 5. As the default number of cutbacks proved to be insufficient, it was was changed so that $I_a = 30$. This high number of cutbacks proved to be necessary only for early versions of the model.

Cutback Factors Test runs showed that the cutbacks in increments were sudden, severe and short lived. As damage was initiated, the increment size was required to drop close to the minimum determined in the step editor. To save computational time, it was attempted to makke this drop require fewer attempts with following cutbacks by lowering the cutback factors in the solution controls: The cutback factors for when the solution was diverging, when too many iterations were used due to discontinuities and when elements calculations had problems in large displacement-problems, D_f, D_s and D_h respectively, were set to 0.1 from a default of 0.25. The effect was lesser than desired as the majority of the cutbacks was from the damage tolerance being exceeded, in which case the solver calculates a cutback factor depending on how much the tolerance was exceeded. It was also considered to increase the increase factors for when the solution was converging rapidly or consistently converging over several increments. This was not done as it was likely to cause premature increment increasing with following cutbacks; using time instead of saving it.

Chapter 4

Laboratory tests

To properly test the model accuracy, it was desired to run a series of laboratory tests varying parameters in the setup. The different setups were to generate data sets that could be used in the initial calibration of the reference model, further parameter studies to check the robustness of the model and yield interesting data in themselves. While an outline of the separate tests is given here, please refer to Appendix A for a complete set of figures showing setup and geometry for each test. There was a total of 10 different test setups and each setup was to be tested with 11 specimens.

4.1 Material

As decided in chapter 3, clear wood of strength class C24 was selected for testing as it is the most commonly used strength class for clear wood in Norway. Variation in density and moisture, as well as occurrence of knots was to be avoided; flawless specimens were desired.

4.1.1 Moisture

Moisture content in wood varies with climate, in other words the humidity in the surroundings. Up to fiber saturation at about 30% moisture content [27], the stiffness of the material decreases as the moisture content increases. Under the fiber saturation point, the wood will shrink and swell with varying moisture. Because of the orthotropic properties of wood, the deformation may be significantly different in the different directions. This can cause cracking.

To get good results that correspond to the data input in the model, it was desired to have approximately the same moisture content for all the samples. The Eurocode uses data assuming a moisture content of 12% which is consistent with a temperature of 20^oC and a relative humidity of 65% [2]. Values close to this were desired for the tests, so all specimens were stored in a room held at the temerature and relative humidity prescribed by the Eurocode for an extended period of time.

All the specimens had their moisture content measured with a Wagner L612 digital moisture meter. Measurements were taken at both ends of the sills and studs, the average of the values were recorded. As this measurement might not have been as accurate as desired, another set data for specimens stored in the same room created by Line Sigbjørnsen was used as reference: Using the Wagner on 56 specimens yielded an average moisture content of 12.4% while calculations done by drying 168 $20 \times 20 \times 25mm$ cubes

yielded an average moisture content of 11.34% [23]. As these measurements were done on GlueLam, some of the error could be caused by the presence of an adhesive. Such an error would obviously not be present in these measurements. Even so, it was taken into account that the Wagner might overestimate the moisture content.

4.1.2 Density

Density has a great impact on both the strength and stiffness properties of wood. Among other things, difference in density comes from ratio between earlywood and latewood. Latewood is both denser and stronger than earlywood, so more latewood means wood with higher density and strength. As shown in section 3.2, the parameters used in the model are for wood with a density of $\rho = 420kg/m^3$ which was obviously the desired density of the test samples. Density as defined by the Eurocode can be calulated as [17]:

$$\rho_w = \frac{m_w}{v_w} \tag{4.1}$$

where

ρ_w is the density of the undried specimen
m_w is the mass of the undried specimen
v_w is the volume of the undried specimen

The scales used was a Mettler PM6000 that gave an error of $\pm 0,5g$, the caliper used for messurements below 15cm was a Mitutoyo CD-15D that gave an error of $\pm 0,2mm$. For messurements greater than 15cm, an ordernary tape measure was used giving an error of $\pm 0,5mm$.

For specimens with a moisture content other than 12%, but between 7% and 17%, the density was adjusted using the a correction formula [17]:

$$\rho_{12\%} = \rho_w \cdot 1 - \left(\frac{(1-K)(w-12\%)}{100\%} \right) \tag{4.2}$$

where

ρ_w is the density of the undried specimen
K is a coefficient for volume shinkage set to 0.5 for wood growing in Scandinavia
w is the moisture content in percent

4.1.3 Pith Location

As pith location was of importance for these test, it had to be measured in the test specimens to have a frame of reference as pith location would likely not be perfect for many of the specimens.

In the specimens containing the pith, the YZ-coordinates were simply measured using a caliper. For specimens without the pith in the cross-section, a cardboard circle with a radius of 5 or 10cm was matched with a suitable growth ring. Using measurements of this growth rings placement in the specimen and simple arithmetic, it was possible to come up with an approximate pith location.

4.1.4 Sources of Error

Knots were avoided as much as possible when making the specimens, but could not be avoided altogether. Piths were not as accurately placed in the specimens as desired. Since

the piths more often than not were not in the piece of wood from which the specimen was cut, accurately determining the pith location was difficult.

All sill and stud specimens were weighed and tested for moisture content. This allowed density to be adjusted to 12% moisture content, causing some error through conversion. While most of the specimens for each individual test came from the same piece of wood, some tests used specimens from several different pieces of wood.

Variations in the stud dimensions, making them imperfect cubes, might have caused either more or less favorable stress situations than in the idealized numerical case.

4.2 Execution of Tests

Ten test configurations were run. A tabular overview is shown in table 4.1, while Appendix A has a full set of figures showing geometry and test setup for all tests. Note that the pith locations in Appendix A and in table 4.1 are approximate. Measurements of pith location from each specimen can be found in appendix D. It was difficult to accurately measure the pith location on the majority of samples, as the pith was not in the sample, making the measured pith locations somewhat inaccurate.

Test		Sill dimentions [mm]			Pith coordinates [mm]		Load case
#	ID	h	b	l	Y	Z	Stud location
1	N-Pc-Lc	72	72	400	0.0	-50	Center of sill
2	N-Pe-Lc	72	72	400	-37.5	0.0	Center of sill
3	N-Pb-Lc	72	72	400	0.0	-50	Center of sill
4	N-Pa-Lc	72	72	400	0.0	122	Center of sill
5	N-Pc-Lh	72	72	400	0.0	50	Edge 45mm from sill edge
6	N-Pc-Le	72	72	400	0.0	50	Edge at sill edge
7	N-Pb-Lh	72	72	400	0.0	-50	Edge 45mm from sill edge
8	N-Pb-Le	72	72	400	0.0	-50	Edge at sill edge
9	D-Pb-Lc	144	72	800	0.0	-50	Center of sill
10	H-Pb-Lc	36	72	400	0.0	-50	Center of sill

Table 4.1: Overview of tests. All dimensions are in mm, origin for pith coordinates is shown in figure 3.2

4.2.1 Setup

The setup used is shown in figure 4.1 while figure 4.2 shows a zoomed in view of a sill being compressed. An Instron 5982 was used for compressing the sills. This test machine has a maximum load of $100kN$, Tests were run at a speed of $1mm/min$ up to an extension of $11mm$. Load measurement was calibrated when the load application piston was hanging free, while the extensimeter was calibrated to zero when touching the top of the stud at the start of the first test in each set.

4.2.2 Boundry Conditions and Gathering of Data

All test specimens were placed on a 18mm steel plate covered with a teflon sheet, seen as a white sheet in figure 4.1, to mimic the zero friction interaction of the numerical model.

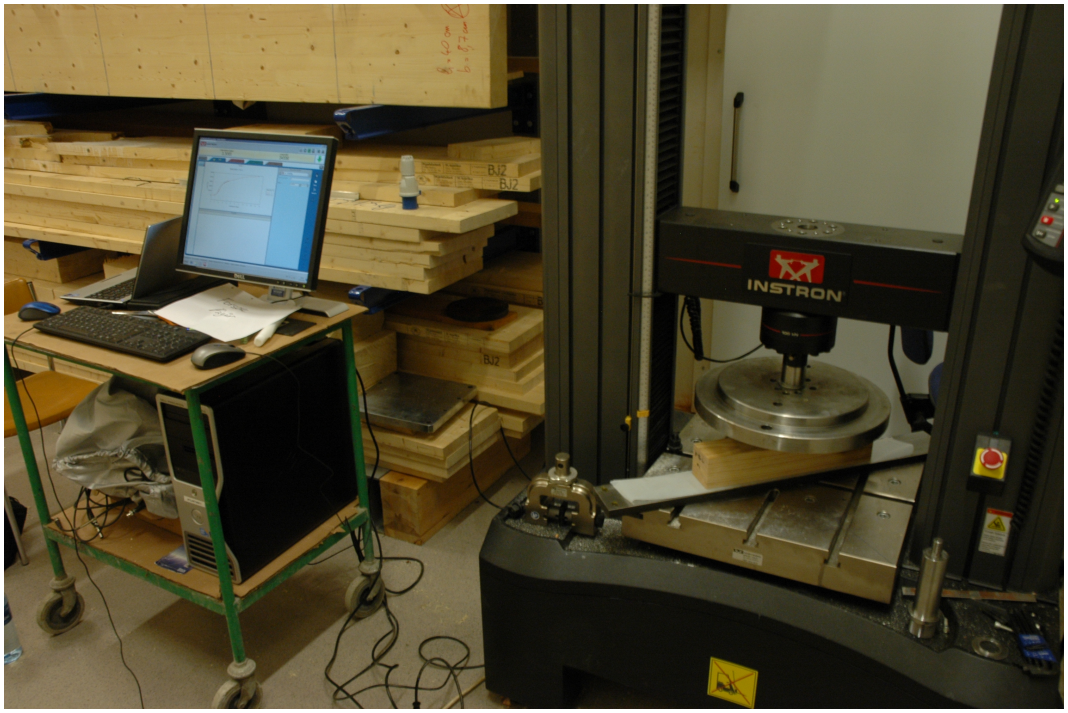

Figure 4.1: Overview of the laboratory test setup

Figure 4.2: Sill being compressed in the testing machine

Load and extension was measured using the integrated functions in the test machine, and were recorded using Bluehill software for static testing. The testing system had an extension measurement accuracy at $\pm 0.01mm$ or 0.05% of displacement (whichever is greater) and a load measurement accuracy at $\pm 0.4\%$ of reading down to1/100 of load cell capacity [14].

4.2.3 Sources of Error

Despite taking care to measure load placements as accurately as possible, it was impossible to execute each individual test in any test configuration exactly the same. While the test machine in itself was quite accurate, the pressure plate seemed to apply the load somewhat unevenly. Finally, this was not an ideal case like the numerical model so any gaps in the mechanism of the test machine and in the sill-stud setup will have to be closed before the test properly begins.

4.3 Test Results

The full sets of measurements and recorded data from the tests in full can be found in the electronic Appendices D and E, respectively. This section contains plots and short evaluations and comments on the data recorded. All test displacement data was normalized so that initial extension was zero. Displacement was measured at the top of the stud.

Most samples had a plateau in the load-displacement diagram up too at least 0.5mm extension. This was likely due to gaps closing in the test mechanism and setup. This area was cleaned out from all graphs used in this paper, but the data for these areas was not deleted and can be found in AppendixE.

Some of the tests had no clear elastic area; the load-displacement curve was S-shaped. Inspecting test runs made it clear that there were gaps in the stud-sill interaction that closed about halfway through the elastic range. This seemed to be caused by imperfect geometry in the test specimens. Uneven load distribution might have caused the tests to give a slightly softer response than what was expected.

Material for the sills and studs was extracted from a total of seven whole clear wood pieces. In this paper, densities and moisture content is given as an average and sample standard deviation for each of these pieces. Average adjusted density and sample standard deviation is also given for each individual test. To see from what piece each individual specimen was extracted, please reference Appendix D. This Appendix also contains individual mesurements of dimensions, pith locations, densities and moisture content for all sills and studs used in testing.

Finally, not all tests listed were completed due to lack of material with correct pith locations. Some of the tests have less than 11 specimens for the same reason.

4.3.1 Load-Displacement Diagrams

N-Pc-Lc

Test load-displacement diagrams are shown in figure 4.3.

This test contained only two test specimens, due to a lack of test specimens with the pith in or near the center of the sill. While there were not enough specimens to make up a complete set, it was decided to run the test anyway. The data was not complete enough to say much about strength or load-displacement response, but the specimens were checked for cracks or failure modes unique to the test configuration. However, nothing of interest was noted.

Densities were below the mean for the wood quality, which means the stiffness and strength was expected to be lower than average.

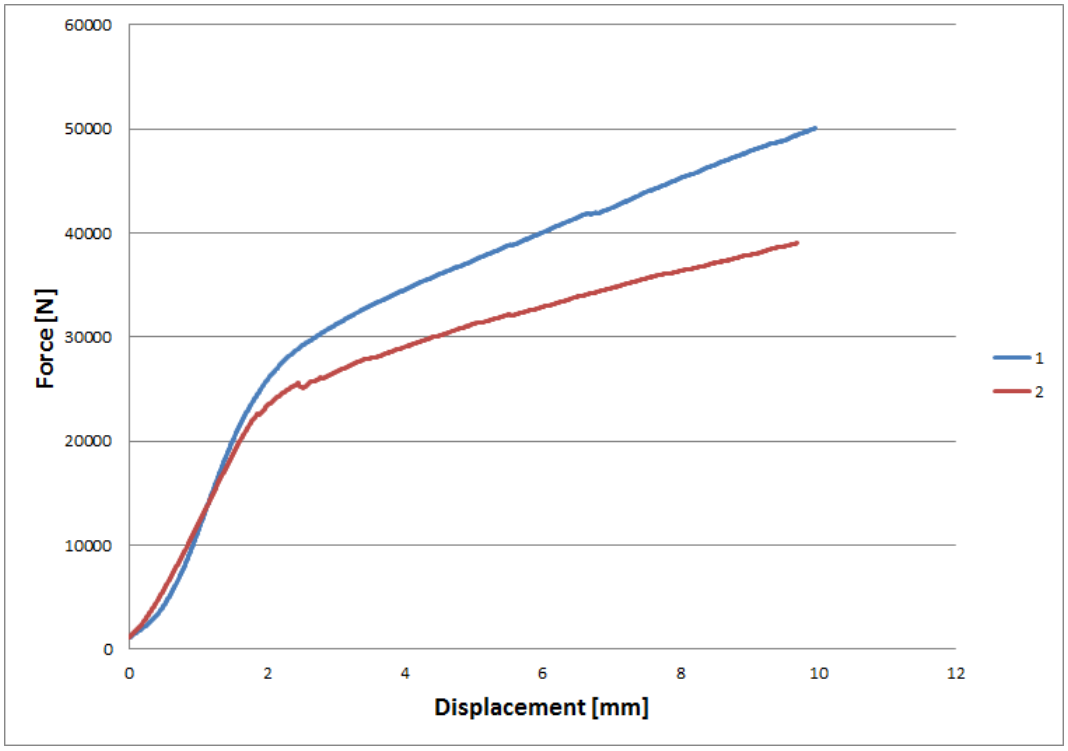

Figure 4.3: Load-displacement for case N-Pc-Lc

N-Pe-Lc

Test load-displacement diagrams are shown in figure 4.4.

Specimens in this test generally had a lower density than the average. Furthermore, none of the specimens had the pith in the desired location and some were quite far off. This was expected to cause more difference between specimens, as specimens with pith far to the side but in line with the bottom edge would have a response dominated by behavior tangential to the growth rings. As stiffness is lowest for the tangential direction, this would make the specimen softer than expected as seen with specimen 1. Despite these issues, the results were quite aggregated.

The failure in this configuration seemed to be quite ductile for most specimens. This seemed to be due to a gradual cracking across the width of the sill as stiffness varied significantly over the width. While the linear-elastic area was identifiable, it was somewhat S-shaped for these specimens.

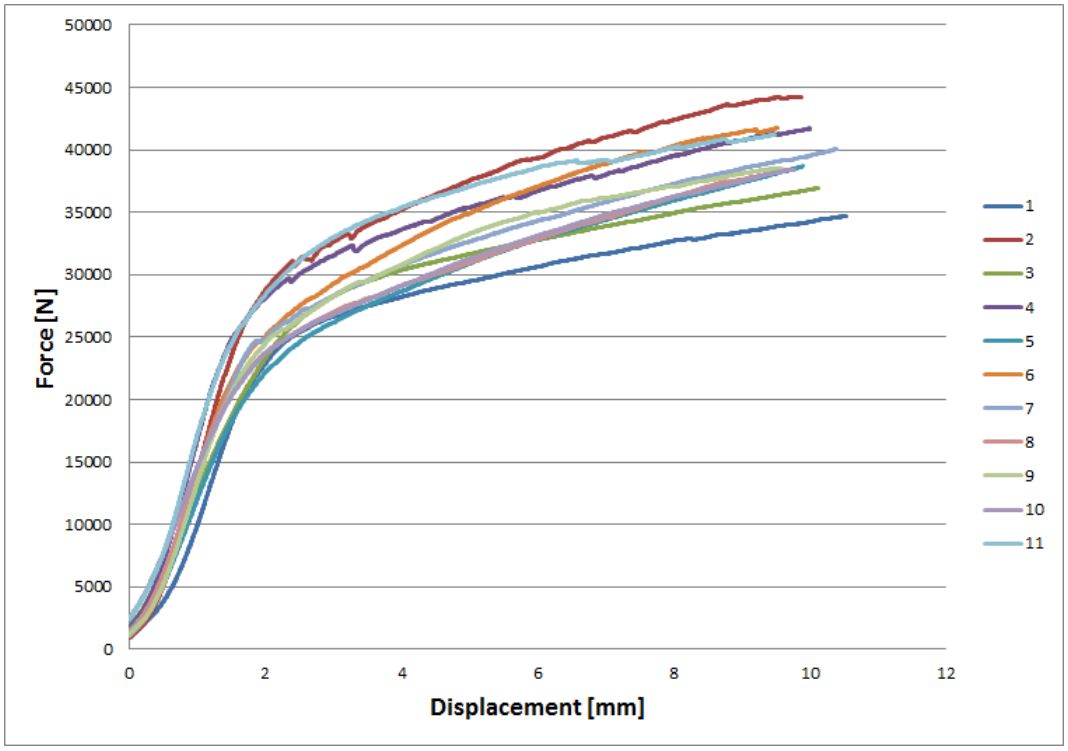

Figure 4.4: Load-displacement for case N-Pe-Lc

N-Pb-Lc

Test load-displacement diagrams are shown in figure 4.5.

This was the data used to calibrate the model; specifically specimen 7 was used for simple reference as it on inspection was a decent representation for the set. The test samples were close to the right densities and most were without significant flaws. Pith locations for this test were satisfactorily close to what was desired.

The specimens displayed very similar behavior in the linear-elastic area which was easy to make out, but had different softening and strength properties. Failure seemed a little brittle as fractures caused some sudden loses of strength.

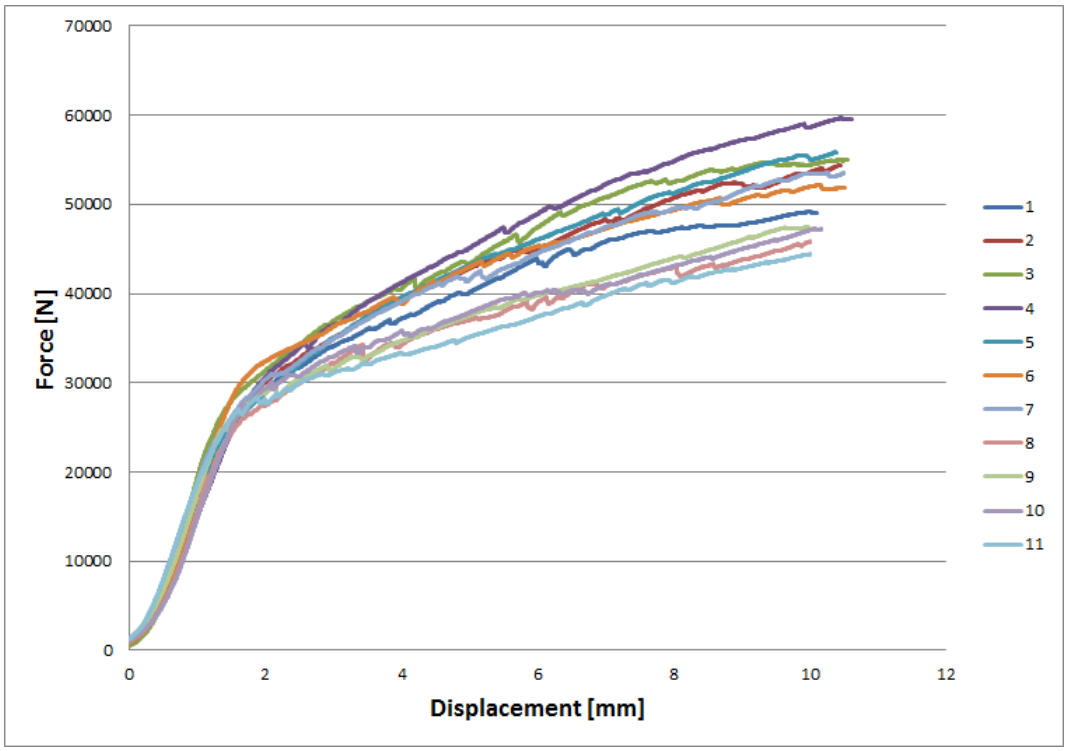

Figure 4.5: Load-displacement for case N-Pb-Lc

N-Pa-Lc

Test load-displacement diagrams are shown in figure 4.6.

In this test set, a lot of the specimens had a higher density than the average for the wood quality. Most of the specimens gave a similar response, but specimen 8 and 10 seemed to diverge from the lot. These two specimens both had vertical knots in the loaded zone, which seemed to stiffen the response considerably. Figure 4.7 is a picture of the two specimens to show the knots. As they clearly protruded from the sill, it was assumed knots with grain in the vertical direction could contribute significantly to the stiffness of the system.

Failure in this configuration seemed very ductile, and it was difficult to make out fractures in the load-displacement diagram for most of the specimens. When using this data for further calculations, specimens 8 and 10 were left out as the effect of the knots clearly did not match the condition that specimens should be nearly flawless.

The linear-elastic area for these specimens was not well defined due to the S-shape in the early response in the load-displacement diagram.

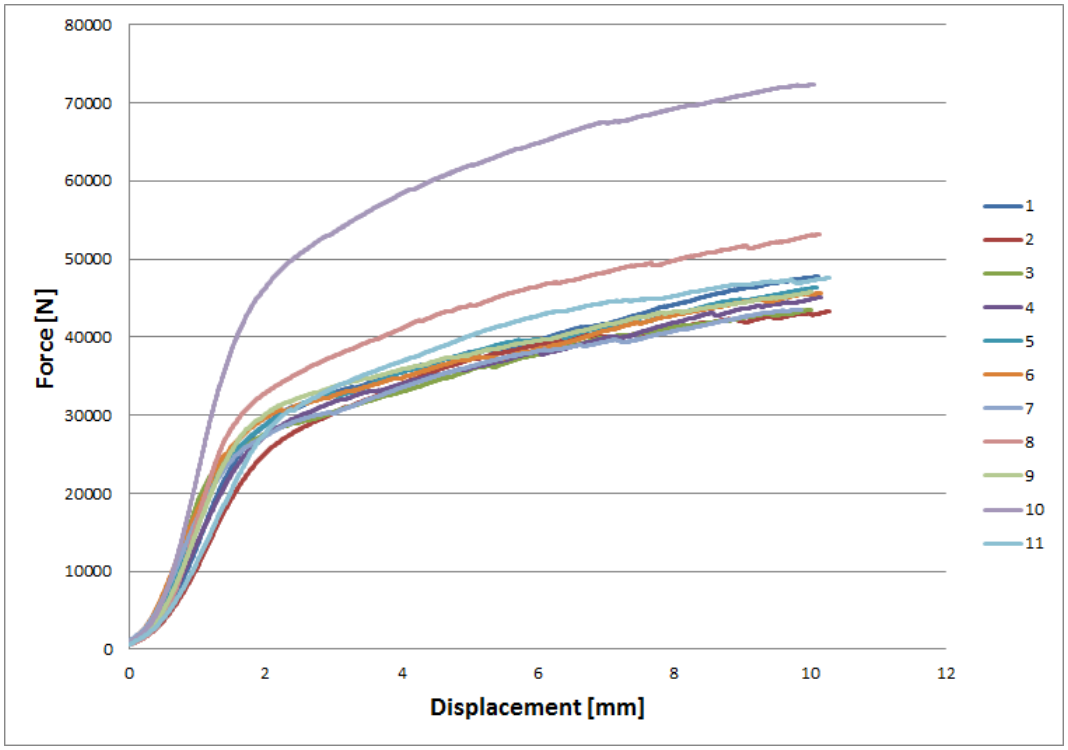

Figure 4.6: Load-displacement for case N-Pa-Lc

Figure 4.7: Knots in specimens 8 and 10

N-Pc-Lh

This test was not completed due to lack of material with the pith in the center.

N-Pc-Le

This test was not completed due to lack of material with the pith in the center.

N-Pb-Lh

Test load-displacement diagrams are shown in figure 4.8.

Densities for this test were distributed about the desired value. The responses seemed nicely aggregated and all samples displayed more rapid strength loss during cracking than the cases were the end lengths were greater. A linear-elastic area was also easy to identify for this case, as it had a less pronounced S-shape to the load displacement curve.

This test had some of the greatest losses of strength upon fracture seen in the tests, caused by horizontal cracks running from under the loaded zone to the closest free end. Some examples of these cracks are shown in figure 4.9.

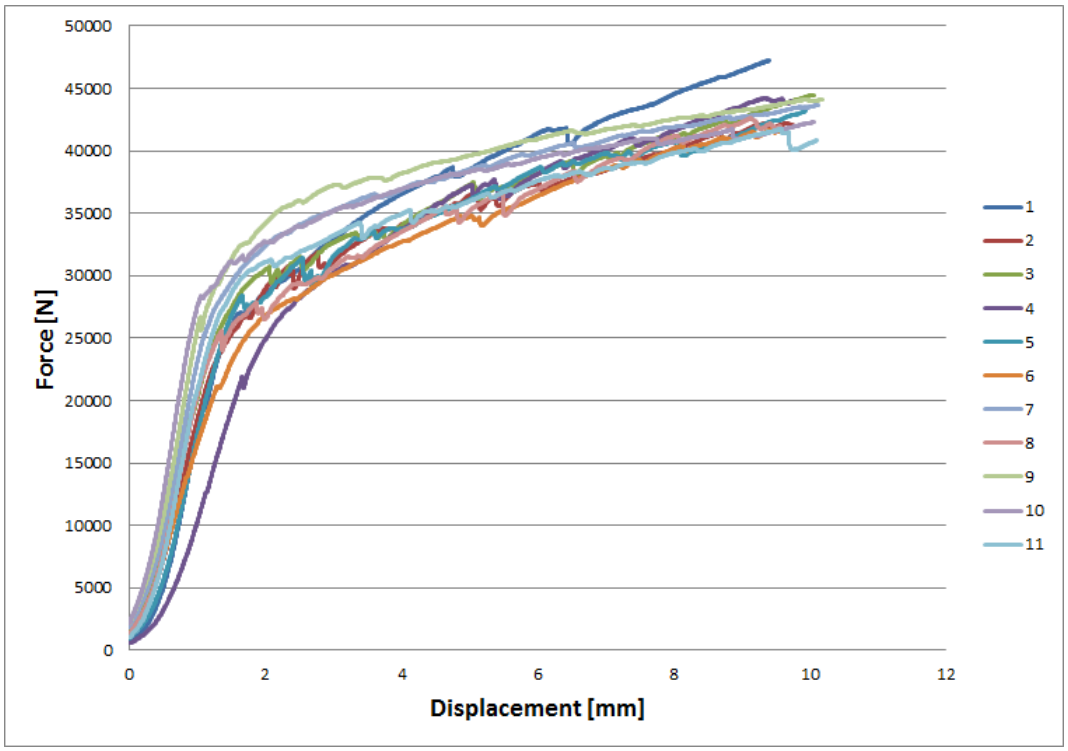

Figure 4.8: Load-displacement for case N-Pb-Lh

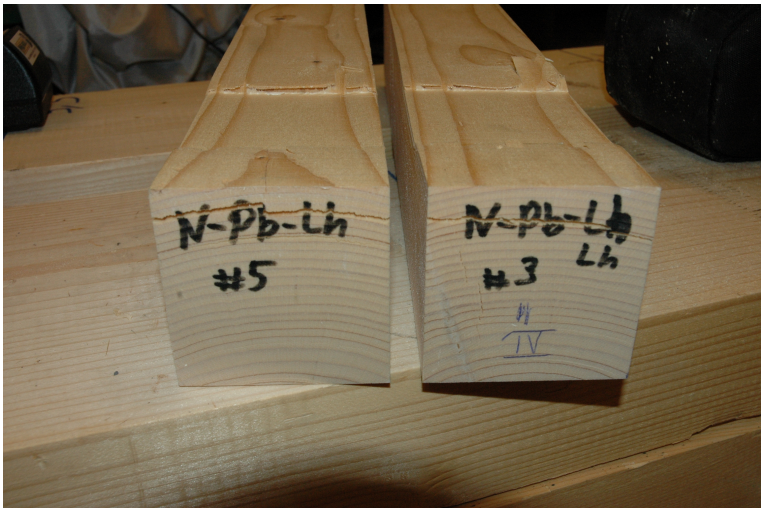

Figure 4.9: Examples of horizontal cracks reaching the edge of specimens

N-Pb-Le

Test load-displacement diagrams are shown in figure 4.10.

The specimens in this test had a lower average densitiy than the average for the wood strength class. This was expected to cause a lower stiffness and strength. Most of the samples gave a similar response, except for specimens 7 and 8. These were inspected thurougly to look for flaws that could explain the response, but no conclucive cause was found. As there was no telling if the divergence was natural variation for the configuration or the result of flawed specimens, the data from these specimens were included in further calculations as a conservative approach.

For the other specimens, there was a clear linear-elastic area and fractures seemed to be propagating fast with quite a loss in strength upon failure.

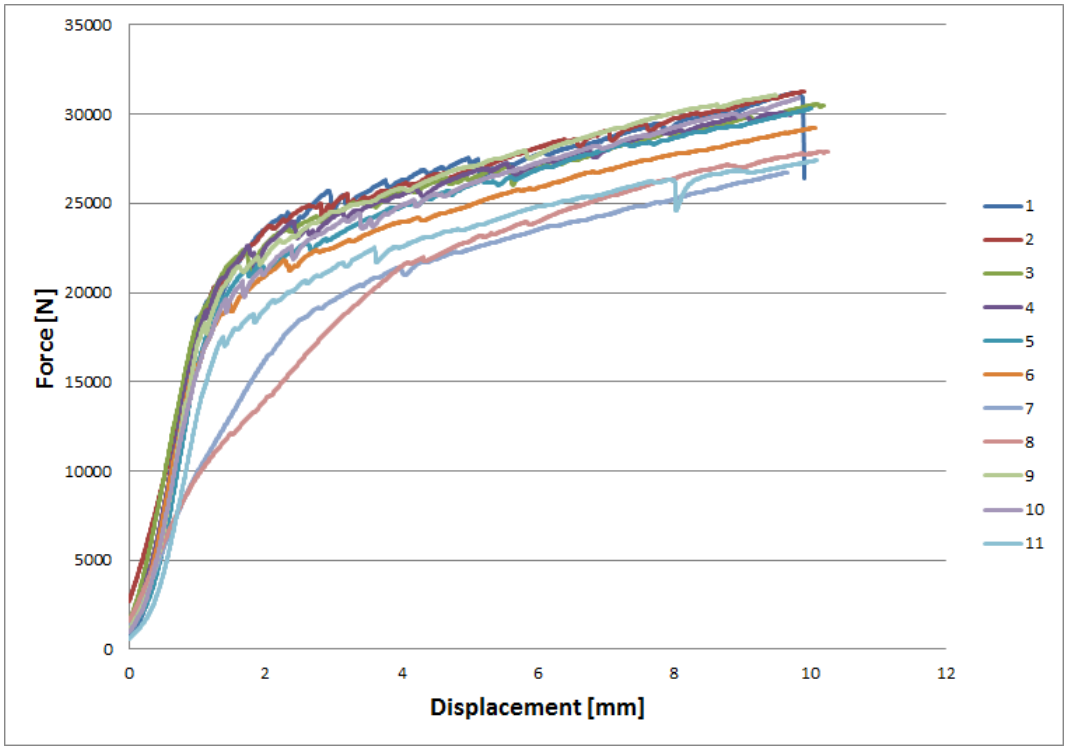

Figure 4.10: Load-displacement for case N-Pb-Le

D-Pb-Lc

Test load-displacement diagrams are shown in figure 4.11.

As the height of these specimens was twice that of the other sills, getting enough specimens with the pith below the bottom surface of the sill proved difficult. Only 8 specimens were extracted from the available material and in many of them the piths were in or near the bottom edge and few of the piths were centered.

This set of specimens had densities that ranged from above the mean for the strength class to quite far below. The load-displacement responses of the specimens in this tests were quite similar except for specimen 3 that displayed a greater than average strength. As with specimen 8 and 10 in figure 4.6, this seemed to be caused by the occurance of a vertical knot in the loaded zone. Thus the data from this test was not used for futher calculations.

For all the data, the linear-elastic area was S-shaped and fractures were propagating neither particularly fast nor slow.

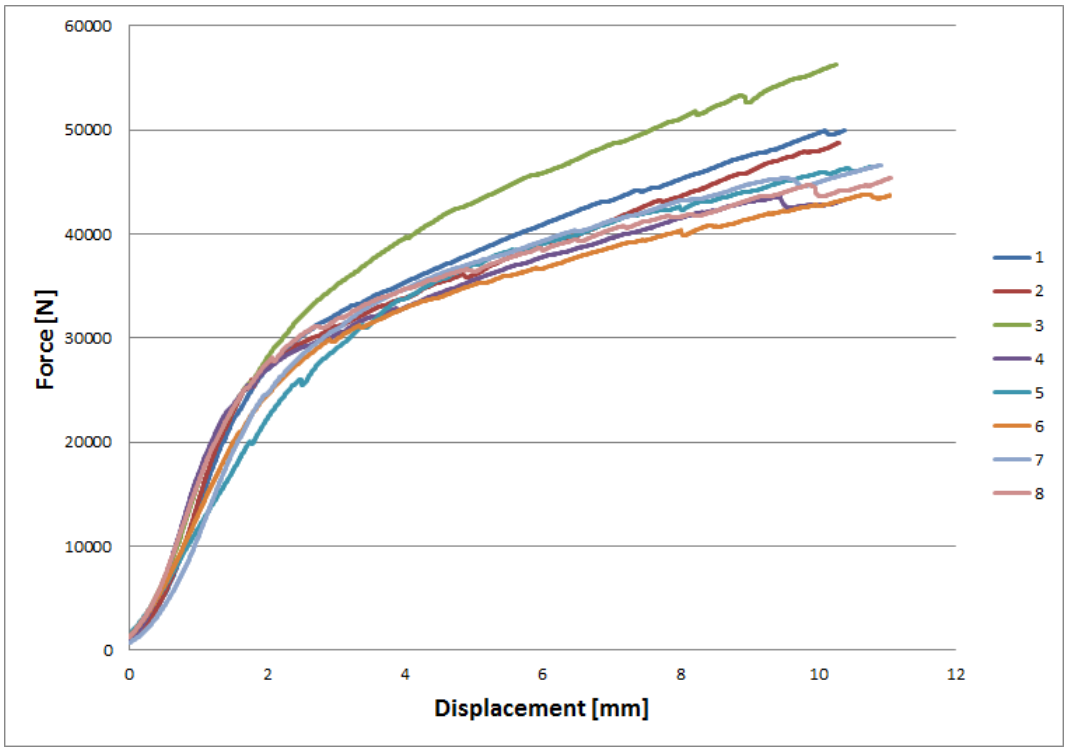

Figure 4.11: Load-displacement for case D-Pb-Lc

H-Pb-Lc

Test load-displacement diagrams are shown in figure 4.12.

Specimens in this test had a massive spread of densities that made it likely with quite divergent results. The spread of results in terms of load displacement diagrams was quite clear. All specimens were inspected and it was concluded that the spread was not caused by flaws. This conclusion was supported by cross-referencing densities with the load response diagram; high densitiy specimens were predominantly stiffer than low density specimens.

Most of the specimens had a quite clear linear-elastic response area, with a slight S-shape. Fractures seemed to be spreading fast causing great loss of strength on failure initiation.

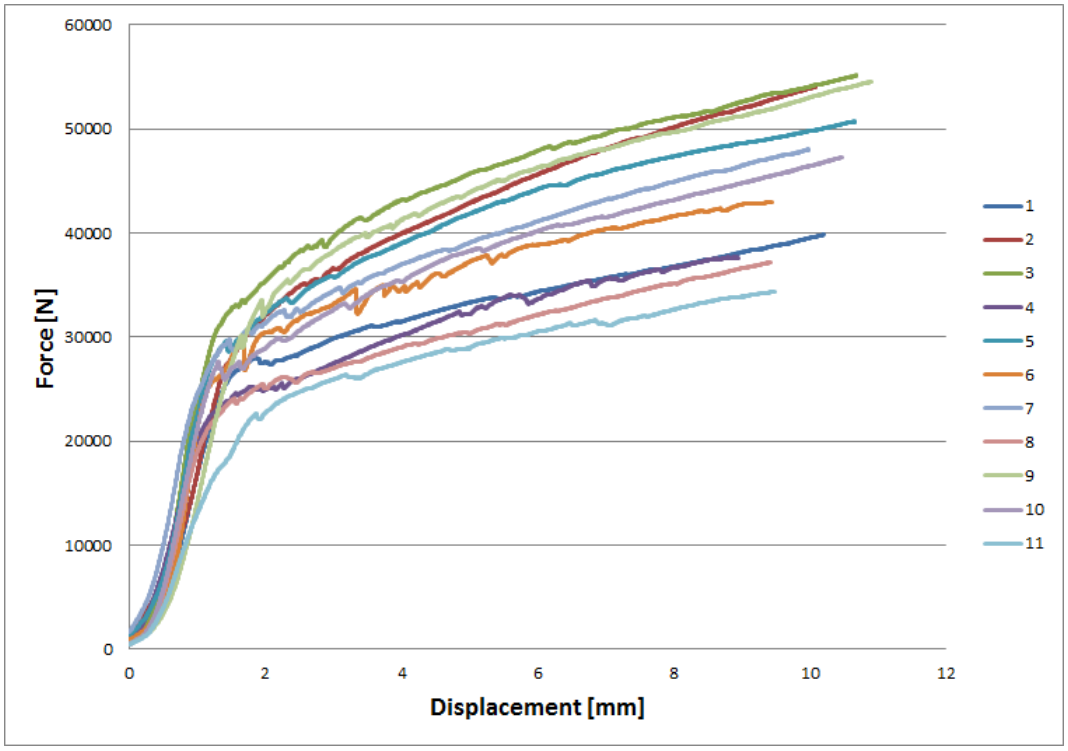

Figure 4.12: Load-displacement for case H-Pb-Lc

	Real $[kg/m^3]$		*Adjusted* $[kg/m^3]$	
Wood piece	Average	SD	Average	SD
I	411.62	±13.71	413.75	±13.70
II	439.86	±20.03	440.24	±19.26
III	432.68	±25.28	433.80	±24.36
IV	427.85	±20.60	429.23	±19.96
V	374.83	±17.73	378.18	±17.35
VI	422.48	±10.32	424.53	±10.29
VII	394.01	±12.80	396.09	±12.53

Table 4.3: Real and adjusted average densities and sample standard deviations for clear wood pieces

4.3.2 Moisture Content

Moisture content was measured in every stud and sill. Table 4.2 shows the average moisture content in the wood pieces from which the sills and studs were cut as well as the sample standard deviations for this data. Individual measurements, as well as listing of which sills and studs were cut from which piece, can be found in Appendix D.

For most of the pieces, there seemed to be a moisture content slightly below the 12% assumed in the Eurocode [2]. Theoretically, this should give a stiffer response. This effect could be more applicable than table 4.2 implies as the apparatus used to measure the moisture content might have overestimated the moisture content as described in section 4.1.1.

Wood piece	Average	SD
I	10.96%	±0.36%
II	11.81%	±0.51%
III	11.46%	±0.49%
IV	11.34%	±0.42%
V	10.19%	±0.52%
VI	11.03%	±0.26%
VII	10.94%	±0.27%

Table 4.2: Average moisture content and sample standard deviation for clear wood pieces

4.3.3 Densities

Density was measured in every stud and sill. Table 4.3 shows the average density of the wood pieces from which the sills and studs were cut as well as the sample standard deviations for this data. Table 4.4 shown the average density of the wood specimens used in each test as well as the sample standard deviations for this data. Individual measurements, as well as listing of which sills and studs were cut from which piece, can be found in Appendix D.

Some of the densities were quite far from the prescribed value of $420\,kg/m^3$, the most pronounced being piece V with a very low density. These deviations caused differences in stiffness and strength that had to be taken into account.

	$Adjusted\,[kg/m^3]$	
Test	Average	SD
N-Pc-Lc	$392,89$	$\pm 5,19$
N-Pe-Lc	$404,49$	$\pm 18,87$
N-Pb-Lc	$420,38$	$\pm 8,01$
N-Pa-Lc	$445,59$	$\pm 14,15$
N-Pb-Lh	$416,49$	$\pm 18,41$
N-Pb-Le	$376,80$	$\pm 13,13$
D-Pb-Lc	$409,29$	$\pm 20,83$
H-Pb-Lc	$406,38$	$\pm 30,87$

Table 4.4: Adjusted average densities and sample standard deviations for test specimen sets

Chapter 5

Calibration

As the model from chapter 3 was based on some assumptions and approximations, it was considered critical to compare the reference case with research data before altering parameters and comparing with laboratory data from more complex cases. This was done as an evolution of the prototype model, testing and changing it as results came in.

5.1 Testing Material Model in Parts 1 and 2

In subsection 3.2.1 and section 3.5, a problem that arose during the initial model creation was presented. Specifically, it was uncertain what material model would be best suited for what was named as parts 1 and 2. As testing this required the rest of the model to be virtually complete, the testing of these models was done as a part of the calibration. All three strategies from subsection 3.2.1 were tested in analysis, as well as the modification to the first strategy proposed in section 3.5. Results in the form of load-displacement diagrams from these tests are shown in figure 5.1. Note that some of the analyses aborted before others, usually when the first crack opened. Rather than using time getting all of the options to converge, the analyses seemed to give enough data to discard at least a few of the options. Time used to get the analysis to converge for longer could thus be used on the models that actually worked. Research data from Hardeng [12] was used to evaluate the models adherence to real load-displacement response and crack growth.

Please note that loads are for the half model and that the pith was in the center of the sill for this series of tests.

5.1.1 XFEM

Using full XFEM, which meant having XFEM active with a MAXE damage criteria for all parts, seemed to cause very little softening prior to fracture. It also gave a very unstable crack growth that is shown in figure 5.2. Looking through the steps as the crack propagates, it was clear that the crack started in parts 1 and 2. It then propagated into the other parts, causing cracks in the longitudinal direction that blocked any vertical crack initiation as cracks cannot split or grow into each other. This strategy was unsuitable to model the problem and was discarded.

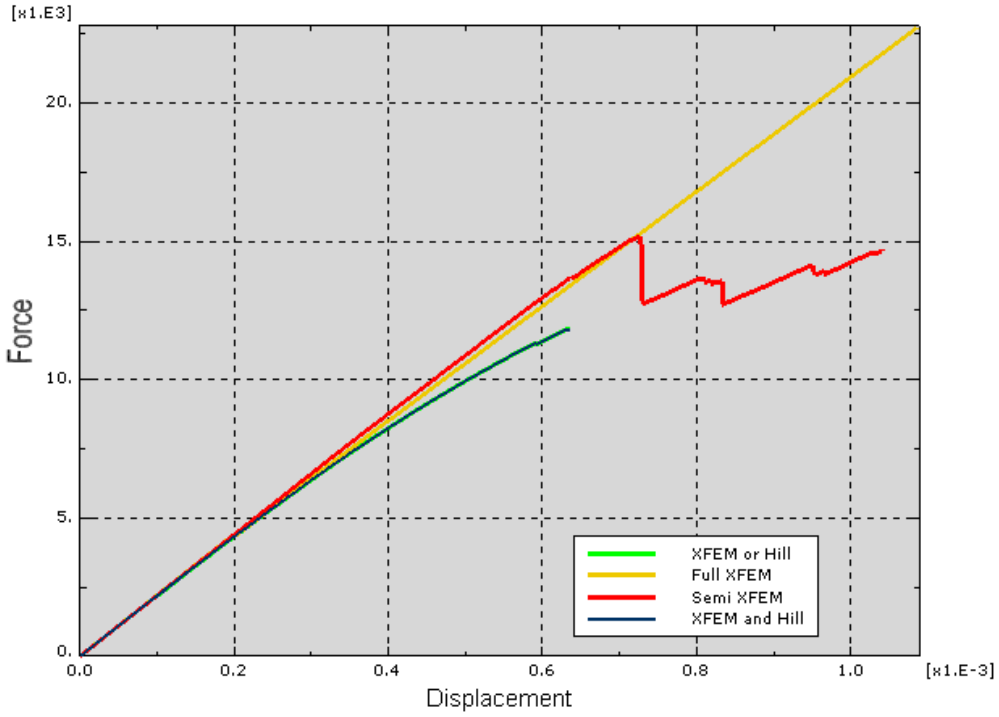

Figure 5.1: Load displacement diagrams for the strategies tested, force is in Pa and Displacement in m

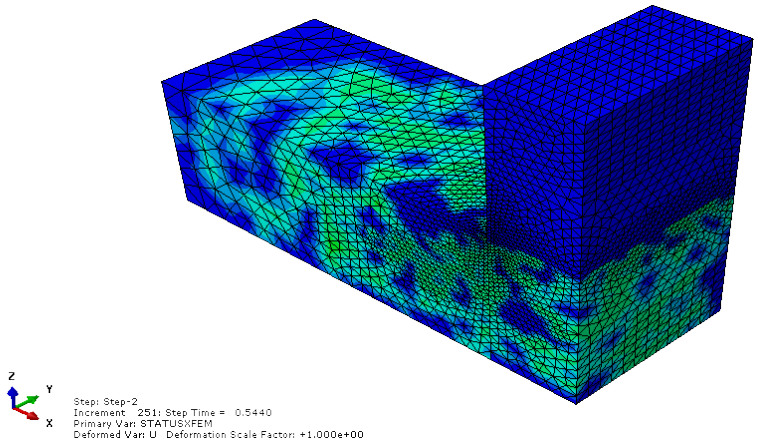

Figure 5.2: Unstable crack growth in the sill for full XFEM

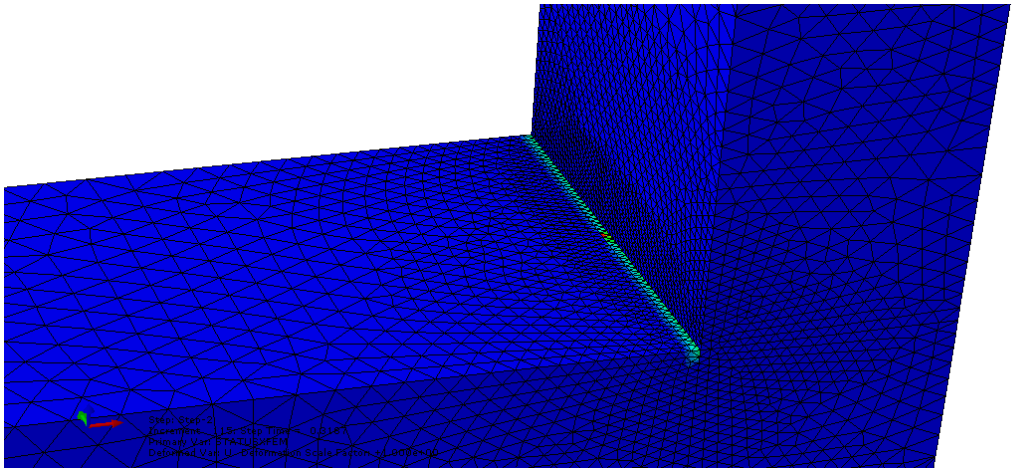

Figure 5.3: Damage and crack initiation with Hill anisotropic yield in parts 1 and 2

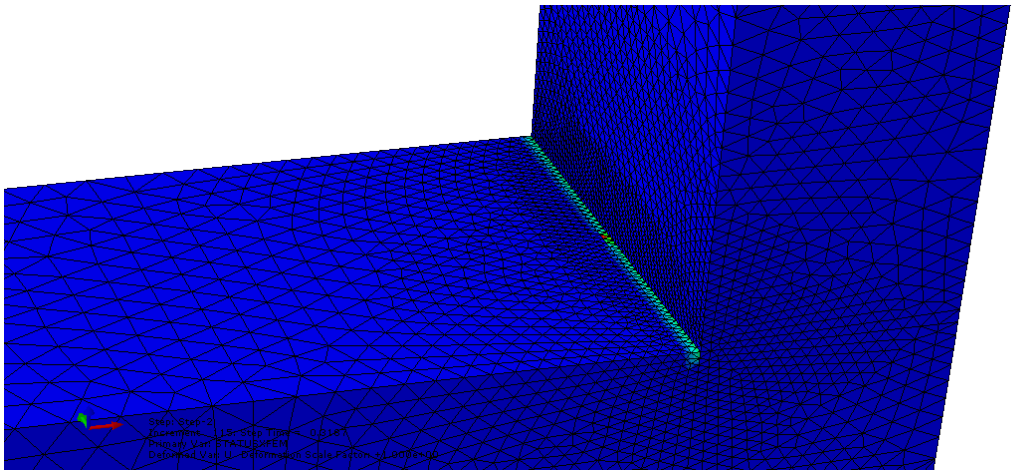

Figure 5.4: Damage and crack initiation with XFEM and Hill anisotropic yield in parts 1 and 2

5.1.2 Hill Anisotropic Yield

This strategy used XFEM with MAXE damage for parts 3, 4 and 5, while parts 1 and 2 were modeled with plastic yielding using Hills potential function. From figure 5.1 it was clear that there was softening of the response as deformations grew. While the analysis aborted on crack initiation, figure 5.3 shows that the crack was initiated in the expected spot and that damage indicates the fracture will spread over the width of the sill if convergence was worked on.

5.1.3 XFEM and Hill Anisotropic Yield

Combining the two strategies meant modeling parts 3, 4 and 5 with XFEM with MAXE damage, while parts 1 and 2 had both XFEM with MAXE damage and Hill anisotropic yield with softening. The results were close to exactly the same as those presented in 5.1.2, indicating that the Hill anisotropic yield simply overrides the MAXE damage criterion, meaning that this model was redundant and it was discarded.

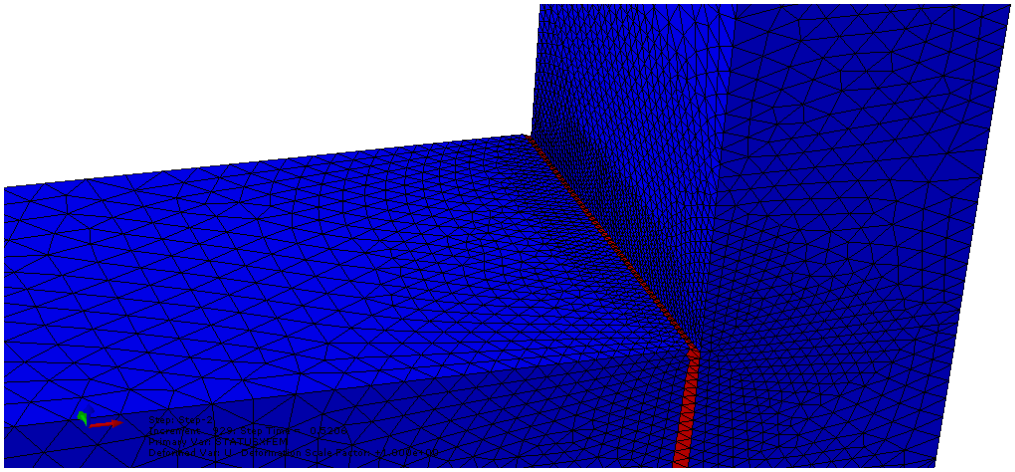

Figure 5.5: Damage and crack initiation with MAXE damage but no XFEM in parts 1 and 2

5.1.4 XFEM Deactivated (Semi XFEM)

This strategy simply ment deactivation of XFEM for parts 1 and 2, while leaving the same material models as with the full XFEM approach. Crack growth went furthest in this approach and there was very little softening before fracture. It was obvious that the crack had propagated too far in the material for the prescribed displacement. The model served as a guideline with regards to convergence for crack initiation and growth, but was otherwise discarded.

5.2 Calibrating the Reference Case

Having eliminated three of the four proposed strategies for modeling parts 1 and 2, only one model remained: The model with Hill anisotropic yield in parts 1 and 2, using XFEM with MAXE damage in parts 3, 4 and 5.

Not every parameter should be changed during calibration. After all, the model would have to work with data from the literature to be useful. Therefore only areas where assumptions and approximations were used during modeling were changed in model calibration. This meant that changes would mainly be related to the Hill anisotropic yield, fracture criterion and fracture energy.

As samples from the tests with the pith below the sill became available first, the model was adapted to this case. The test setup used as the reference case is denoted N-Pb-Lc.

5.2.1 Initial Changes

The model suffered from convergence issues upon crack initiation. As was clear from the load-displacement diagram in figure 5.1, a displacement of 1mm was more than the model could handle. Halving the displacement per unit of step time has the same effect as halving the increment sizes with respect to displacement increments. To avoid unnecessarily small increments, the initial and max increments were set to 0.1 while minimum increment was left at 1×10^{-30}.

During convergence test runs, it became apparent that the analysis was having problems with undefined Hill potential. A simple modification seemed to fix this problem: As

the R ratios were causing negative factors in the Hill potential, the R ratios were changed so that $R_{22} = R_{33} = 0.251$.

It was also discovered that partitioning the deformation in two steps had caused an error leading to unloading during the first part of step 2. As the initial increment size for step two was already changed to the same as for step one, the two steps were remerged to remedy this problem.

5.2.2 Increasing Displacement

After the quick fixes proposed in subsection 5.2.1, the model was better able to run beyond first fracture. While it modeled the ductile failure of the material in compression and found a point of fracture, it was desirable to get the model to show crack propagation and post fracture material behavior.

As convergence improved slightly due to the initial changes, the step time was changed to 10 and the total displacement was optimistically increased to 10mm. This maintained the displacement increments despite increasing the total displacement over the analysis. While the initial model had problems getting past 1mm displacement, it was hoped that calibration could get the model to run past 2mm displacement. The full displacement was never reached, usually the analysis diverged and aborted or was terminated when it was clear the solution was diverging.

5.2.3 Comparing Initial Model with Laboratory Tests

Test data from test set N-Pb-Lc specimen 7 was used as a basis for comparison. It seemed to be a decent representation of the test set average and it was believed that using only one graph made it easier to pick out the similarities and differences. While a trend line for the entire set could be used, it would eliminate or soften variance caused by cracks making initial cracking hard to identify. The plot in figure 5.6 shows the load-displacement for specimen 7 and for the uncalibrated model. As explained in section 4.3, the responses in the laboratory tests were probably too soft because of uneven load distribution. This would separate it from the idealized numerical model.

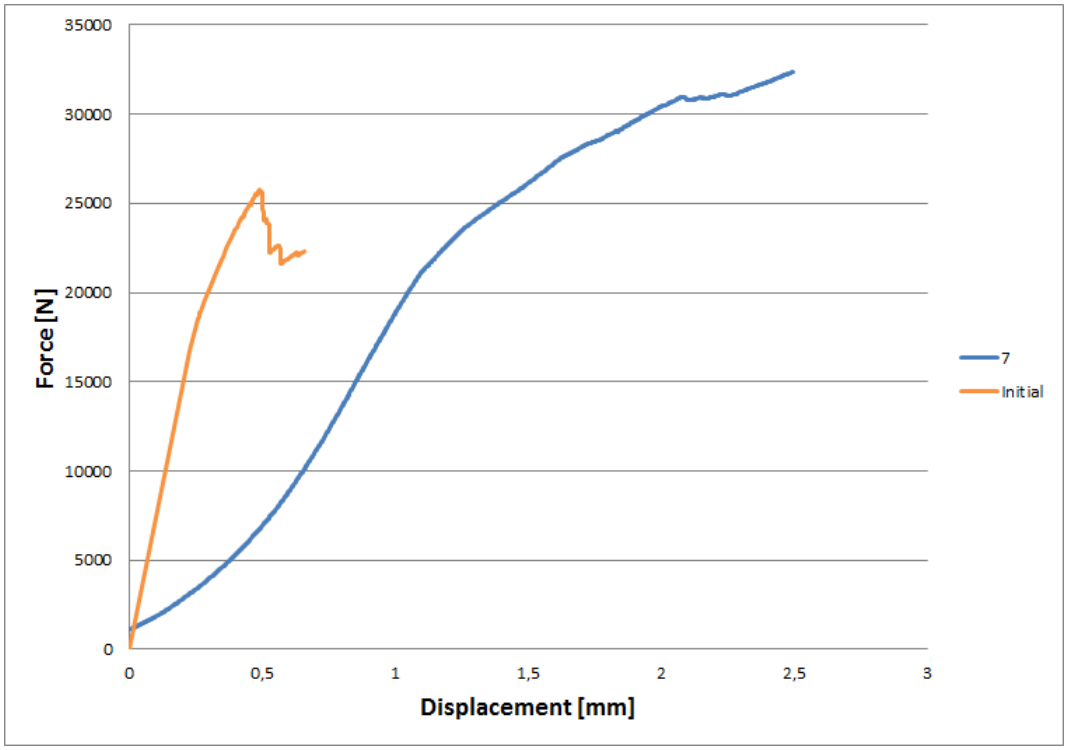

Figure 5.6: Load-displacement for specimen 7 and inital model

A few observations were made:

- The model was too stiff initially, even when taking into consideration that the response from the laboratory tests might be a little too soft.
- First fracture happened at an appropriate load.
- First fracture caused a great loss of strength.
- Softening seemed decent, but it was hard to tell as the linear elastic areas do not match up well.

5.2.4 Calibration

Several calibration runs were completed in an attempt to address the problems with the model. The goal was to get realistic softening and crack growth. Changes were made to the material model gradually. An issue with the calibration was analysis time, as a single analysis took about 6 hours to produce interesting data and in excess of 24 hours to complete a deformations above 1mm. This made making adjustments very time consuming.

Linear Response

From the initial observations it was clear that the linear response was far too stiff. In the literature, it is sometimes assumed that $E_{RR} = E_{TT}$ [27]. Implementing this in the model meant that $E_{RR} = E_{TT} = 420MPa$ and $\nu_{TR} = 0.6$. This change made the linear response a little better, but also meant that the model would not give as much difference in results when varying pith location. It was uncertain if the model could be made to give

σ	ϵ_p
10	0.00000
14	0.00308
16	0.01015
64	0.015

Table 5.1: Hill potential σ and ϵ_p data pairs for first calibration. Stresses in MPa

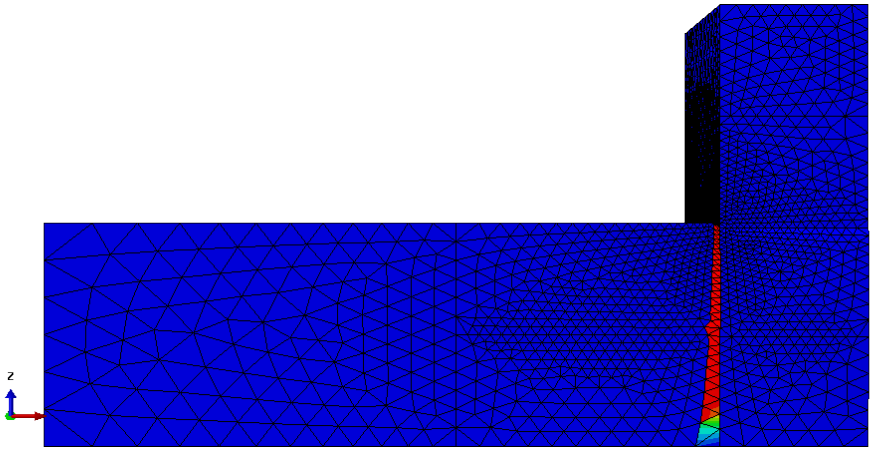

Figure 5.7: Crack propagation in a model prototype

the linear elastic response seen in the real case by altering stiffness moduli within realistic parameters.

Softening

The data for Hill potential was changed according to table 5.1. This was an attempt at getting correct softening, as the extreme displacement value for $64MPa$ caused convergence problems. It was clear that using Hill would make realistic softening difficult; however, no other options were available. The changes improved the convergence of the model significantly and gave better softening.

Crack Propagation

Cracks were propagating too fast through the material, causing great loss of strength as seen in the load-displacement diagram in figure 5.7. It was believed this was due to the partitioning of the sill material properties and limitations in the XFEM formulation. In real case, seen in figure 5.8, horizontal "yield lines" have appeared in the area below and around the loaded zone and cracks have propagated horizontally.

Clearly, the ductile failure was spreading horizontally beyond the block of the sill identified as parts 1 and 2 in the model. As the model did not allow yielding other than in part 1 and 2, a strength difference occurred in the interface between parts 1 and 2 and parts 3 and 4, as yielding was initiated. Naturally, such a difference caused greater shear stresses and strains than was realistic. This was likely a contributing cause of the quick crack propagation in the model as well as the post fracture strength being too low. A cure was attempted; simply to implement Hill yielding in the material model for parts 3 and 4. These tests did not converge.

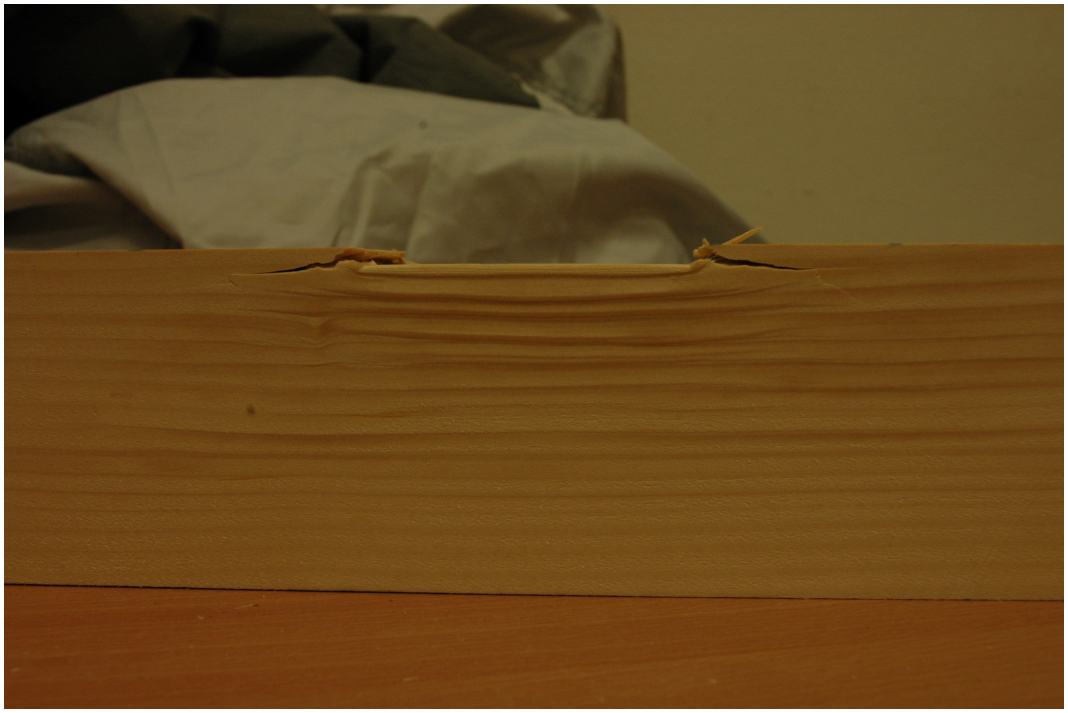

Figure 5.8: Side view of a sill after being compressed in the lab tests

More tests were run in attempts to improve crack propagation, but the limitations in the program and of having to use actual values from literature meant there were not a lot of options available.

Finally, in an attempt to make mode I cracks more dominant, the failure shear strains and fracture energies were doubled for the models with $E_{RR} = E_{TT}$. This clearly made the model diverge from reality, but was attempted none the less to get better post-fracture behavior.

The load-displacement responses of a few calibration iterations of the model, including both versions of linear elastic properties proposed before, are shown in figure 5.9 compared to specimen 6, 7 and 11. Models with $E_{RR} = E_{TT}$ are better in terms of stiffness, but are far off in terms of failure load.

It was clear at this point that the model could not be calibrated to match the cases very accurately, there simply seemed to be too many nonlinear effects that could not be modeled adequately by the software. For finding load at first failure, the initial material model was used as it had properties matching those found in the litterature. Calibration 11, while having a too high fracture load, had some interesting properties: Like all the others, it was too stiff and cracks destabilized but it featured softening properties and hardening after first fracture similar to that seen in the laboratory results.

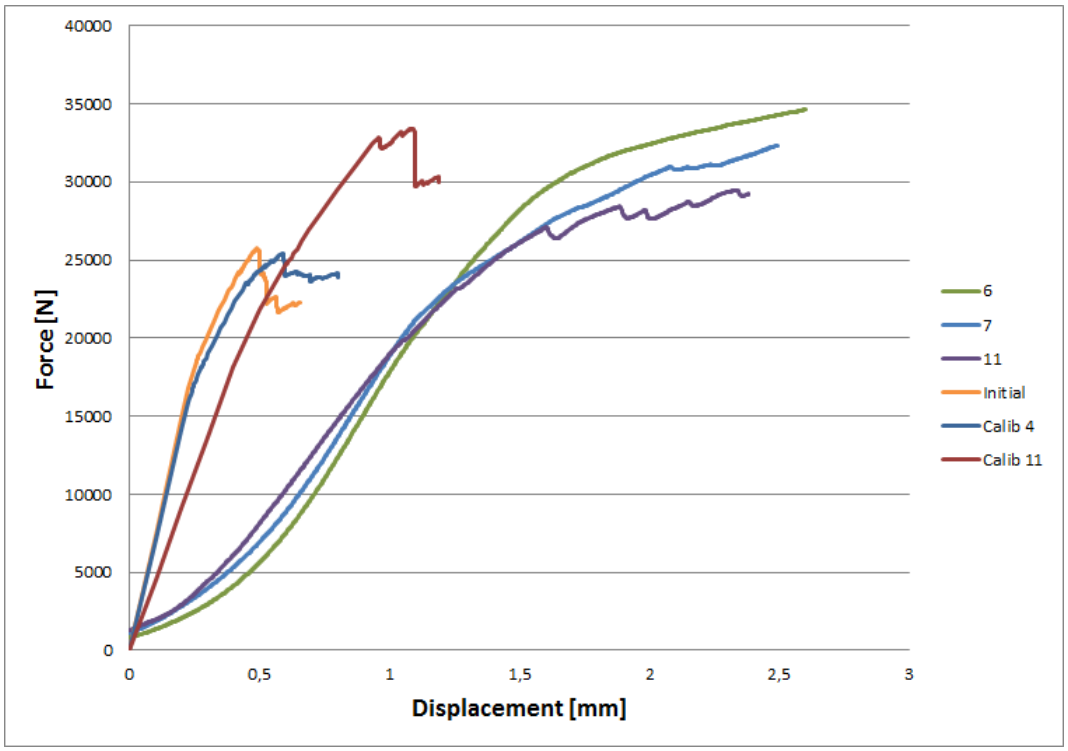

Figure 5.9: Load-displacement for specimens 6, 7, 11 and calibration 4, 10, 11

Chapter 6

Discussion

This chapter will be focused on the comparison of the different cases and its numerical model equivalent created using parameters from the calibrated model as a base; parameters and geometry was altered to see if the general setup of interactions and material properties would be valid, ergo producing similar data as the laboratory results, with new parameters.

Comparisons with results for the cases calculated using the Eurocode, full calculations in appendix B, are also discussed before evaluating strength and utility of the model as a whole.

Finally, the impact of different parameters in light of results attained through numerical simulations and laboratory work is assessed.

6.1 Evaluation of Load-displacement Response Data From the Model

The focus of this section is on the comparison of the real load-displacement diagrams and those produced by the model. Even though it was clear that the model would not be able to accurately model the load-displacement response of the cases, it was considered interesting to see how the model would adapt when changing parameters. It was also of some interest to evaluate convergence or divergence of each case run with the model.

Both the initial iteration of the model and the one named Calib 11, henceforth simply referred to at the calibrated model, were adapted to all cases. As the modeling of post fracture behavior was unsatisfactory, the analyses were run for a maximum of 24 hours before being terminated. Some of the analyses diverged and aborted within this timeframe.

In all cases, no effort was made at improving convergence at this point, as the solution never diverged before first fracture. Thus data from the elastic response, damaged response and the load at first fracture could be extracted from all the models.

The complete set of load-displacement diagrams, comparing model response to the floating average of all the specimens in each laboratory test, can be found in appendix C.

6.1.1 N-Pc-Lc

Load-displacement diagram in figure C.1 of appendix C.

Both the tested material models gave a too great stiffness in the elastic area. Softening and fracture seemed to happened at about the right load with the initial model, while

the calibrated one overestimated damage initiation and fracture loads significantly. Post fracture behavior was unstable in both models and strength was progressively deteriorating.

6.1.2 N-Pe-Lc

Load-displacement diagram in figure C.2 of appendix C.

The case where the pith was placed at a sill bottom corner caused more shear, specifically in the RT-plane. This is the softest shear plane in deformation. From the load-displacement diagram, it was clear that the model gave a too stiff response. Softening and damage happened at appropriate loads for the initial model, while the calibrated model overestimated again. Crack propagation in the initial model was too fast, resulting in a great loss of strength after first failure. As the calibrated model diverged during the first crack growth, it was unclear how the crack growth would continue.

6.1.3 N-Pb-Lc

Load-displacement diagram in figure C.3 of appendix C.

The reference case has its pith placed somewhere below the centerline of the sill. Model response for this case was discussed in section 5.2; it was too stiff and lost too much strength as a consequence of fracture. First failure seemed to happen at a reasonable load for the initial model, while the calibrated model overestimated by a bit. The rapid growth of the crack was clearly not a good representation of post fracture behavior.

6.1.4 N-Pa-Lc

Load-displacement diagram in figure C.4 of appendix C.

For this case, the problems were much the same as in the previous cases. The model gave a too stiff response, the initial model gave seemingly good results for softening and first fracture while the calibrated model overestimates. Both the models gave extremely fast-growing cracks, with cracks propagating very far in the material after first failure.

6.1.5 N-Pb-Lh

Load-displacement diagram in figure C.5 of appendix C.

While still giving a too stiff response, this case provided one of the better matches in the linear-elastic area. Unlike previous cases, the calibrated model seemed to give a reasonable estimate for first failure while the initial model underestimated. As none of the two models converged beyond crack initiation, it was not possible to evaluate post fracture behavior.

6.1.6 N-Pb-Le

Load-displacement diagram in figure C.6 of appendix C.

Same as all the cases, the model gave a too stiff response in the linear-elastic area. Softening seemed to start at about the right load for the calibrated model, while it overestimated the load at first fracture. The initial model seemed to underestimate both softening and failure load. Both model analyses diverged at the initiation of the first crack, making evaluation of the post failure area impossible.

6.1.7 D-Pb-Lc

Load-displacement diagram in figure C.7 of appendix C.

Model response for this case was way too stiff and softening was, while starting at an appropriate load with the calibrated model, nearly indistinguishable from the linear-elastic area. The calibrated model seems to give a reasonable estimate for load at first fracture, while the initial model underestimated again. In this case, both model analyses diverged at crack initiation, again making evaluation of post failure behavior impossible.

6.1.8 H-Pb-Lc

Load-displacement diagram in figure C.8 of appendix C.

For the final case gave, like all the other cases, a too stiff response resulted from the model. Softening seemed to start too early for the initial model and at a more reasonable load for the calibrated model. The initial model seemed to give a reasonable estimate for load at first failure while the calibrated model overestimated. Finally, the inital model gave some reasonably stable crack growth but still lost too much strength after failure. The calibrated model still had unstable crack growth.

6.2 Model Robustness Evaluation

Using the short evaluations in section 6.1 as well as other data extracted from models and laboratory tests, this section evaluates the strengths and weaknesses of the model.

6.2.1 Pre-Fracture Behavior and Strength

The load at first fracture was extracted from both models for all the cases. In table 6.1, these strengths are compared to ULS loads calculated using the Eurocode with characteristic values, full calculations in Appendix B, and failure loads from the laboratory tests. Failure loads from the laboratory tests were extracted by inspecting the load-displacement diagrams and the relative difference in force between two displacement steps. Since the tests were run using displacement control, initial failure was hard to make out for some of the specimens that had seemingly ductile behavior. In these cases, plateaus where load increase was close to zero for several displacement steps were selected as failure load. This was clearly the source of some error.

Stiffness of the numerical model is also evaluated in this subsection as it is related to the strength through fracture strains and both the strength and stiffness of wood is linked to the density of the wood. Table 4.4 was referenced for densities when evaluating the data.

Stiffness Properties

From the individual evaluations in section 6.1, it was clear that the model was stiffer than the laboratory tests in all the cases. There are several possible factors that can have caused this error.

First, as explained in subsection 2.3.2, the model had to use linear elements. This is known to cause models that are too stiff if the mesh is not sufficiently fine. Meshing convergence tests in section 3.4 showed that the global stiffness of the model went down as the mesh was made finer. However, as was pointed out in this section, the analysis time

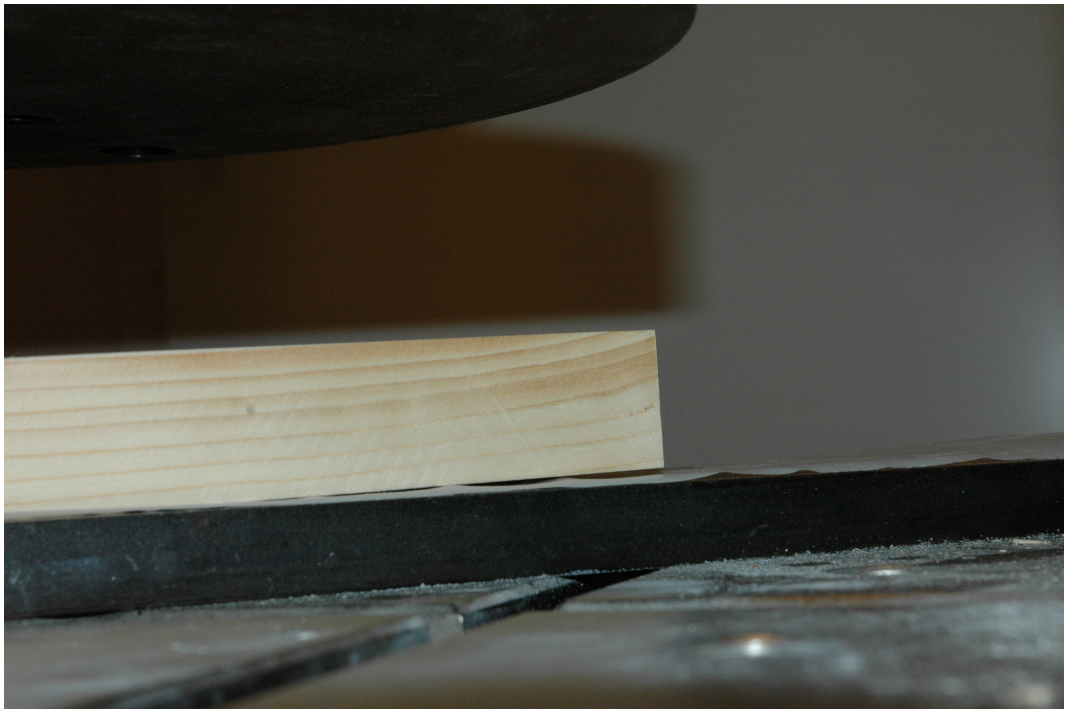

Figure 6.1: Lifting of the ends of a H-Pb-Lc sill

increases substantially with smaller elements. As the hardware available already used a lot of time running an analysis, a finer mesh was never implemented.

Second, the boundary conditions in the model were too rigid. As seen clearly in figure 6.1, the ends of the sills lifted during the compression tests. The boundary conditions of the model did not allow this to happen, causing an increase in stiffness. Friction tests in section 3.3 used a contact problem with an infinitely rigid surface instead of boundary conditions. Implementing this solution could have fixed the problem, but this also increases analysis time. As time did not allow for it, the solution was never implemented.

Finally, as explained in section 4.3, the load-displacement response recorded in the laboratory tests might have been too soft due to geometric imperfections causing uneven stress distribution across the loaded surface during initial loading. With the prescribed setup there was no way around this, so it was simply taken into account.

Softening

The softening used to model the ductile failure resulting from the pressure perpendicular to the grain was one of the parts of the model that seemed to be working rather well. However, the formulation was not without fault. As was discussed several times in chapter 5, the softening only happens in what was called parts 1 and 2. Inspecting the real cases, such as in figure 5.8, clearly show "yielding lines" in a wider area. In subsection 5.2.4, attempts were made at introducing Hill potential in parts 3 and 4, but the resulting softening response was barely distinguishable from the model without Hill potential in parts 3 and 4 and the solution had convergence difficulties. The attempt was therefore abandoned.

However, as explained in subsection 5.2.4, the interface between the parts that softened and those that did not can be the cause of some issues. Figure 6.2 clearly shows the discontinuity in the strain field caused by the difference in properties. While the

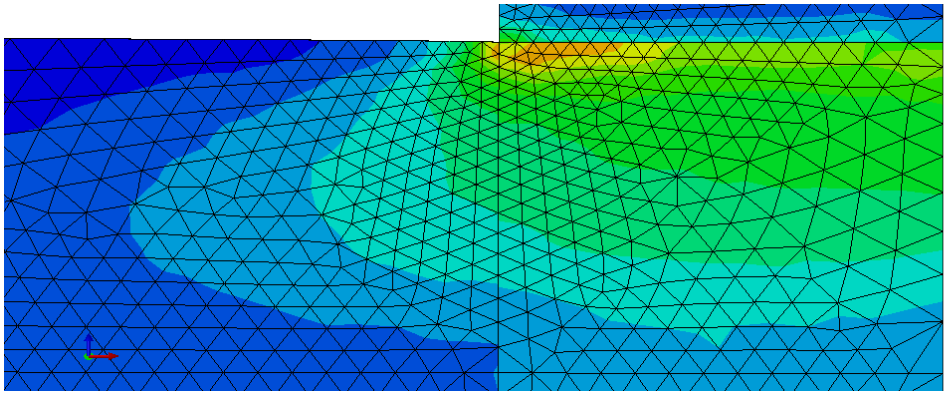

Figure 6.2: Strain on the side of the sill before crack initiation

Case	Eurocode	Laboratory Tests		Initial	Calib 11
	Force [N]	Force [N]	SD	Force [N]	Force [N]
N-Pc-Lc	25126	24740, 93	3046, 31	24289, 20	35662, 20
N-Pe-Lc	25126	25434, 65	2725, 54	23294, 00	33201, 40
N-Pb-Lc	25126	25588, 39	3365, 78	24269, 00	33199, 00
N-Pa-Lc	25126	25834, 63	1499, 81	27098, 20	40088, 80
N-Pb-Lh	25126	24379, 06	3440, 39	19162, 30	28927, 20
N-Pb-Le	19415	17941, 75	2632, 96	13267, 30	21382, 55
D-Pb-Lc	25126	24084, 34	2553, 69	20122, 60	23797, 80
H-Pb-Lc	25126	25598, 89	3313, 79	27117, 60	37252, 60

Table 6.1: Eurocode ULS loads and loads at first failure from laboratory tests and numerical simulations

effect on the load-displacement response seemed negligible, the discontinuity might have contributed to errors in fracture initiation and growth, as the crack appears in the area of the discontinuity.

Case Strength Evaluations

N-Pc-Lc This test had lower density than the mean and a slightly lower strength was therefore expected. As the test only had two specimens, the laboratory test was not in any way conclusive. For the data collected the initial model gave the closest result. Clearly, the calibrated model was far off while the Eurocode gave a reasonable value, though being a slight overestimation.

The sample standard deviation for the strength was close to meaningless because the sample size was two.

N-Pe-Lc On average this test had a lower density than the mean and a sample standard deviation signifying significant difference between the specimens. Of the two models, the initial one obviously gave the best results with the calibrated one being far off. The Eurocode accually gave the best estimate.

Compared to the other tests, the sample standard deviation for the failure load was surprisingly small considering the sample standard deviation of the densities.

N-Pb-Lc The mean density of the specimens in this test were very close to the value prescribed in the Eurocode, and the sample standard deviation for the density data was rather small. Again, the strength from the initial model was clearly the closest one and the calibrated model was far off. The Eurocode results, being slightly below the average of the laboratory tests, were good.

For having such a low sample standard deviation for the density data, the sample standard deviation for the strength data from the laboratory tests was surprisingly high.

N-Pa-Lc For this test, the mean density of the specimens tested was far above the desired value for the strength class, with a rather high sample standard deviation for the data. It was expected that the results would be greater strength. As two of the specimens had knots in the loaded zone, only nine specimens were used for the calcualtion of the strength data. The initial model overestimated the strength in this case and the calibrated model was far off again. The Eurocode clearly gave the best estimate.

Even though there was a quite high sample standard deviation for the density data, the sample standard deviation for the strength data was very low.

N-Pb-Lh Specimens used in this test had a sligtly lower than average density for the strength class. The sample standard deviation for this data was quite high. Neither model gave a good result for this setup, with the initial model underestimating strength by nearly the same amount as the calibrated model overestimates strength. The Eurocode, while overestimating, gives a decent approximation.

As was expected with quite a variation of densities for the specimens in the test, the sample standard deviation for the strength data was high.

N-Pb-Le This test had specimens with very low densities compared to the mean for the strength class. With a sample standard deviation for the data that was neither high nor low, it was expected that the entire set would give similar and low values for strength. Even so, the initial model underestimated the strength found in the laboratory tests by quite a lot while both the Eurocode and the calibrated model gave strengths above the test result. As the density was low, this was to be expected and the Eurocode likely gave the more accurate result.

For having such a low strength, the sample standard deviation for the strength data from the tests was quite high.

D-Pb-Lc The mean density of the specimens used in this test was a little below the desired value for the strength class and the sample standard deviation was rather high. Because of limited material availability and knots in the one of the test specimen's loaded zones, the sample size for the strength calculations was reduced to seven. The strength estimate from the initial model was an underestimate for this case, while the calibrated model gave a good estimate. For this double height case, the Eurocode overestimated the strength.

Strength data sample standard deviation was not very high, keeping in mind that sample size was too small and density data sample standard deviation rather high.

H-Pb-Lc The final specimen set had a density below the mean value for the strength class. It also had the greatest sample standard deviation of all the sets for this data,

meaning the strength was expected to be a little low with significant difference between the specimens. Both models overestimated the strength in this case, the calibrated one by a lot. The Eurocode provided a reasonable result.

As expected with a high sample standard deviation for the density data, the sample standard deviation for the strength data was rather high.

Summary of Strength Estimates from the Model

Interestingly, the initial model seemed to give decent estimates for the first four cases. The calibrated model, being an attempt at matching the post fracture behavior, was far off the mark in all cases except the case with double height. These observations had an interesting implication: Since two models with significantly different material property input both estimated at least one case rather well but was far off the mark in several other cases, it was unlikely that the current material model was capable of remaining accurate when changing loading or geometry. It did however seem like the initial model was somewhat capable of modeling different pith location cases with load centered and original geometry rather well.

The problems with altering geometry and loading might have been related to the fact that it required a whole model rather than the half one with a symmetry boundary condition. While mesh and material model was assigned as a mirror about the symmetry plane, the use of the whole model might have caused some unexpected issues.

It was puzzling that the Eurocode estimated so well for many of the cases. After all, the calculations were done with characteristic values, while the data from the tests were a mean. This result supported the findings of Mackenzie-Helnwein, Eberhardsteiner and Mang [18].

6.2.2 Post Fracture Behavior

All the model runs that converged beyond first fracture had a crack growth that propagated far too deep in the sill for the displacement applied. This is clearly seen in figure 6.3. When comparing this crack to a real one, like the one shown in figure 5.8, it was clear that the real case had a far more complex crack growth.

In the real cases, the cracks propagate through a few layers of fibers vertically before shooting off horizontally along the grain. This stabilizes the crack growth by effectively creating a new undamaged hammock. This also relaxes the shear on the fibers at the top of the hammock.

In the model, the limitations enforced by the use of XFEM forces the crack to propagate vertically. Three effects were identified as possible causes for the large strength loss:

1. The asymptotic stress field around the crack tip causing premature failure.

2. Weaknesses in the softening scheme causeing the fracture criterion to activate prematurely.

3. No cracks shooting off horizontally, hindering the shear stresses in the fibers from relaxing after a fracture as the material to the left and above the crack tip, as clearly seen in figure 6.3, still supports the fibers vertically.

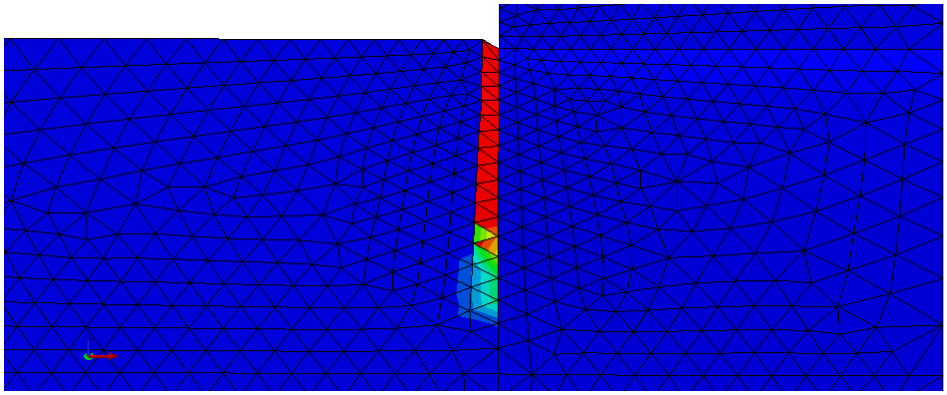

Figure 6.3: Crack propagating in the sill at the end of a test

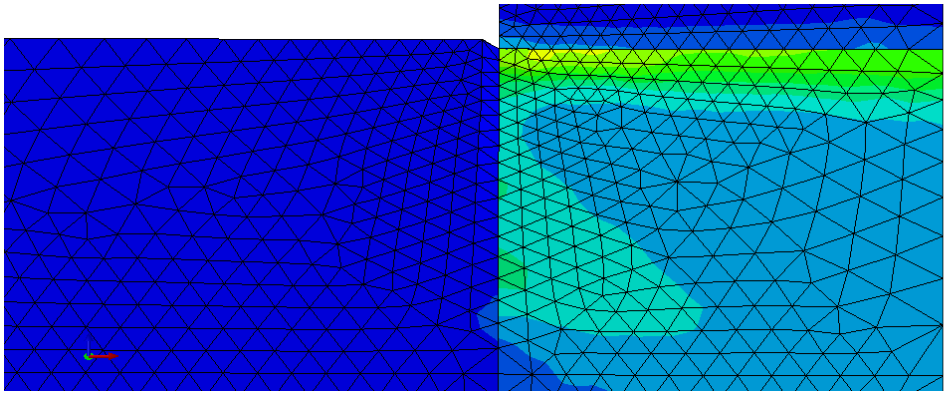

Figure 6.4: Max principal strain at the end of a test

As seen in the strain contour plot in figure 6.4, no stress was transferred across a crack surface.

The sum of these issues was simply the behavior seen for the model: Cracks propagated much deeper than in the real case for any displacement and post-fracture strength loss was far too great. No good solution was found to address these problems within the limitations of the program.

6.2.3 Utility

It was clear that the model in its current state needed more work to be accurate enough for practical use. While it might have uses in testing certain parameters influence on initial fracture load, it was not able to properly model post fracture behavior. A strategy for new design rules proposed by Mackenzie-Helnwein, Eberhardsteiner and Mang [18] was to have rules dependant on the conseqences of failure; it was clear from the laboratory tests that fracture does not mean catastrophic failure. Therefore, they argue, design rule ULS may be divided into a failure stress for joints where the fracture would be dangerous and a higher stress for joints where the initial fracture would not cause significant trouble.

As such, the model may be used as a basis for a model used to find sensible factors for additional parameters in the design rules for the first case where the initial fracture is dimensioning. This requires a comprehensive parameter study, but it was clear that the design rules could be improved significantly by accounting for factors such as pith location, height of the cross section and to a greater degree the length of free ends.

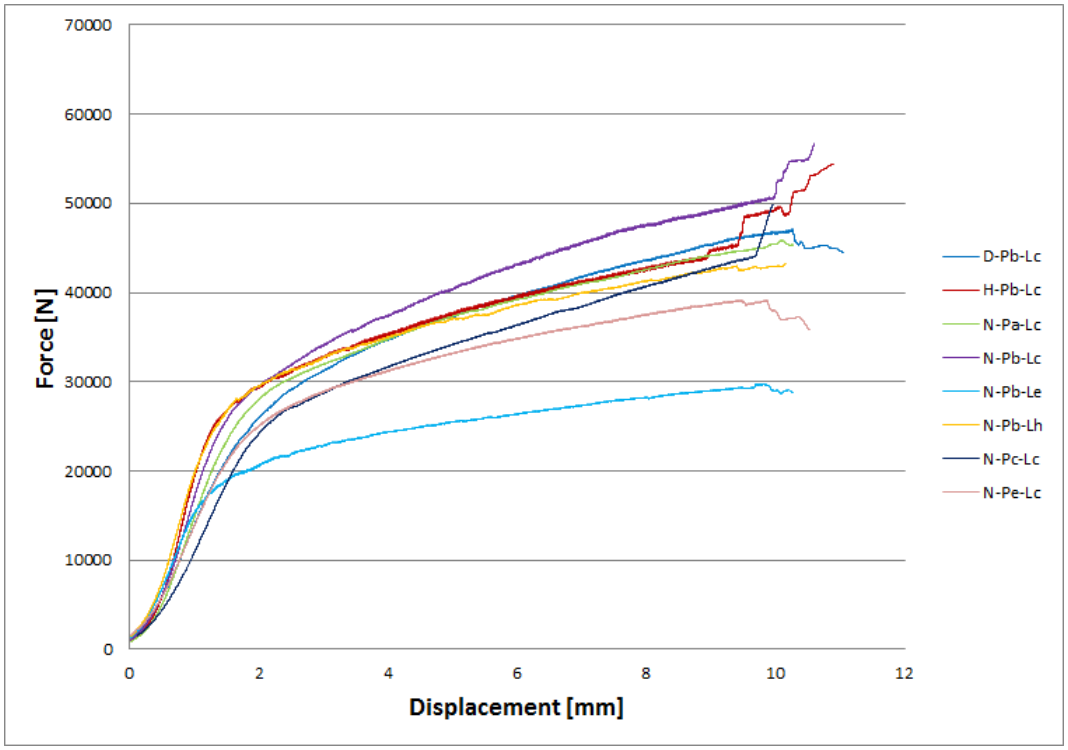

Figure 6.5: Floating averages for all tests

6.3 Significance of Parameters

In light of lessons learned through modeling and laboratory tests, this section is used to evaluate the significance of the parameters that have been tested in this paper. Figure 6.5 shows the floating average of all relevant specimens for all the tests. The legend is alphabetical and the final part of each graph is messy as not all specimens had the same end deformation after normalization, due to different initial extension.

6.3.1 Pith Location

Table 6.1 showed that there was not a lot of variation in the strength of the sill from pith placement, however the test with the pith in the center had too few specimens for this result to be conclusive.

From inspection of figure 6.5, it was clear that pith location does influence the post failure strength of the sill; sorted from strongest to weakest as pith below, pith above, pith centered and pith in the corner. Average densities are also an influence, yet the strongest of the lot with the pith below did not have the highest density.

Another factor should be considered: Inspection of the load-displacement diagrams in subsection 4.3.1 indicates that the different pith locations have different failure development. This is irrelevant to first failure strength, but is significant for a separate ULS for structures where partial failure will not be critical. Clearly, a seemingly ductile load-displacement response is more desirable than sudden loses of strength resulting in displacement jumps. With this in mind, it was clear that the case with the pith below is less desirable as the failures seem to cause greater displacement jumps than the other pith locations.

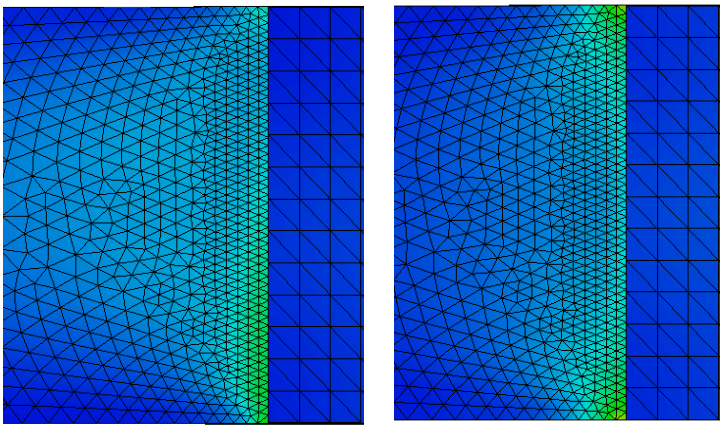

(a) Pith at corner (b) Pith below

Figure 6.6: Top view of logarithmic strain across the width of the sill before failure

Both the cases with the pith at the edge and above the sill top had much smoother load-displacement response. Figure 6.6 shows the likely cause using the strain fields from the numerical models. For the case with the pith in the corner, the strain was unevenly distributed across the sill width because of the material orientations. Such a distribution implies that the failure will start above the pith, which is aligned with the bottom edge of the figure, and gradually spread across the sill width with one crack front. The case with the pith below however, has two areas with greater strain which implies two crack fronts and thus a greater loss of strength at failure. A lower strain gradient, as seen for the case with pith at the corner, also indicates steady progressive failure, rather than sudden brittle failure.

It is clear that design rules allowing post failure deformation in the ULS should include a factor related to pith location, both accounting for strength variations and the difference in loss of strength during cracking.

The case with the pith centered had too few specimens to be commented.

6.3.2 Load Placement

Figure 6.5 along with table 6.1 implied that placing the load on or near the edge of the sill can significantly lower the strength. It had to be taken into account that the sills where load was placed near the edge had an average density close to the desired value, while the specimens used for the load on edge test had a very low average density.

Even so, the implication of the laboratory test was clear. Figure 4.9 clearly showed that horizontal cracks have propagated the 45mm to the edge, meaning that there was strength to be had beyond the 30mm edge lengths allowed in the Eurocode and even beyond the 45mm used in the test.

For the post-fracture behavior, the horizontal cracks cause a greater loss of strength during fracture as clearly seen in figures 4.8 and 4.10. This means that the use of short end lengths should be severely restricted if the post-fracture part of the load-displacement diagram is to be utilized in structural design.

6.3.3 Sill Geometry

Table 6.1 showed that the strength changed little when changing the geometry of the sill. However, figure 6.5 showed that the response of the taller cross section was softer in the linear range. It was difficult to draw conclusions from the results as the double height cross-sections ended up with a sample size of seven that had a high variation in density while the half height specimens just had huge variations in density. The average densities of the two test sets were quite similar.

Despite this, there seemed to be some implications of the tests. First of all, figure 4.12 showed that the half height samples had a tremendous variation in response, while figure 4.11 showed that the double height samples were nicely aggregate. As both had quite a lot of variation in density, this implied that a low cross-section is much more sensitive to variations in material quality than higher cross-sections. Clearly, this variation is of significance to design and should be included.

The post fracture response had some interesting differences as well, as the lower cross-section seemed to lose a lot more strength during fractures than its taller relative. This implied that fracture in higher sills is more stable, which should be included as a factor when using post-fracture strength in structural design.

Chapter 7

Conclusion

The numerical model that was created for this thesis proved to be less usefull than what was initially hoped for. Being a 3D model, analysis time was high, making adjusting and testing the model very time consuming on the hardware available. It also limited the use of certain modeling tools, as well as making desired changes to mesh fineness and interactions with the surroundings very computationally expensive.

The model produced reasonable fracture loads for the first load and geometry configurations, but was unsuited for handling the load and geometry variations attempted. Restrictions and limitations in the software used made the strategy chosen for modeling crack growth unsuitable, as the crack propagation pattern in the model could not be made to match that of the real case.

Laboratory tests yielded useful data regarding strength and post-fracture behavior. Along with data extracted from the numerical modeling, it was possible to evaluate the significance of parameters that were varied in the laboratory tests.

It was shown that pith location has a significant impact on the material response at and beyond first failure, while not affecting strength to any great degree.

Free ends longer than what is used for calculations in the Eurocode was shown to impact the strength, as well as having serious implications in post-fracture behavior.

Finally, the height of the cross-section of the sills was shown to be an important factor, affecting the impact of material variability on the response and strength. Height also seemed to impact the response beyond first fracture, giving a much more stable and smooth response for higher cross-sections.

It was concluded that these parameters should be considered when revising the rules for the ULS for pressure perpendicular to the grain. Given a revisal where utilization of the post-fracture range, it was concluded that consideration of the parameters tested would be important.

Chapter 8

Further Work

Further works includes improving the current model and material model, implementing better solutions as they become available and doing more laboratory studies.

Clearly the material models in the Abaqus software has a way to go before wood can be accurately modeled. As new tools become available, the model can be improved and a new comparison with test results can be done. Hopefully, several of the criteria that are currently available only in two dimensions, such as Tsai-Wu and Hashin damage, will shortly be available for three dimensions. Using stronger hardware, some of the impracticality of having to wait half a day for analysis results when doing minor adjustments can be mitigated. Given a stronger computer, it would also be possible to remake the model with a finer mesh and better suited boundary conditions while keeping analysis time down, this might yield better results particularly for the linear-elastic range.

The laboratory data gathered is not as comprehensive as what would be desired. Further laboratory studies and empirical study of the data can yield interesting results as to the significance of parameters both with and without the use of a numerical model.

Sills that have been compressed regain a lot of their original shape. An interesting laboratory study would be cyclic loading of sills up to different displacements around and above the ULS. The development over time could be very relevant to a revisal of the design rules if post-fracture loading is to be allowed.

A lot of the data related to the nonlinear behavior of wood is woefully lacking. Studies can be done finding crack driving force for all fracture modes in all directions to better model the behavior of cracks. The stress strain relationship beyond ultimate stress and strain for compression perpendicular to the grain is obscure. Clearly, no collapse akin to tension failure happens so data for the stress-strain curve beyond ultimate stress is needed.

Bibliography

[1] Ns-en 338 structural timber - strength classes, 2003.

[2] Eurocode 5: Design of timber structures part 1-1: General common rules and rules for buildings, 2009.

[3] J.C.M. Schoenmakers A.J.M Leijten. Bearing strength perpendicular to the grain of locally loaded timber blocks.

[4] Artec. Verdens høyeste trebygg. "http://www.artec.no/index.php", 2011.

[5] Petter Aune. *Trekonstruksjoner*. Tapir forlag, 1992.

[6] K.B Dahl. *Mechanical properties of clear wood from Norway spruce*. PhD thesis, Norwegian University of Science and Technology (NTNU), 2009.

[7] H. Danielson. The strength of gluelam beams with holes: A survey of tests and calculation methods. *Structural Mechanics*, page 97, 2006.

[8] A. N. Foulger. *Classroom demonstrations of wood properties*. U.S Department of Agricultre, Forest service, forest products laboratory, 1969.

[9] A. A. Griffith. The phenomena of rupture and flow in solids. In *Philosophical transactions of the royal society of London. Series A, containing papers of a mathematical or physical character*, volume 221, pages 163–198. The Royal Society, 1921.

[10] A. Hanhijärvi. Modeling of creep deformation mechanisms in wood. *VTT Publications*, 231:143, 1995.

[11] Rainer Görlacher Hans J. Blass. Compression perpendicular to the grain. *World conference Timber engineering*, pages 435–440, 2004.

[12] Alvis Hardeng. The bearing capacity of locally loaded beams and sills for compression perpendicular to the grain. Master's thesis, Universitetet for miljø- og biovitenskap, 2011.

[13] Rodney Hill. A theory of the yielding and plastic flow of anisotropic metals. *Proceeding of the Royal Society of London*, 193:281–297, 1948.

[14] Instron. 5900 series - advanced mechanical testing systems. "http://www.instron.se/wa/product/5900-Series-Mechanical-Testing-Systems.aspx", June 2012.

[15] Ori Ishai Isaac M. Daniel. *Engineering mechanics of composite materials*. Oxford University Press, Inc., 2006.

[16] Benjamin A. Jayne Jozef Bodig. *Mechanics of wood and wood composites.* Krieger publishing company, 1993.

[17] Bohumil Kucera. *Skandinaviske normer for testing av små feilfrie prøver av heltre.* Skogforsk, 1992.

[18] H. A. Mang P. Mackenzie-Helnwein, J. Eberhardsteiner. A multi-surface plasticity model for clear wood and its application to the finite element analysis of structural details. *Computational Mechanics*, 31:204–218, 2003.

[19] H. Ribberholt. Compression perpendicular to the grain of wood. Technical Report P-42239-1, COWI, 2000.

[20] Michael E. Plesha Robert J. Witt Robert D. Cook, David S. Malkus. *Concepts and Applications of Finite Element Analysis.* John Wiley & Sons Ltd., 4th edition edition, 2001.

[21] M. K. J. Schmidt. Models for numerical failure analysis of wooden structures. *Engineering Structures*, 31:8, 2008.

[22] Edward M. Wu Sephen W. Tsai. A general theory of strenght for anisotropic materials. *Composite Materials*, 5:58–80, 1971.

[23] Line Sigbjørnsen. Shear properties of nordic glulam ce l40c. Master's thesis, Norwegian University of Science and Technology (NTNU), 2012.

[24] Simulia. *Abaqus Analysis User's Manual*, 6.10 edition.

[25] Simulia. *Abaqus/CAE User's Manual*, 6.10 edition.

[26] T. Black T. Belytschko. Elastic crack growth in finite elements with minimal remeshing. *International journal for numerical methods in engineering*, 45:20, 1999.

[27] Treteknisk. *Treteknisk Håndbok*, nr. 4 edition, 2009.

[28] C. H. Wang. *Introduction to Fracture Mechanics.* DSTO Aeronautical and Maritime Research Laboratory, 1996.

Appendix A

Laboratorium Test Plan

A.1 General Setup for Testing

A.1.1 Tools

- Test rig for compressing sills
- Teflon film to achieve low friction with bottom surface
- Computer program for post-processing data, excel used
- Camera for documentation, Nikon D70 used

A.1.2 Execution

- Tests should be run beyond fracture to evaluate post-fracture response that may be signifigant to properties in the numerical model

A.2 Pith Location Test 1 (N-Pc-Lc)

Purpose

The purpose of this series of tests is to check if the calibrated numerical model is still valid if the pith changes location to the center of the sill. If possible, data from the series may be used to further calibrate the model.

Materials

Clear wood of strength class C24. Sample size is 11.

Figures

- All messures are in metres
- Pith location is approximate

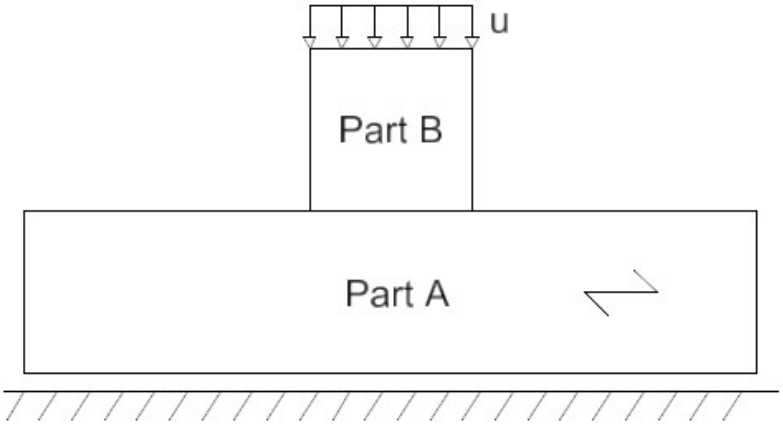

Figure A.1: Pith location test 1 overview

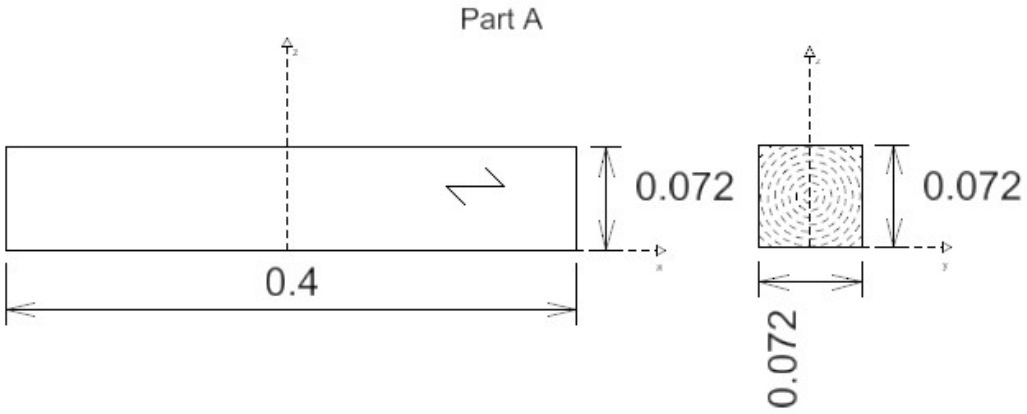

Figure A.2: Pith location test 1 part A dimentions and pith locations

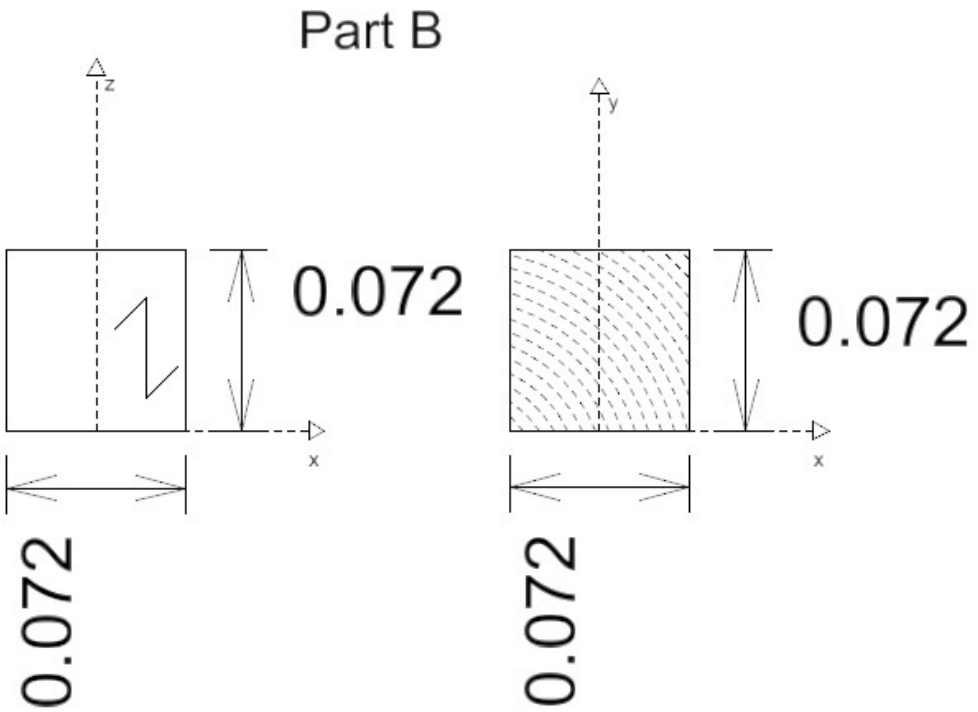

Figure A.3: Pith location test 1 part B dimentions and pith locations

A.3 Pith Location Test 2 (N-Pe-Lc)

Purpose

The purpose of this series of tests is to check if the calibrated numerical model is still valid if the pith changes location to the corner of the sill. If possible, data from the series may be used to further calibrate the model.

Materials

Clear wood of strength class C24. Sample size is 11.

Figures

- All messures are in metres
- Pith location is approximate

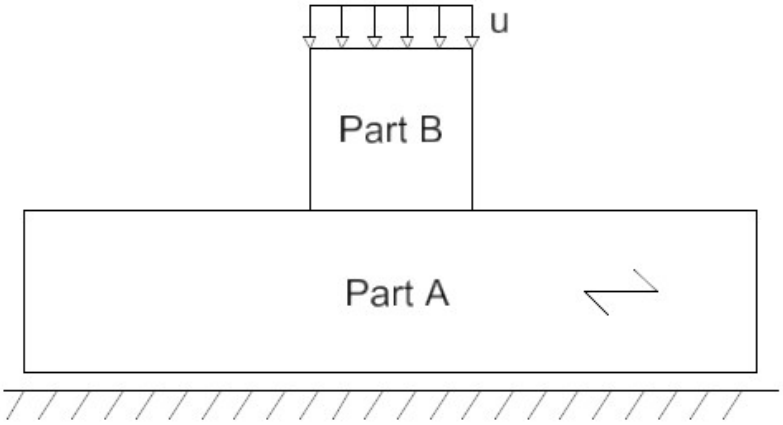

Figure A.4: Pith location test 2 overview

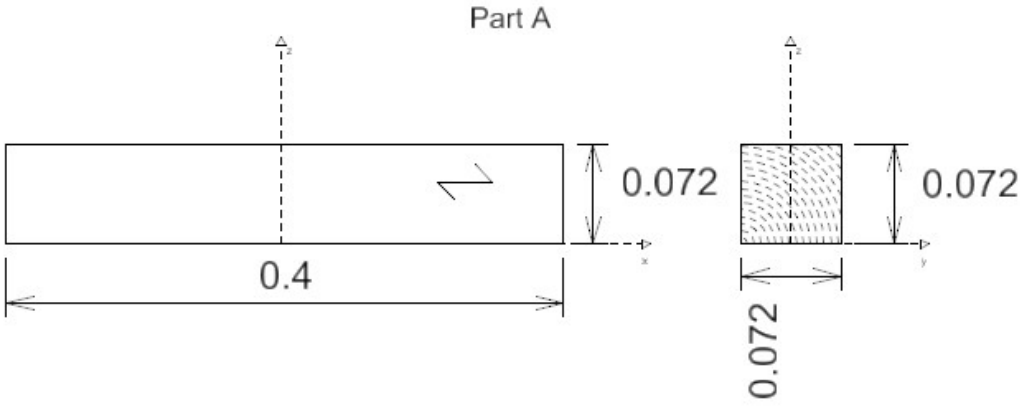

Figure A.5: Pith location test 2 part A dimentions and pith locations

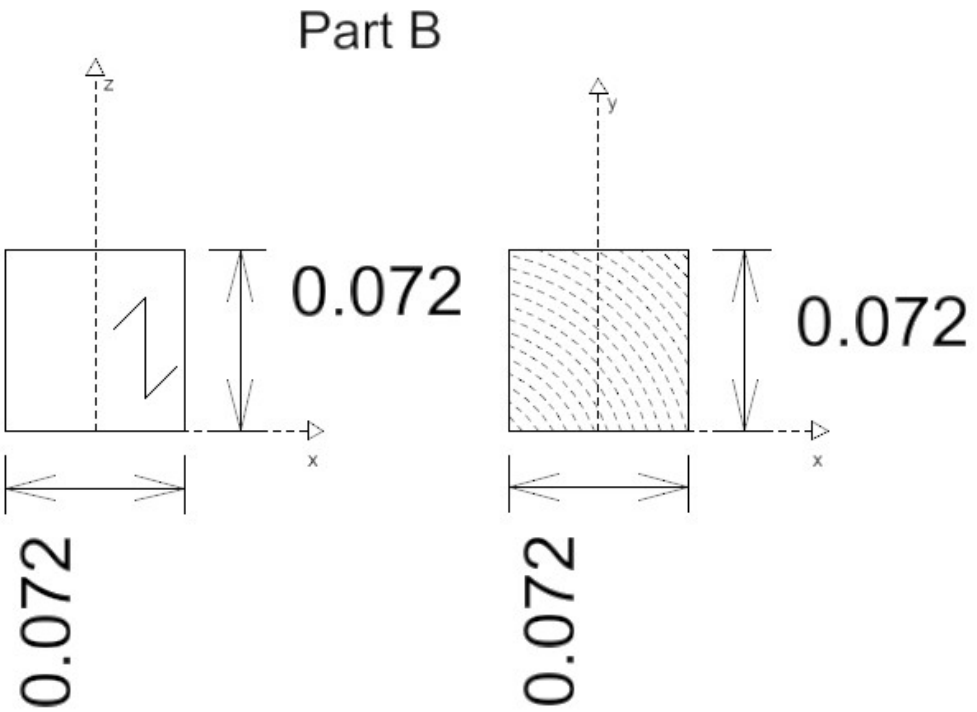

Figure A.6: Pith location test 2 part B dimentions and pith locations

A.4 Pith Location Test 3 (N-Pb-Lc)

Purpose

The purpose of this series of tests is to check if the calibrated numerical model is still valid if the pith changes location to about 37.5mm below the sill. If possible, data from the series may be used to further calibrate the model.

Materials

Clear wood of strength class C24. Sample size is 11.

Figures

- All messures are in metres
- Pith location is approximate

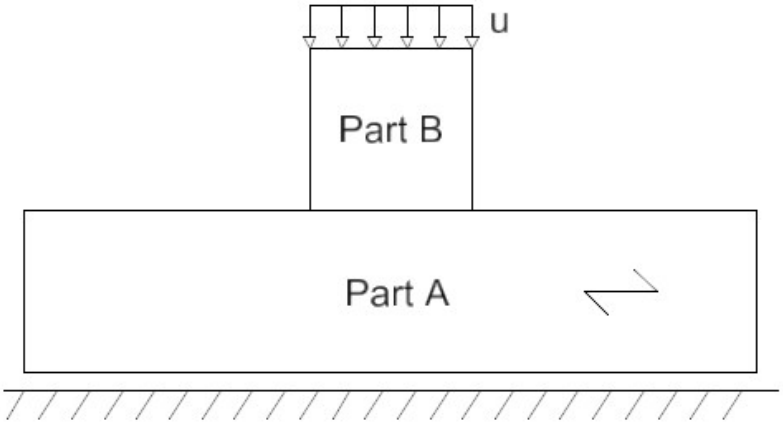

Figure A.7: Pith location test 3 overview

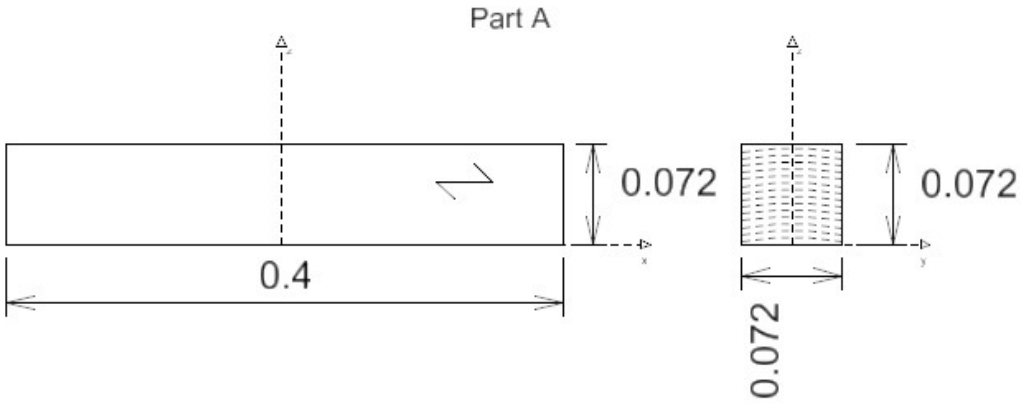

Figure A.8: Pith location test 3 part A dimentions and pith locations

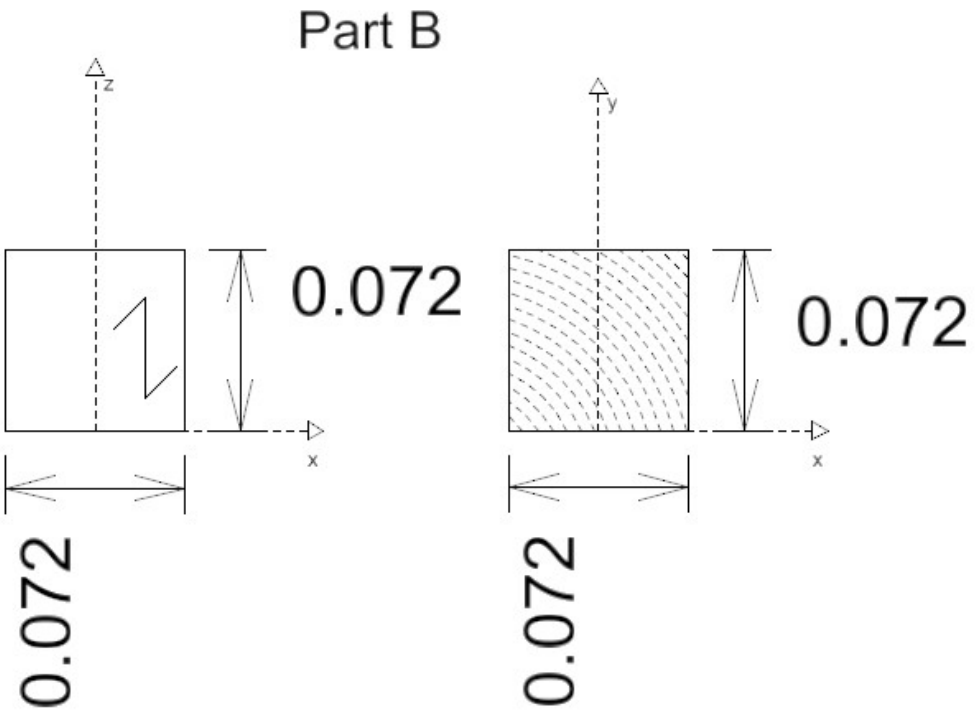

Figure A.9: Pith location test 3 part B dimentions and pith locations

A.5 Pith Location Test 4 (N-Pa-Lc)

Purpose

The purpose of this series of tests is to check if the calibrated numerical model is still valid if the pith changes location to about 37.5mm above the sill. If possible, data from the series may be used to further calibrate the model.

Materials

Clear wood of strength class C24. Sample size is 11.

Figures

- All messures are in metres
- Pith location is approximate

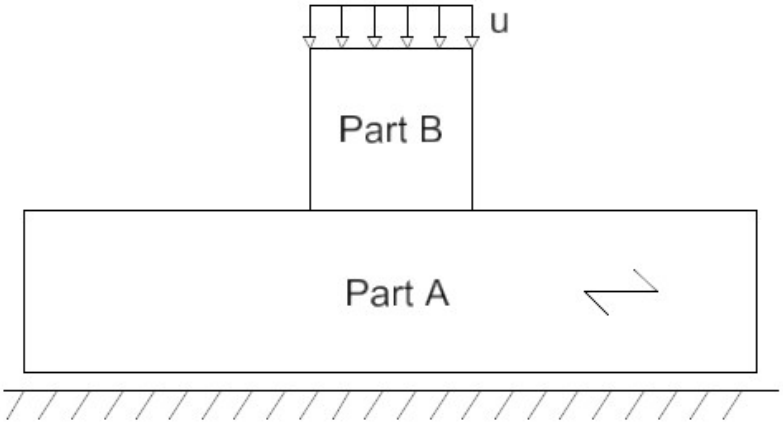

Figure A.10: Pith location test 4 overview

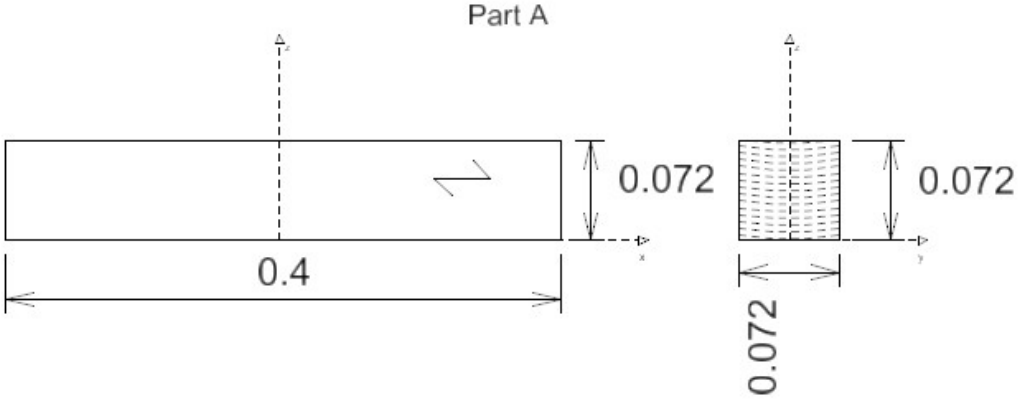

Figure A.11: Pith location test 4 part A dimentions and pith locations

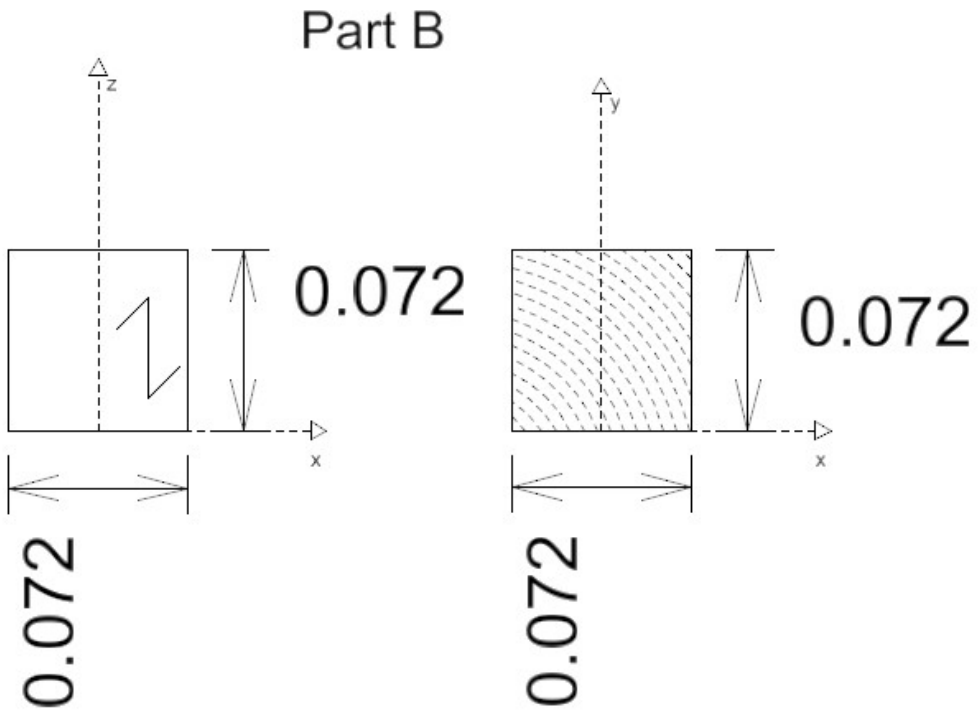

Figure A.12: Pith location test 4 part B dimentions and pith locations

A.6 Load Location Test 1 (N-Pc-Lh)

Purpose

The purpose of this series of tests is to check if the calibrated numerical model is still valid if the load is placed with its edge 45mm from the sill edge. If possible, data from the series may be used to further calibrate the model.

Materials

Clear wood of strength class C24. Sample size is 11.

Figures

- All messures are in metres
- Pith locations are approximate

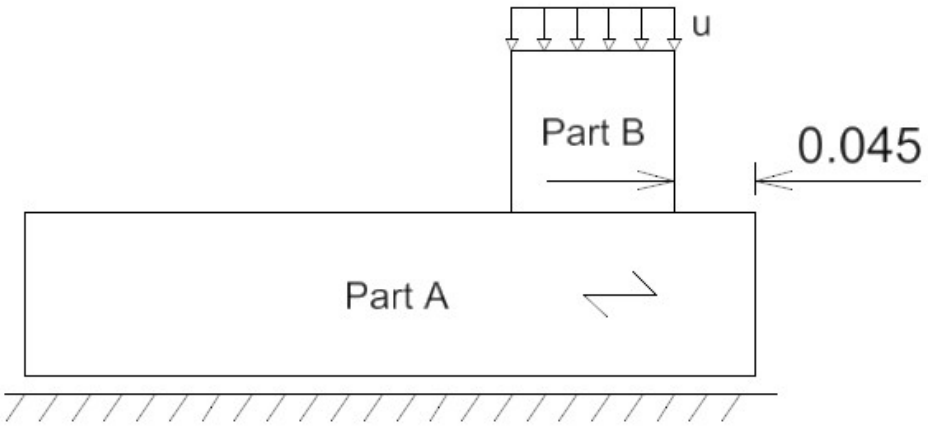

Figure A.13: Load location test 1 overview

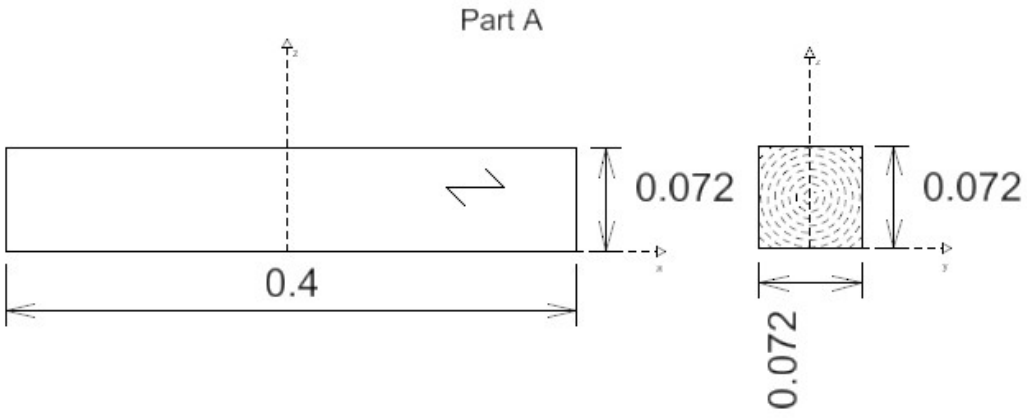

Figure A.14: Load location test 1 part A dimentions and pith locations

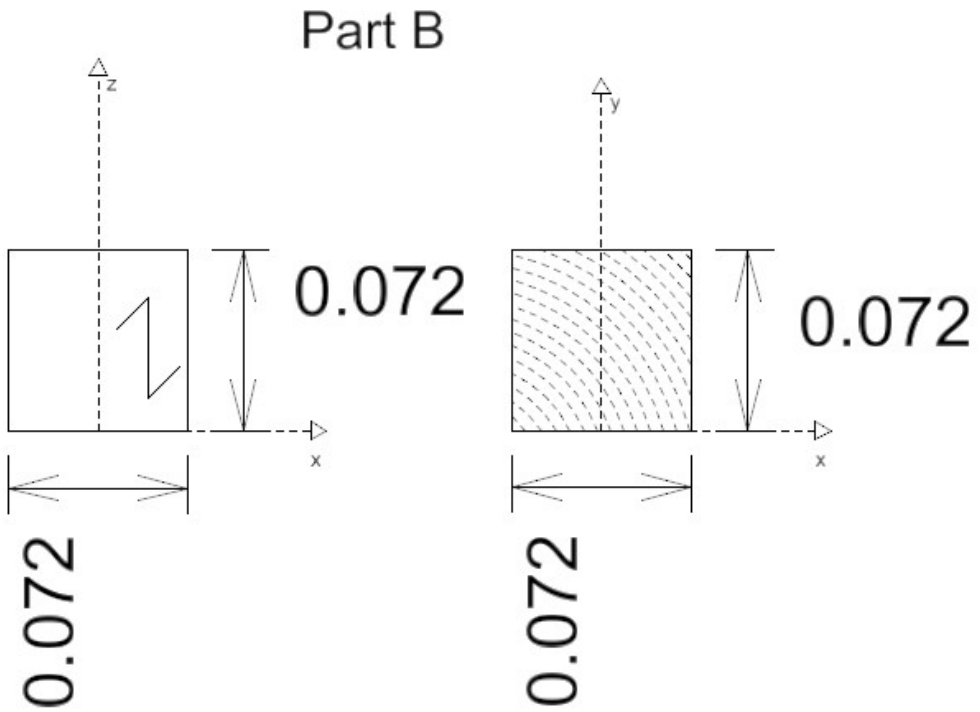

Figure A.15: Load location test 1 part B dimentions and pith locations

A.7 Load Location Test 2 (N-Pc-Le)

Purpose

The purpose of this series of tests is to check if the calibrated numerical model is still valid if the load is placed at the sill edge. If possible, data from the series may be used to further calibrate the model.

Materials

Clear wood of strength class C24. Sample size is 11.

Figures

- All messures are in metres
- Pith locations are approximate

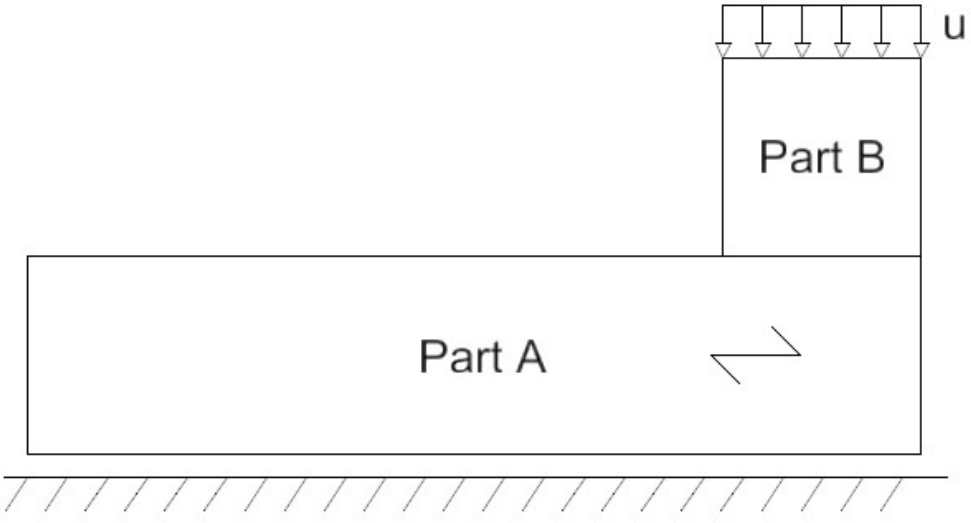

Figure A.16: Load location test 2 overview

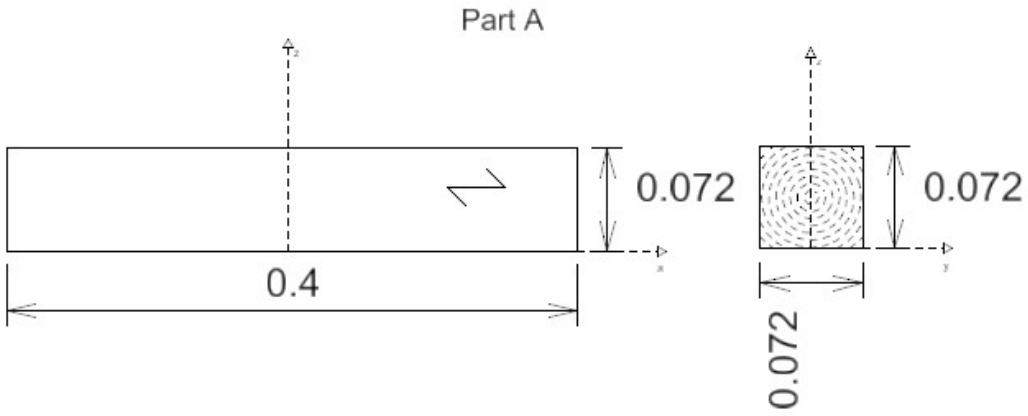

Figure A.17: Load location test 2 part A dimentions and pith locations

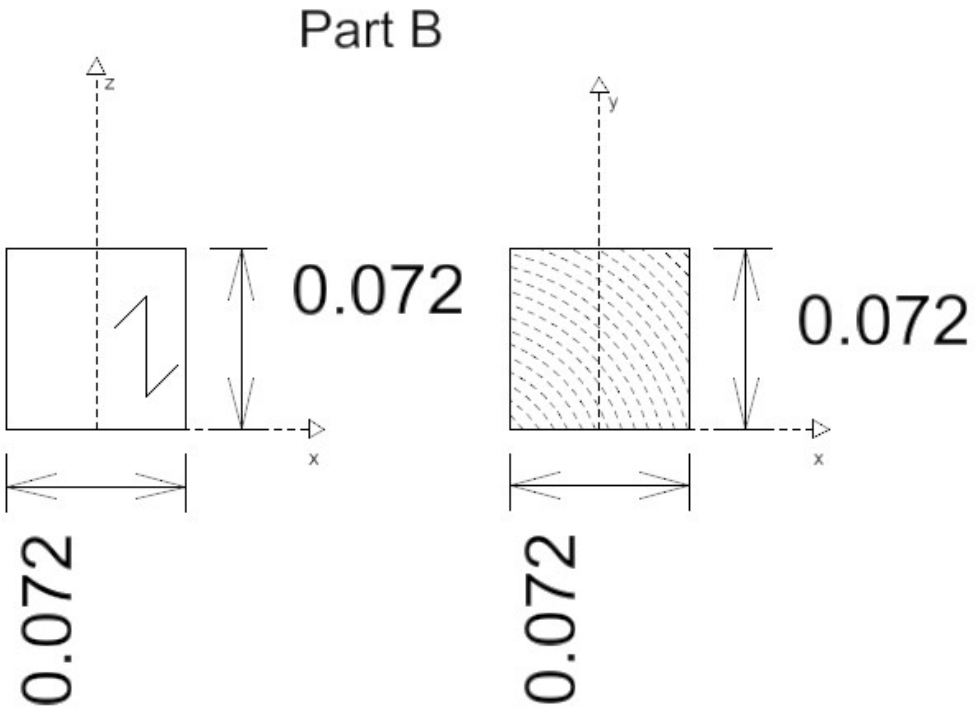

Figure A.18: Load location test 2 part B dimentions and pith locations

A.8 Load Location Test 1 with Alternate Pith Location (N-Pb-Lh)

Purpose

The purpose of this series of tests is to check if the calibrated numerical model is still valid if the load is placed with its edge 45mm from the sill edge. If possible, data from the series may be used to further calibrate the model.

Materials

Clear wood of strength class C24. Sample size is 11.

Figures

- All messures are in metres
- Pith locations are approximate

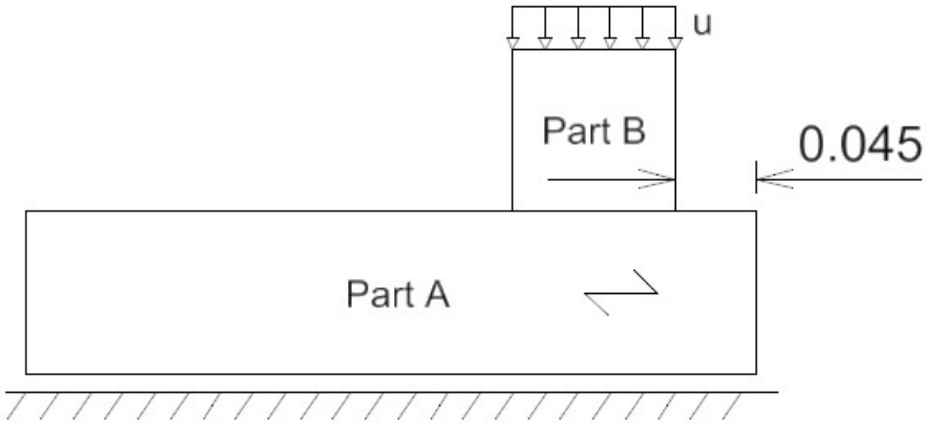

Figure A.19: Load location test 1 overview

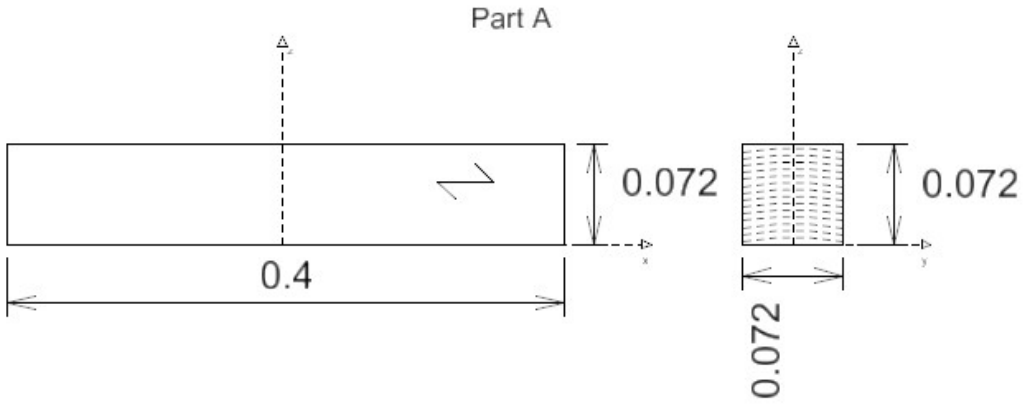

Figure A.20: Load location test 1 part A dimentions and pith locations

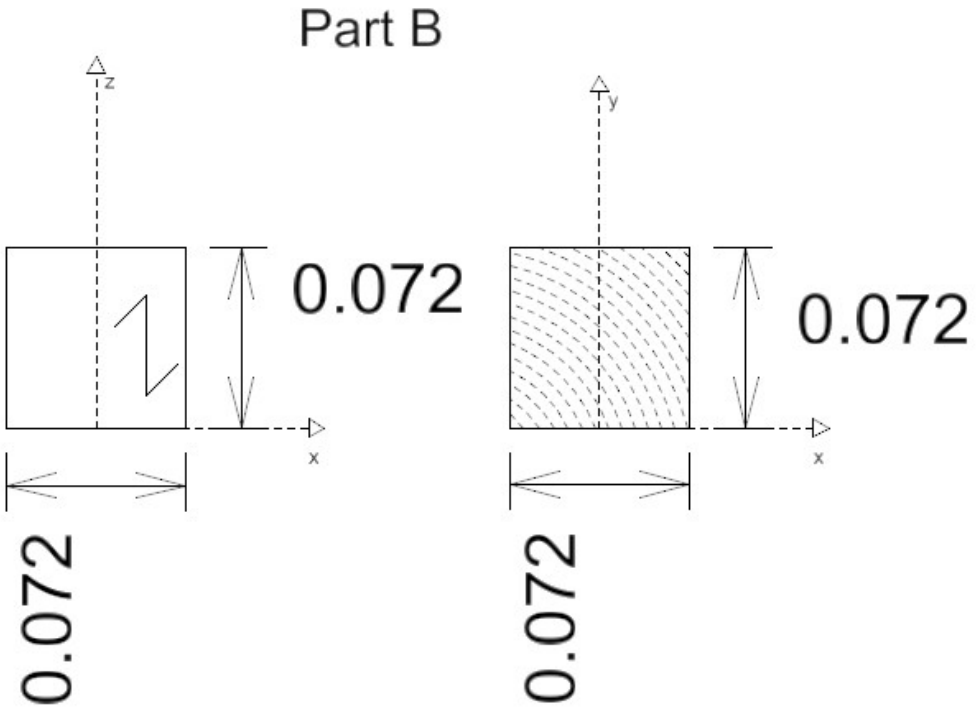

Figure A.21: Load location test 1 part B dimentions and pith locations

A.9 Load Location Test 2 with Alternate Pith Location (N-Pb-Le)

Purpose

The purpose of this series of tests is to check if the calibrated numerical model is still valid if the load is placed at the sill edge. If possible, data from the series may be used to further calibrate the model.

Materials

Clear wood of strength class C24. Sample size is 11.

Figures

- All messures are in metres
- Pith locations are approximate

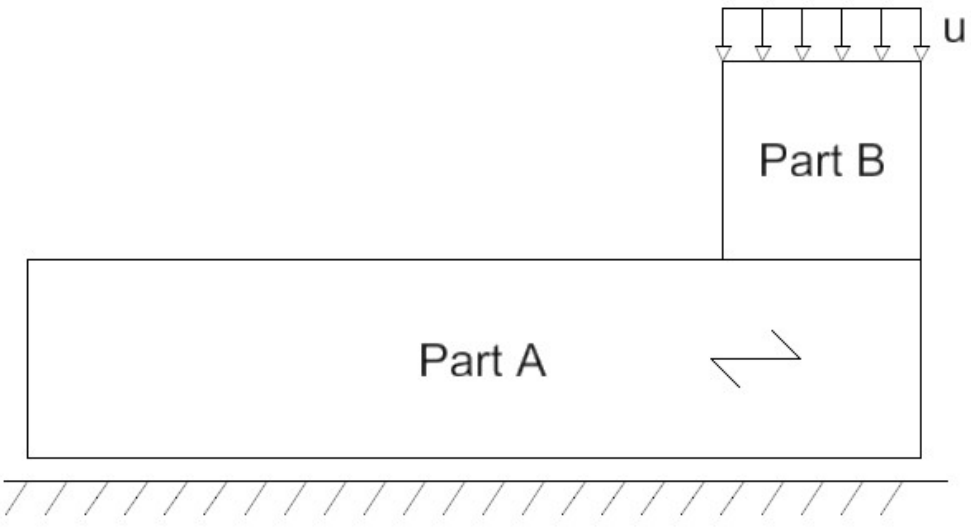

Figure A.22: Load location test 2 overview

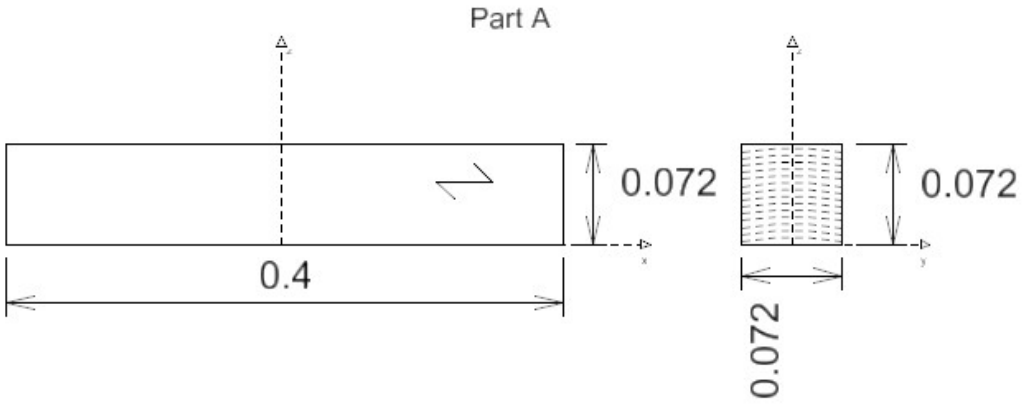

Figure A.23: Load location test 2 part A dimentions and pith locations

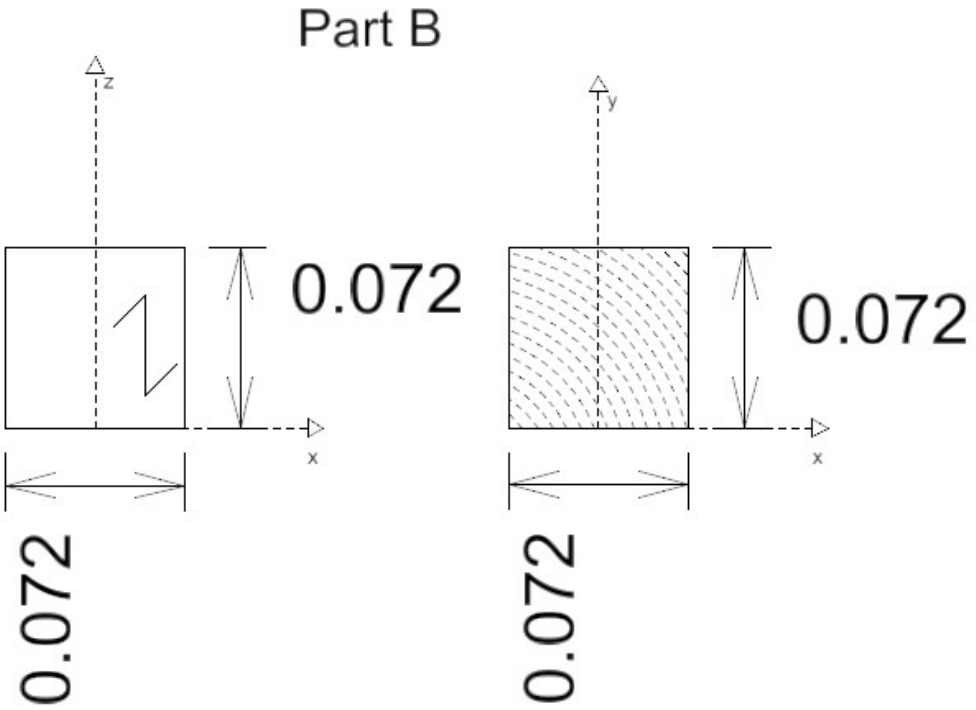

Figure A.24: Load location test 2 part B dimentions and pith locations

A.10 Geometry Test 1 (D-Pb-Lc)

Purpose

The purpose of this series of tests is to check if the calibrated numerical model is still valid if the height of the sill is twice that of the reference case. If possible, data from the series may be used to further calibrate the model.

Materials

Clear wood of strength class C24. Sample size is 11.

Figures

- All messures are in metres
- Pith locations are approximate

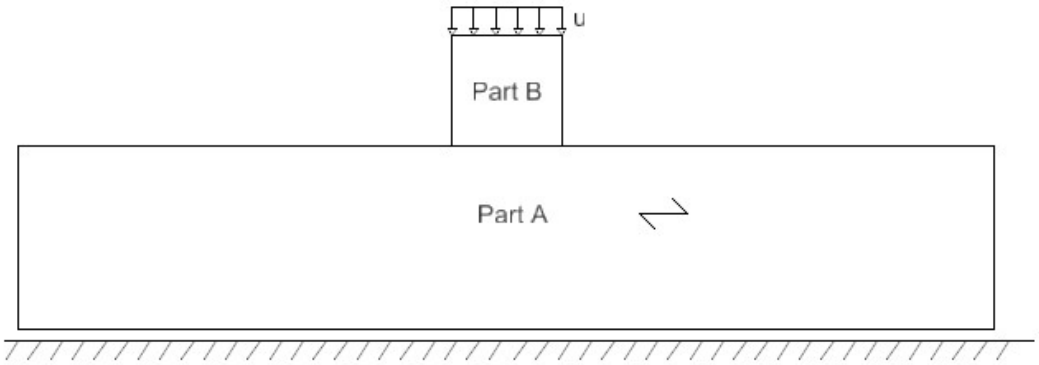

Figure A.25: Geometry test 1 overview

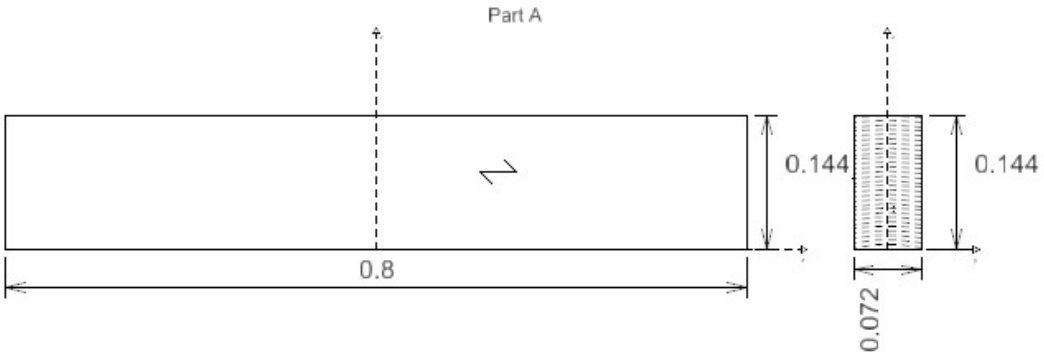

Figure A.26: Geometry test 1 part A dimentions and pith locations

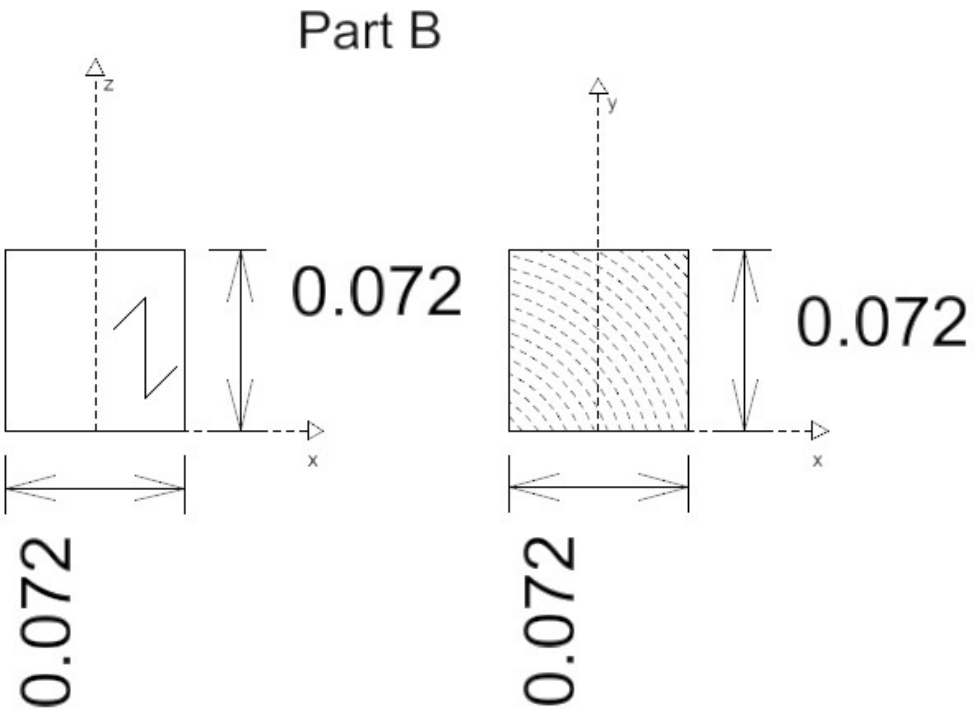

Figure A.27: Geometry test 1 part B dimentions and pith locations

A.11 Geometry Test 2 (H-Pb-Lc)

Purpose

The purpose of this series of tests is to check if the calibrated numerical model is still valid if the height of the sill is half that of the reference case. If possible, data from the series may be used to further calibrate the model.

Materials

Clear wood of strength class C24. Sample size is 11.

Figures

- All messures are in metres
- Pith locations are approximate

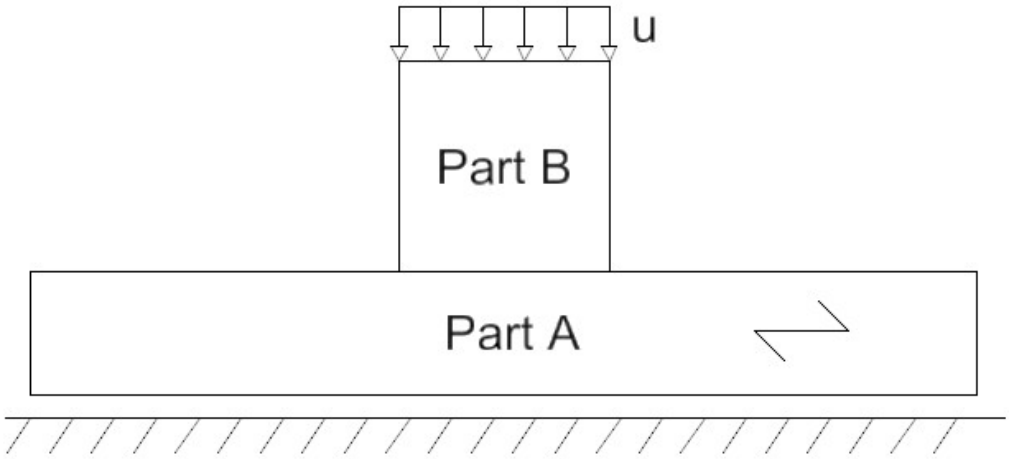

Figure A.28: Geometry test 2 overview

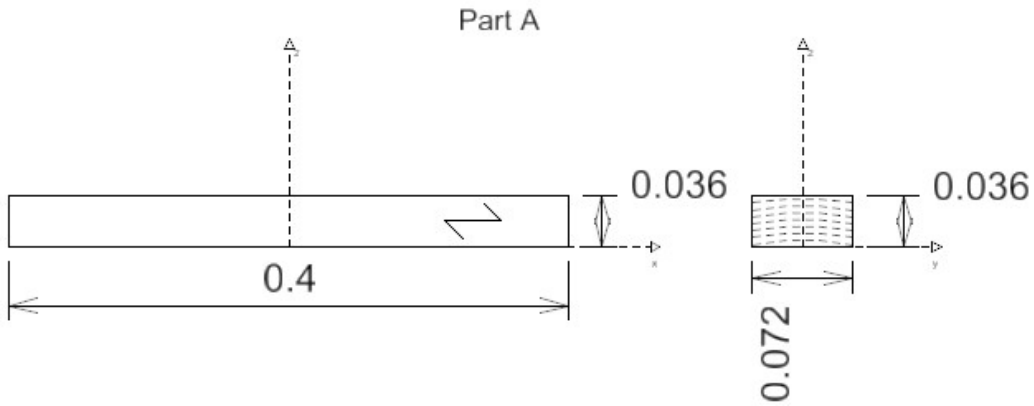

Figure A.29: Geometry test 2 part A dimentions and pith locations

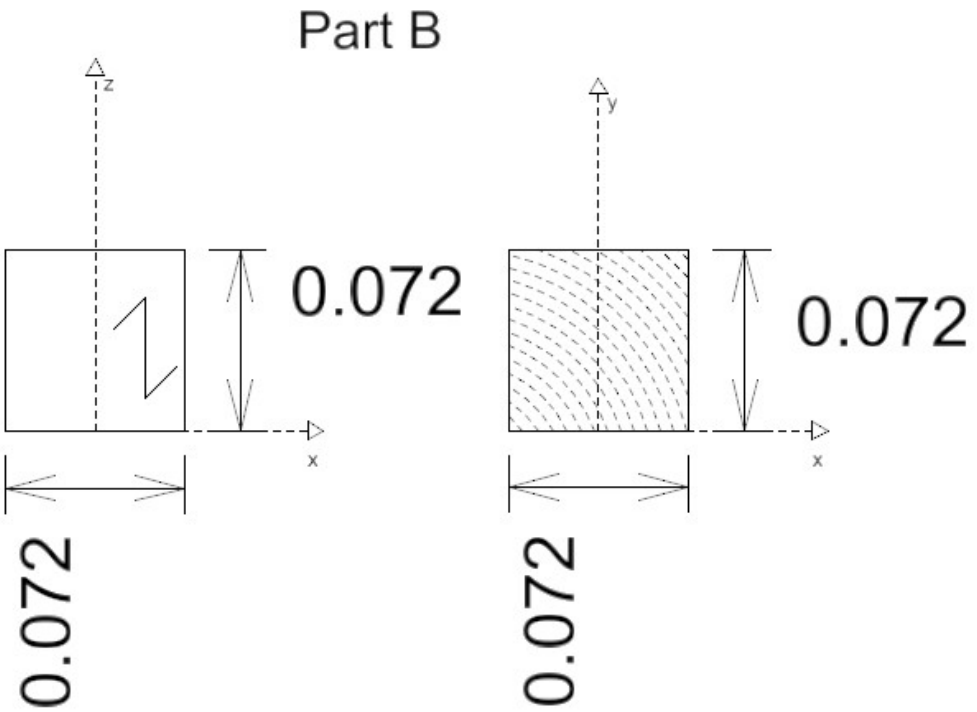

Figure A.30: Geometry test 2 part B dimentions and pith locations

Appendix B

Eurocode Calculations

B.1 General Calculations

Eurocode 5 [2] gives the following rule for the ULS with compression perpendicular to the grain in wood:

$$\sigma_{c,90,d} = \frac{F_{c,90,d}}{A_{ef}} \leq k_{c,90} f_{c,90,d} \tag{B.1}$$

where

$\sigma_{c,90,d}$ is the design compressive stress on the effective contact surface perpendicular to the grain

$F_{c,90,d}$ is the design compressive load perpendicular to the grain

A_{ef} is the effective contact surface for compression perpendiular to the grain

$f_{c,90,d}$ is the design compressive strength

$k_{c,90}$ is a factor accounting for load configuration, spliting of the wood and the magnitude of the compressive deformation

For C24 with climate class 1 and instantaneous load, the following design strength is calculated

$$f_{c,90,d} = 1,1 \cdot \frac{2,5MPa}{1,3} = 2,115Mpa \tag{B.2}$$

All the cases have continuous supports and are of massive softwood, meaning that $k_{c,90} = 1,25$. The expression for maximum compressive force perpendicular to the grain becomes

$$F_{c,90,d} = 1,25 \cdot 2,115Mpa \cdot A_{ef} \tag{B.3}$$

B.2 Cases 1, 2, 3, 4, 5, 7, 9 and 10

In all these cases, there is only one load and end lengths are greater than 30mm. Thus the effective contact surface becomes

$$A_{ef} = 72mm \cdot (72mm + 30mm + 30mm) = 9504mm^2 \tag{B.4}$$

Maximum compressive force for these cases becomes

$$F_{c,90,d} = 1,25 \cdot 2,115Mpa \cdot 10125mm^2 = 25126N \tag{B.5}$$

B.3 Cases 6 and 8

In these two cases, there is only one load, one end length is 0mm while the other is greater than 30mm. Thus the effective contact surface becomes

$$A_{ef} = 72mm \cdot (72mm + 30mm) = 7344mm^2 \tag{B.6}$$

Maximum compressive force for these cases becomes

$$F_{c,90,d} = 1,25 \cdot 2,115Mpa \cdot 7875mm^2 = 19415N \tag{B.7}$$

Appendix C

Plots of Numerical Results

C.1 Numerical Load-Displacement Comparison to Laboratory Results

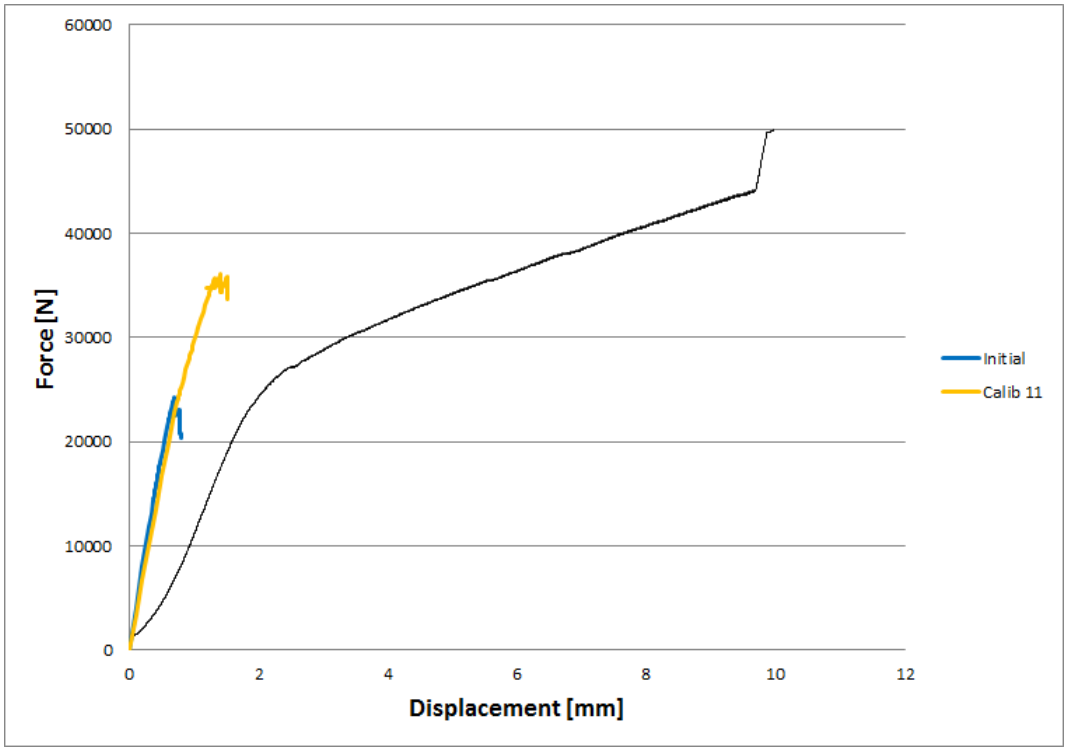

Figure C.1: Load-displacement for case N-Pc-Lc with abaqus model response

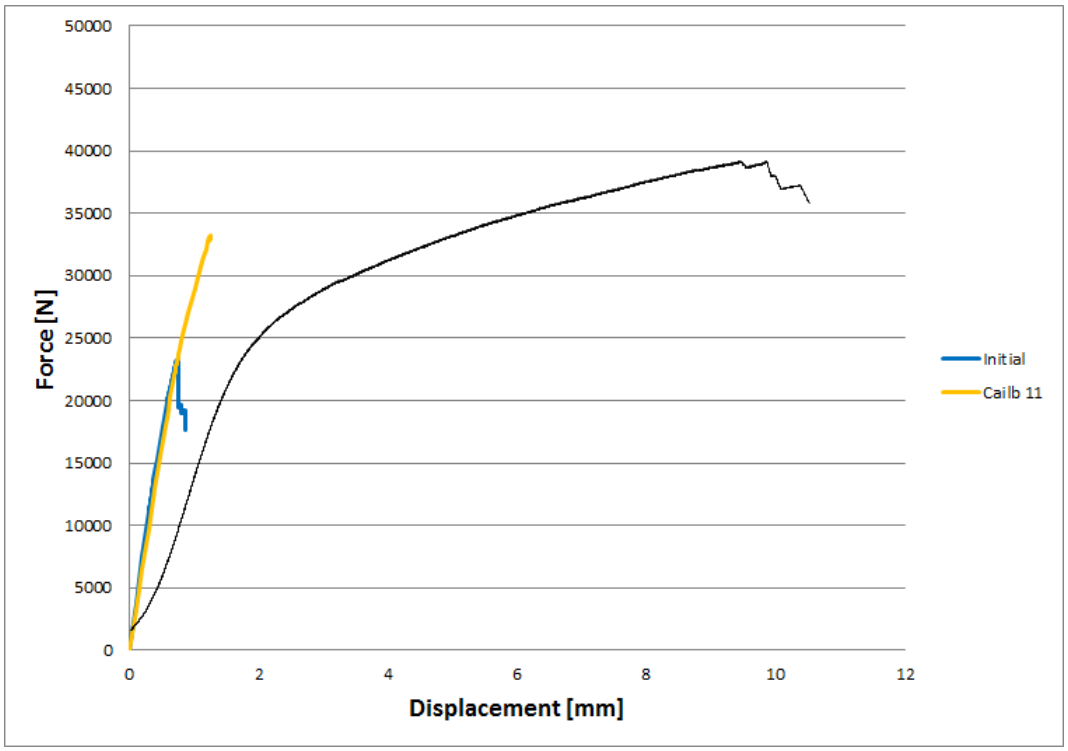

Figure C.2: Load-displacement for case N-Pe-Lc with abaqus model response

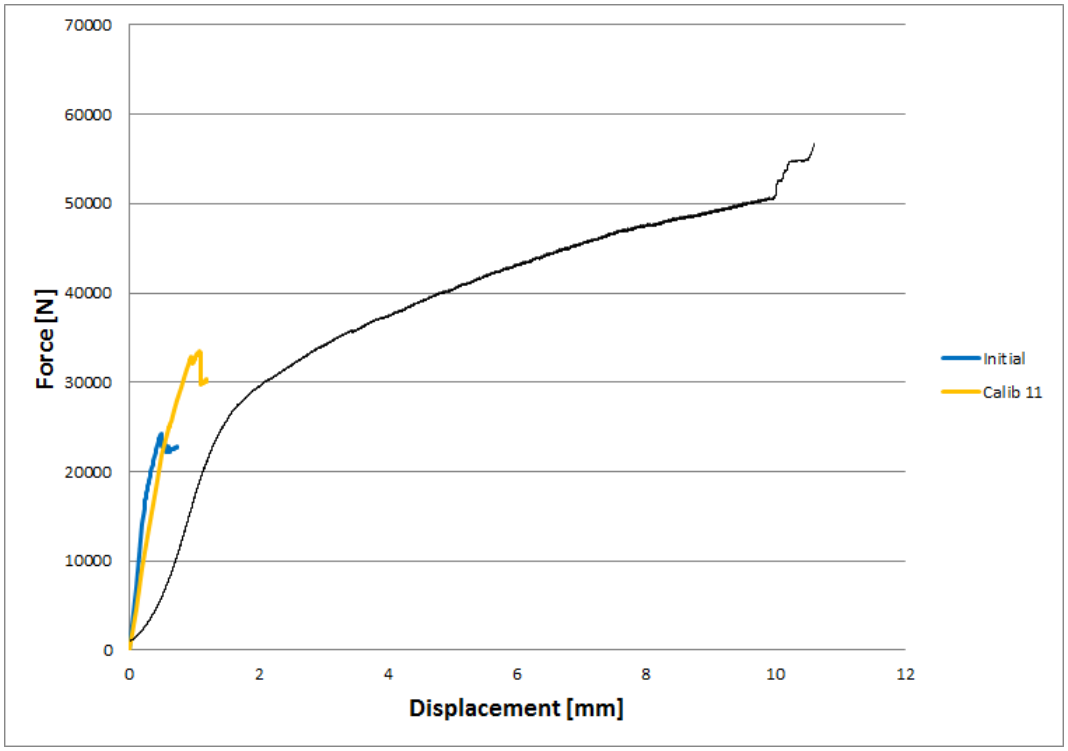

Figure C.3: Load-displacement for case N-Pb-Lc with abaqus model response

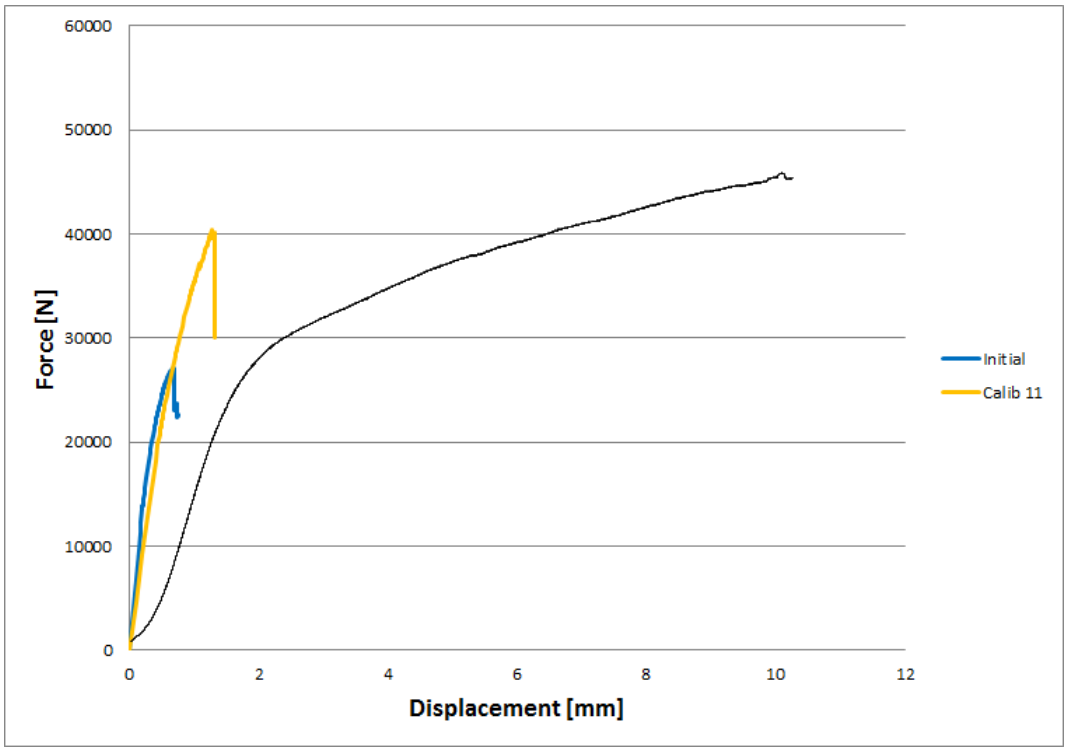

Figure C.4: Load-displacement for case N-Pa-Lc with abaqus model response

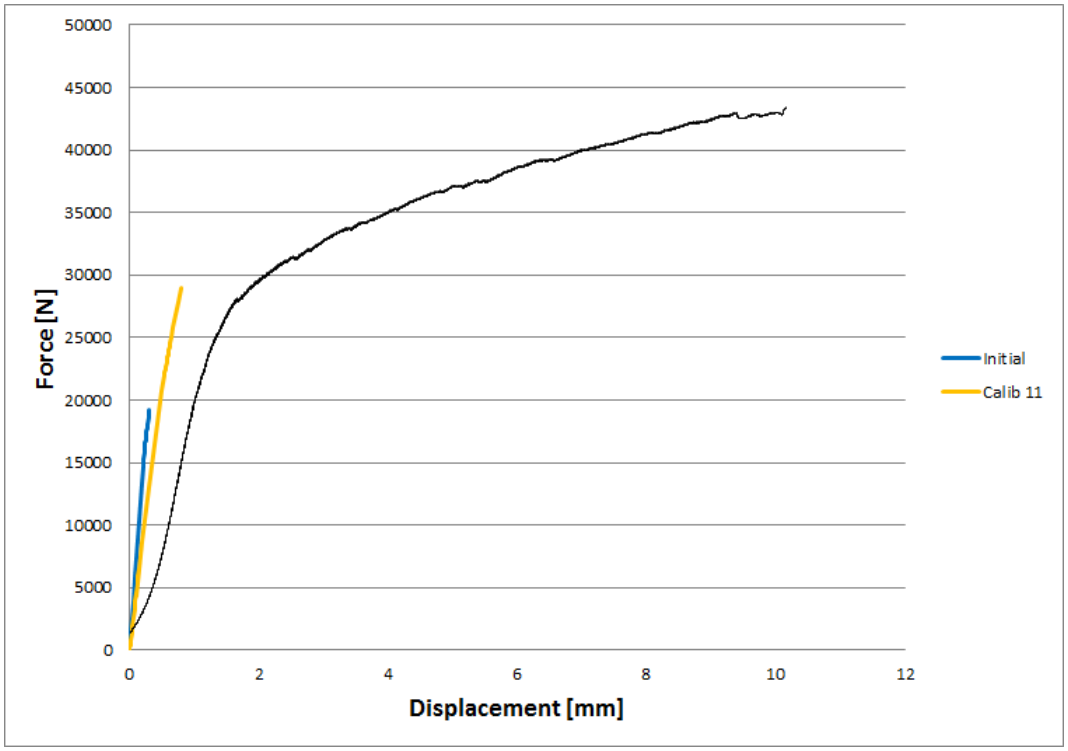

Figure C.5: Load-displacement for case N-Pb-Lh with abaqus model response

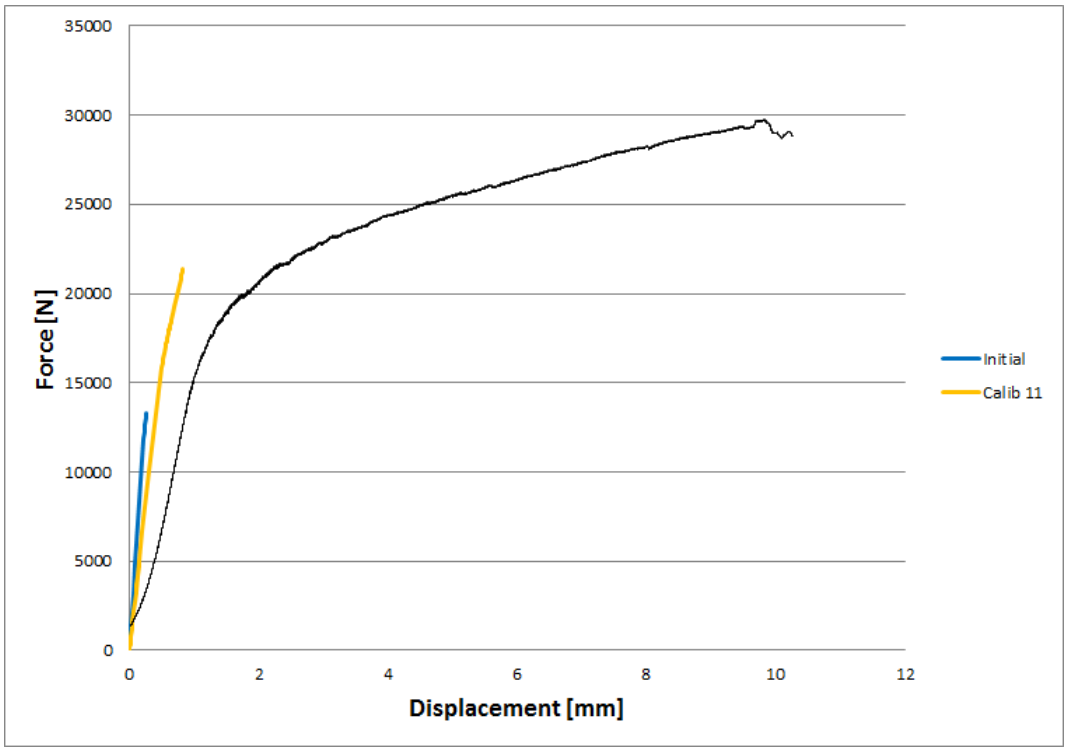

Figure C.6: Load-displacement for case N-Pb-Le with abaqus model response

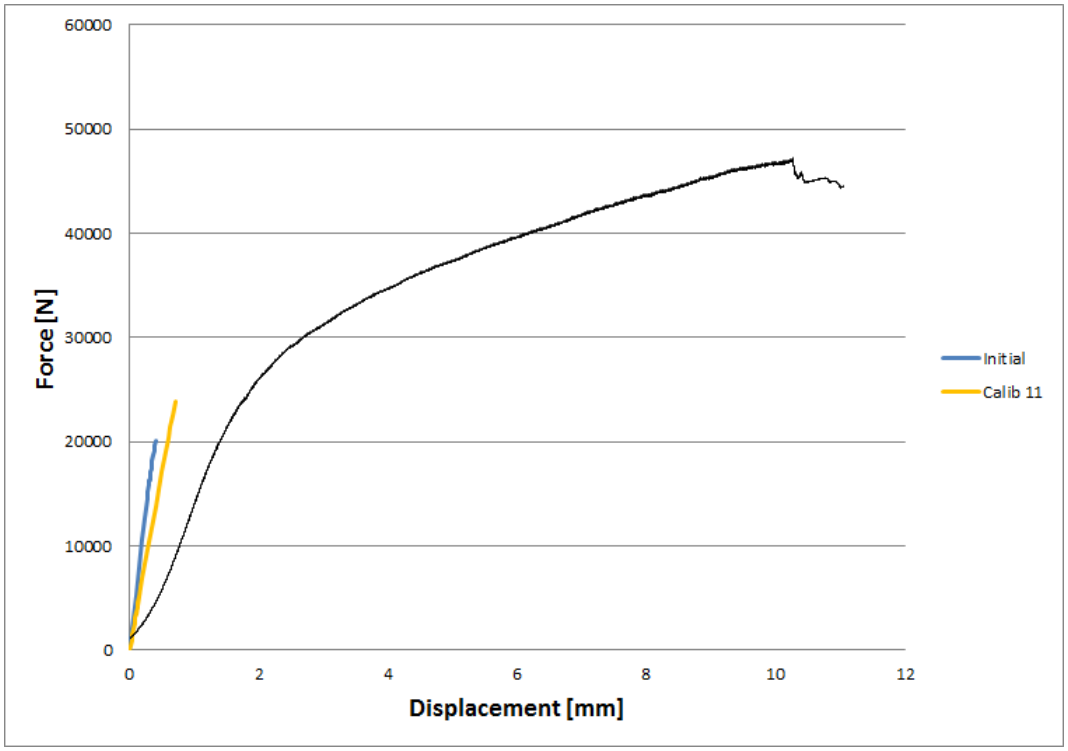

Figure C.7: Load-displacement for case D-Pb-Lc with abaqus model response

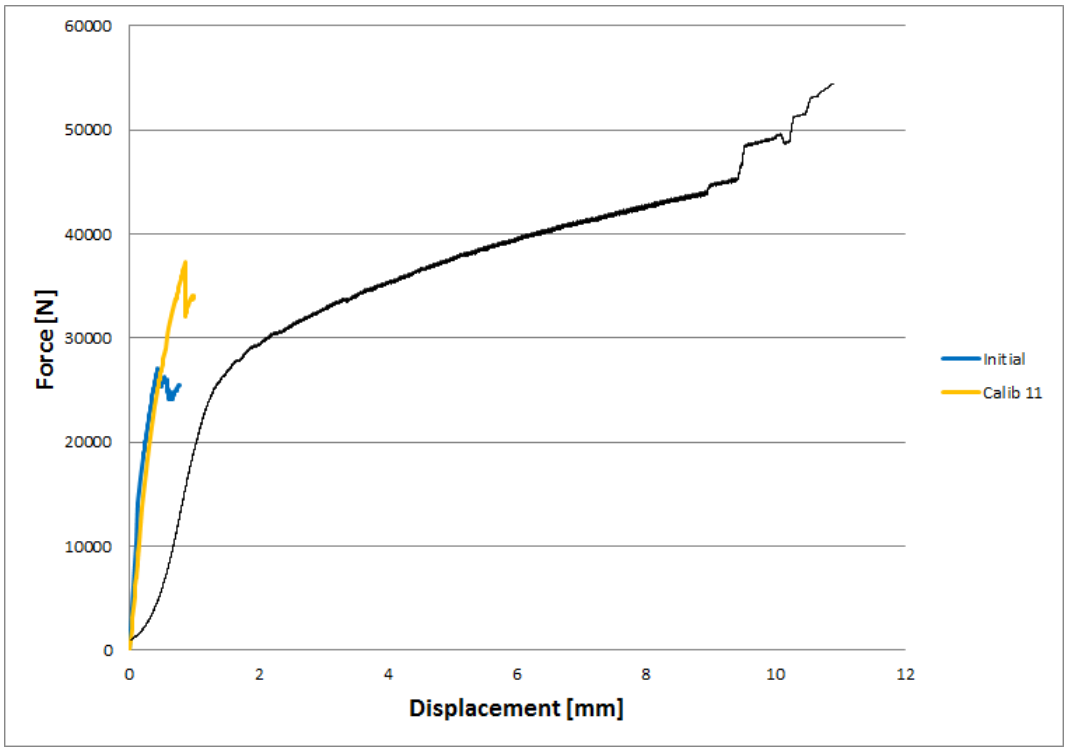

Figure C.8: Load-displacement for case H-Pb-Lc with abaqus model response

Appendix D

Specimen Measurements (Digital)

Appendix E

Test Data (Digital)

Appendix F

Abaqus Input Files (Digital)